Advances in Materials Science and Engineering

Structural Characteristics, Mechanical Properties and Thermal Stability of Bulk Metallic Glasses

Lead Guest Editor: Majid Samavatian
Guest Editors: Amir Mosavi and Shahin Khademinia

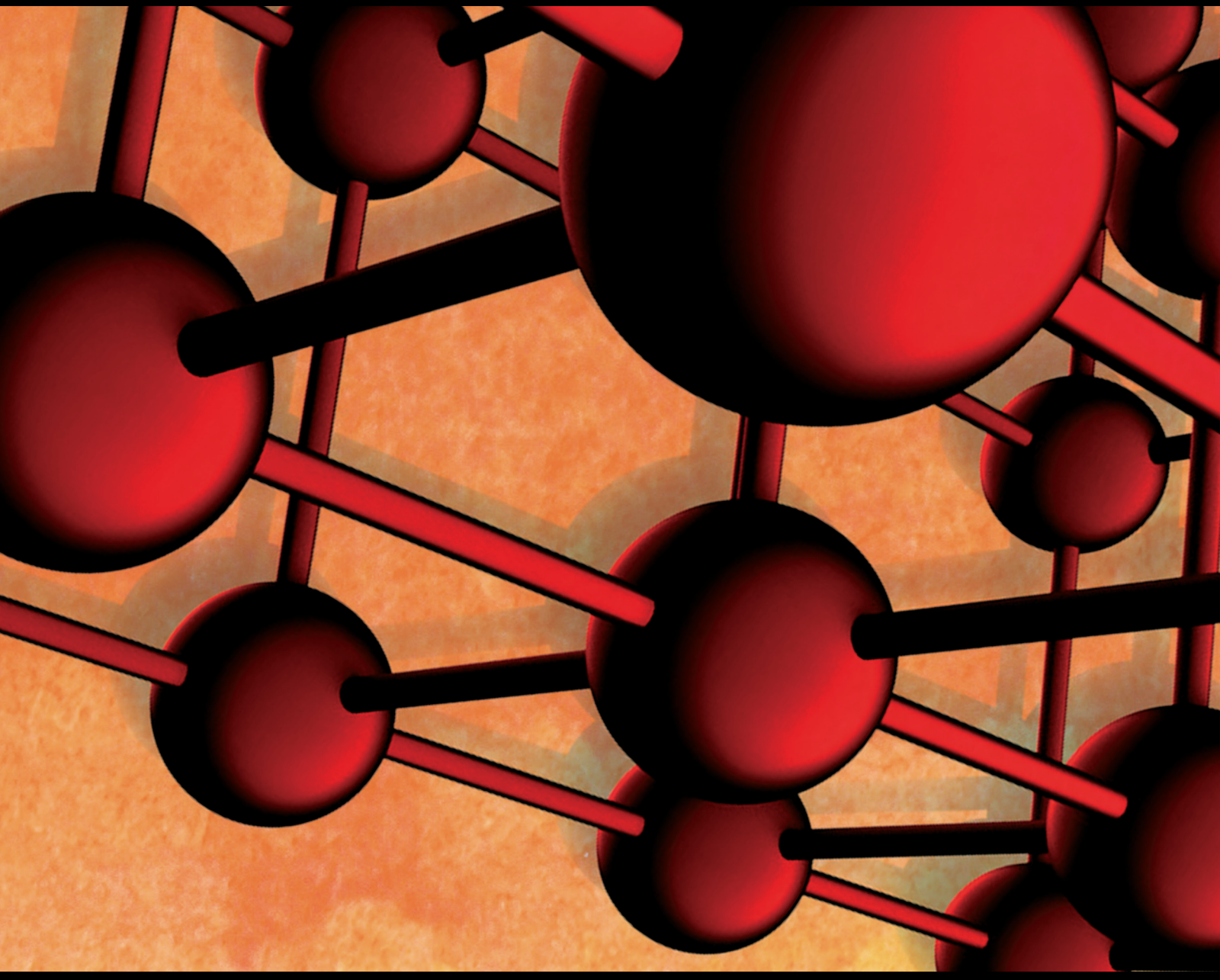

Structural Characteristics, Mechanical Properties and Thermal Stability of Bulk Metallic Glasses

Advances in Materials Science and Engineering

Structural Characteristics, Mechanical Properties and Thermal Stability of Bulk Metallic Glasses

Lead Guest Editor: Majid Samavatian
Guest Editors: Amir Mosavi and Shahin Khademinia

Copyright © 2023 Hindawi Limited. All rights reserved.

This is a special issue published in "Advances in Materials Science and Engineering." All articles are open access articles distributed under the Creative Commons Attribution License, which permits unrestricted use, distribution, and reproduction in any medium, provided the original work is properly cited.

Chief Editor

Amit Bandyopadhyay, USA

Associate Editors

Vamsi Balla, India
Mitun Das, USA
Sandip Harimkar, USA
Ravi Kumar, India
Peter Majewski, Australia
Enzo Martinelli, Italy
Luigi Nicolais, Italy
Carlos R. Rambo, Brazil
Michael J. Schütze, Germany
Kohji Tashiro, Japan
Zhonghua Yao, China
Dongdong Yuan, China
Wei Zhou, China

Academic Editors

Antonio Abate, Germany
Hany Abdo, Saudi Arabia
H.P.S. Abdul Khalil, Malaysia
Ismael alejandro Aguayo villarreal, Mexico
Sheraz Ahmad, Pakistan
Michael Aizenshtein, Israel
Jarir Aktaa, Germany
Bandar AlMangour, Saudi Arabia
Huaming An, China
Alicia Esther Ares, Argentina
Siva Avudaiappan, Chile
Habib Awais, Pakistan
NEERAJ KUMAR BHOI, India
Enrico Babilio, Italy
Renal Backov, France
M Bahubalendruni, India
Sudharsan Balasubramanian, India
Markus Bambach, Germany
Irene Bavasso, Italy
Stefano Bellucci, Italy
Brahim Benmokrane, Canada
Jean-Michel Bergheau, France
Guillaume Bernard-Granger, France
Giovanni Berselli, Italy
Patrice Berthod, France
Michele Bianchi, Italy
Hugo C. Biscaia, Portugal
Antonio Boccaccio, Italy
Mohamed Bououdina, Saudi Arabia
Gianlorenzo Bussetti, Italy
Antonio Caggiano, Germany
Marco Cannas, Italy
Qi Cao, China
Gianfranco Carotenuto, Italy
Paolo Andrea Carraro, Italy
Jose Cesar de Sa, Portugal
Wen-Shao Chang, United Kingdom
Qian Chen, China
Francisco Chinesta, France
Er-Yuan Chuang, Taiwan
Francesco Colangelo, Italy
María Criado, Spain
Enrique Cuan-Urquizo, Mexico
Lucas Da Silva, Portugal
Angela De Bonis, Italy
Abílio De Jesus, Portugal
José António Fonseca De Oliveira Correia, Portugal
Ismail Demir, Turkey
Luigi Di Benedetto, Italy
Maria Laura Di Lorenzo, Italy
Marisa Di Sabatino, Norway
Luigi Di Sarno, Italy
Ana María Díez-Pascual, Spain
Guru P. Dinda, USA
Hongbiao Dong, China
Mingdong Dong, Denmark
Frederic Dumur, France
Stanislaw Dymek, Poland
Kaveh Edalati, Japan
Philip Eisenlohr, USA
Luís Evangelista, Norway
Michele Fedel, Italy
Francisco Javier Fernández Fernández, Spain
Isabel J. Ferrer, Spain
Massimo Fresta, Italy
Samia Gad, Egypt
Pasquale Gallo, Finland
Sharanabasava Ganachari, India
Santiago Garcia-Granda, Spain
Carlos Garcia-Mateo, Spain

Achraf Ghorbal, Tunisia
Georgios I. Giannopoulos, Greece
Ivan Giorgio, Italy
Andrea Grilli, Italy
Vincenzo Guarino, Italy
Daniel Guay, Canada
Jenö Gubicza, Hungary
Xuchun Gui, China
Benoit Guiffard, France
Zhixing Guo, China
Ivan Gutierrez-Urrutia, Japan
Weiwei Han, Republic of Korea
Simo-Pekka Hannula, Finland
A. M. Hassan, Egypt
Akbar Heidarzadeh, Iran
Yi Huang, United Kingdom
Joshua Ighalo, Nigeria
Saliha Ilican, Turkey
Md Mainul Islam, Australia
Ilia Ivanov, USA
Jijo James, India
Hafsa Jamshaid, Pakistan
Hom Kandel, USA
Kenji Kaneko, Japan
Rajesh Kannan A, Democratic People's Republic of Korea
Mehran Khan, Hong Kong
Akihiko Kimura, Japan
Ling B. Kong, Singapore
Pramod Koshy, Australia
Hongchao Kou, China
Alexander Kromka, Czech Republic
Abhinay Kumar, India
Avvaru Praveen Kumar, Ethiopia
Sachin Kumar, India
Paweł Kłosowski, Poland
Wing-Fu Lai, Hong Kong
Luciano Lamberti, Italy
Fulvio Lavecchia, Italy
Laurent Lebrun, France
Joon-Hyung Lee, Republic of Korea
Cristina Leonelli, Italy
Chenggao Li, China
Rongrong Li, China
Yuanshi Li, Canada
Guang-xing Liang, China
Barbara Liguori, Italy
Jun Liu, China
Yunqi Liu, China
Rong Lu, China
Zhiping Luo, USA
Fernando Lusquiños, Spain
Himadri Majumder, India
Dimitrios E. Manolakos, Greece
Necmettin Maraşlı, Turkey
Alessandro Martucci, Italy
Roshan Mayadunne, Australia
Mamoun Medraj, Canada
Shazim A. Memon, Kazakhstan
Pratima Meshram, India
Mohsen Mhadhbi, Tunisia
Philippe Miele, France
Andrey E. Miroshnichenko, Australia
Ajay Kumar Mishra, South Africa
Hossein Moayedi, Vietnam
Dhanesh G. Mohan, United Kingdom
Sakar Mohan, India
Namdev More, USA
Tahir Muhmood, China
Faisal Mukhtar, Pakistan
Dr. Tauseef Munawar, Pakistan
Roger Narayan, USA
Saleem Nasir, Pakistan
Elango Natarajan, Malaysia
Rufino M. Navarro, Spain
Miguel Navarro-Cia, United Kingdom
Behzad Nematollahi, Australia
Peter Niemz, Switzerland
Hiroshi Noguchi, Japan
Dariusz Oleszak, Poland
Laurent Orgéas, France
Togay Ozbakkaloglu, United Kingdom
Marián Palcut, Slovakia
Davide Palumbo, Italy
Gianfranco Palumbo, Italy
Murlidhar Patel, India
Zbyšek Pavlík, Czech Republic
Alessandro Pegoretti, Italy
Gianluca Percoco, Italy
Andrea Petrella, Italy

Claudio Pettinari, Italy
Giorgio Pia, Italy
Candido Fabrizio Pirri, Italy
Marinos Pitsikalis, Greece
Alain Portavoce, France
Simon C. Potter, Canada
Ulrich Prahl, Germany
Veena Ragupathi, India
Kawaljit singh Randhawa, India
Baskaran Rangasamy, Zambia
Paulo Reis, Portugal
Hilda E. Reynel-Avila, Mexico
Yuri Ribakov, Israel
Aniello Riccio, Italy
Anna Richelli, Italy
Antonio Riveiro, Spain
Marco Rossi, Italy
Fernando Rubio-Marcos, Spain
Francesco Ruffino, Italy
Giuseppe Ruta, Italy
Sachin Salunkhe, India
P Sangeetha, India
Carlo Santulli, Italy
Fabrizio Sarasini, Italy
Senthil Kumaran Selvaraj, India
Raffaele Sepe, Italy
Aabid H Shalla, India
Poorva Sharma, China
Mercedes Solla, Spain
Tushar Sonar, Russia
Donato Sorgente, Italy
Charles C. Sorrell, Australia
Damien Soulat, France
Adolfo Speghini, Italy
Antonino Squillace, Italy
Koichi Sugimoto, Japan
Jirapornchai Suksaeree, Thailand
Baozhong Sun, China
Sam-Shajing Sun, USA
Xiaolong Sun, China
Yongding Tian, China
Hao Tong, China
Achim Trampert, Germany
Tomasz Trzepieciński, Poland
Kavimani V, India
Matjaz Valant, Slovenia
Mostafa Vamegh, Iran
Lijing Wang, Australia
Jörg M. K. Wiezorek, USA
Guosong Wu, China
Junhui Xiao, China
Guoqiang Xie, China
YASHPAL YASHPAL, India
Anil Singh Yadav, India
Yee-wen Yen, Taiwan
Hao Yi, China
Wenbin Yi, China
Tetsu Yonezawa, Japan
Hiroshi Yoshihara, Japan
Bin Yu, China
Rahadian Zainul, Indonesia
Lenka Zaji#c#kova#, Czech Republic
Zhigang Zang, China
Michele Zappalorto, Italy
Gang Zhang, Singapore
Jinghuai Zhang, China
Zengping Zhang, China
You Zhou, Japan
Robert Černý, Czech Republic

Contents

Hindawi
Advances in Materials Science and Engineering
Volume 2023, Article ID 3938111, 6 pages
https://doi.org/10.1155/2023/3938111

Research Article

Improving the Corrosion Resistance of NiNb-Based Bulk Metallic Glass through the Hot Compression

Abeer Abdullah Al Anazi,[1] Andrés Alexis Ramírez-Coronel,[2,3,4,5] Rasha Fadhel Obaid,[6] Abdullah Albaker,[7] M. Abdulfadhil Gatea,[8] and Seyed Mojtaba Mostafavi[9]

[1]*Department of Mechanical Engineering, Australian University (AU), Kuwait City, Kuwait*
[2]*Azogues Campus Nursing Career, Health and Behavior Research Group (HBR), Psychometry and Ethology Laboratory, Catholic University of Cuenca, Cuenca, Ecuador*
[3]*University of Palermo, Buenos Aires, Argentina*
[4]*ADEPIN Research Group, National University of Education, Azogues, Ecuador*
[5]*Epidemiology and Biostatistics Research Group, CES University, Colombia*
[6]*Department of Biomedical Engineering, Al-Mustaqbal University College, Babylon, Iraq*
[7]*Department of Electrical Engineering, College of Engineering, University of Ha'il, Ha'il 81451, Saudi Arabia*
[8]*Technical Engineering Department, College of Technical Engineering, The Islamic University, Najaf, Iraq*
[9]*Department of Chemistry, Islamic Azad University Tehran Branch, Tehran, Iran*

Correspondence should be addressed to Seyed Mojtaba Mostafavi; mostafavi@rosecal.com.au

Received 20 October 2022; Revised 30 November 2022; Accepted 31 March 2023; Published 14 April 2023

Academic Editor: Majid Samavatian

Copyright © 2023 Abeer Abdullah Al Anazi et al. This is an open access article distributed under the Creative Commons Attribution License, which permits unrestricted use, distribution, and reproduction in any medium, provided the original work is properly cited.

This paper aims to study and evaluate the corrosion resistance of $Ni_{55}Nb_{45}$ and $Ni_{55}Nb_{35}Co_5Zr_5$ bulk metallic glasses (BMGs) in an environment similar to proton exchange membrane fuel cells. Moreover, the hot compression process was carried out to find the effects of a thermomechanical treatment on the corrosion resistance. The X-ray diffraction (XRD) test indicated that the hot compression process led to formation of crystalline species in both samples; however, it was more pronounced in the $Ni_{55}Nb_{35}Co_5Zr_5$ alloy. It is suggested that the minor addition of Zr and Co facilitated the crystallization in the material. The polarization test unveiled that the hot compression deteriorated the corrosion resistance of the $Ni_{55}Nb_{45}$ alloy through the introduction of anomalous chemical interfaces. On the other hand, the hot deformation affected the $Ni_{55}Nb_{35}Co_5Zr_5$ alloy in a positive way, so that the corrosion behavior improved compared with its fully glassy state. It is suggested that the hot deformation induces some NiNb crystalline constituencies in the microstructure of $Ni_{55}Nb_{35}Co_5Zr_5$ BMG, leading to the enrichment of glassy matrix from Zr/Co constituencies and the enhancement of corrosion resistance.

1. Introduction

In recent years, a growing interest has been attracted to apply bulk metallic glasses (BMGs) as the bipolar plates in the proton exchange membrane fuel cells [1–3]. A wide range of properties from corrosion resistance to flexural strength is needed for considering a material as a bipolar plate [4–6]. Among a broad spectrum of alloy compositions in the glassy systems, Ni-based BMGs are promising alloys with excellent corrosion resistance, which can be employed as bipolar plates in the proton exchange membrane fuel cells [7, 8]. Several processes such as annealing, microalloying, and thermomechanical treatments have been carried out to improve the corrosion resistance of Ni-based BMGs as much as possible. For instance, Espinoza Vazquez et al. [9] reported that NiNb amorphous alloy exhibited a superior corrosion resistance under the presence of chloride ions when the pH value was in the range of 0–7. On the other hand, the passive film got inhomogeneous, and the corrosion rate increased at pH = 14. Zhao et al. [10] applied cryogenic

cycling and annealing treatments to improve the corrosion behavior of $Ni_{62}Nb_{33}Zr_5$ BMG in a 3.5 wt.% NaCl solution. Their results indicated that both treatments with optimized parameters enhanced the corrosion resistance and thermal stability. After cryogenic cycling, the sample exhibited an excellent corrosion resistance, which was related to the high degree of amorphization. In the annealed samples, the fully crystallized state showed a superior anticorrosion performance, which was due to the formation of Nb-rich and Zr-rich oxides. Poddar et al. [11] demonstrated that the oxidation kinetics of $Ni_{60}Nb_{30}Ta_{10}$ BMG included a two-stage parabolic-rate trend under the glass transition temperature. Moreover, the constant of the parabolic rate enhanced with the rise of oxidation temperature. Poddar et al. [12] also characterized the corrosion resistance of thermally oxidized $Ni_{60}Nb_{30}Ta_{10}$ in the nitric acid medium and found that the electrochemical corrosion behavior was consistent with the type of semiconducting nature of the oxide film. Reported in another study [13], it was unveiled that the amorphous $Ni_{60}Nb_{30}Ta_{10}$ exhibited a higher corrosion resistance in comparison with partially crystallized state. This was due to the depletion of the nano α-Ni phase in the system. Jiang et al. [14] applied NiNb amorphous coatings on the stainless steel for improving the corrosion resistance. It was unveiled that the $Ni_{50}Nb_{50}$ resisted corrosion owing to the creation of the passive film with a considerable amount of Nb_2O_5 species. On the other hand, the $Ni_{60}Nb_{40}$ amorphous coating with a high Ni content exhibited weak corrosion resistance owing to the devastation of the coating structure caused by the dissolution of Ni cations. Another investigation showed that the oxidation of $Ni_{50}Zr_{25}Nb_{25}$ BMG at 400°C led to the formation of an amorphous oxide film with species of ZrO_2 and Nb_2O_5, improving the corrosion resistance in the concentrated nitric acid [15].

In general, the previous works indicated that the NiNb-based BMGs are promising alloys for application in corrosive environments [16–18]. However, it is possible to improve the corrosion resistance of this type of alloy through manipulating the chemical composition and applying mechanical or thermal treatments. For example, Wang et al. [19] unveiled that the heat treatment above the glass transition temperature significantly changed the corrosion resistance of the $Zr_{56}Al_{16}Co_{28}$ alloy. Zhao et al. [20] also reported that the corrosion behavior of the deformed ZrCuNiAl MG after heat treatment is much better than that of the deformed MG prior to the heat treatment. Figueira et al. [8] demonstrated that the thermomechanical post-treatment was an efficient method for improving the corrosion resistance of NiNb-based BMGs. It was also found that the severe surface deformation led to an alteration of free volume and enhancement of bio-corrosion resistance in the BMGs [21]. Xing et al. [22] indicated that the pre-compression treatment at room temperature induced the partial crystallization in the MGs and increased the corrosion resistance in the seawater solution. In this study, we added Zr and Co constitutes to the NiNb BMG and also conducted a thermomechanical process to enhance the corrosion resistance of NiNb BMGs in an environment similar to that of proton exchange membrane fuel cells (PEMFC). In this type of cells, electricity is generated through a reaction between hydrogen and oxygen, so that the only by-products are water and heat [23, 24].

2. Experimental Procedure

The $Ni_{55}Nb_{45}$ and $Ni_{55}Nb_{35}Co_5Zr_5$ alloying compositions (at. %) were prepared through the arc-remelting process. To fabricate ingots with a homogeneous composition, high-purity elemental constitutes (>99.7%) were mixed and melted for four times. The alloys were then cast using the water-cooled copper mold. The prepared samples were in the form of plates with dimensions of $40 \times 30 \times 2\,mm^3$. The temperature features of samples were characterized by a Perkin Elmer 6000 differential scanning calorimeter (DSC) with heating and cooling rates of 20 K/min under a protective environment. It should be noted that the DSC instrument was calibrated through the thermographs of high-purity Al and Zr elements. To apply thermomechanical treatment, the hot deformation was carried out at a 0.75 mm/min compression rate at $0.98T_g$. The final thickness of samples decreased about 2% after the hot deformation. The X-ray diffraction (XRD-EQUINOX 100) test with Cu-Kα radiation was also carried out to reveal the amorphous structure or possible crystalline species in the samples.

To measure the electrochemical parameters, an Origa-Stat200 potentiostat was used along with a saturated Ag/AgCl electrode as reference and a platinum mesh as a counter-electrode. To simulate the environment of proton exchange membrane fuel cells, 2 ppm F + 1 M H_2SO_4 at 70°C were prepared [8, 25]. Prior to any measurement, the working electrode was left at open circuit potential for 2 hours. Electrochemical impedance microscopy was done with a signal amplitude around the open circuit potential and the recording rate of 15 points/decade. The curves of potentiodynamic polarization were obtained with the scan rate of 1 mV/s. It should be noted that the stainless steel 316L was considered as a reference material for comparative study.

3. Results and Discussion

At the first step, it is required to identify the possible formation of crystalline phases in the samples. Figure 1 illustrates the XRD patterns of $Ni_{55}Nb_{45}$ and $Ni_{55}Nb_{35}Co_5Zr_5$ at the initial and treated states. Considering the broad peak in the patterns, it is found that the samples at their initial state exhibit a dominant amorphous structure, implying that the copper mold casting successfully produced the BMGs. On the other hand, the thermomechanical process led to the formation of crystalline species in the samples. Although the types of crystals are similar for both alloy compositions, i.e., Ni_3Nb and Nb_7Ni_6, the peak intensities in the XRD pattern of $Ni_{55}Nb_{35}Co_5Zr_5$ are obviously sharper. This result indicates that the minor addition of Zr and Co facilitates the formation of NiNb crystalline phases under hot compression. To ascertain the reasons for this event, it is necessary to evaluate the thermographs of samples. Figure 2(a) represents the DSC curves prior to the glass transition temperature (T_g)

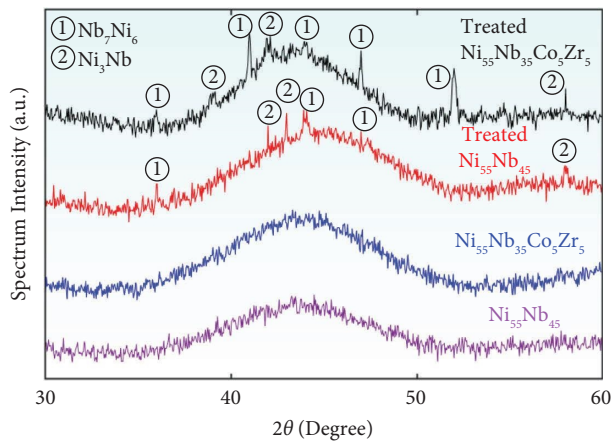

Figure 1: X-Ray diffraction patterns for raw and treated samples.

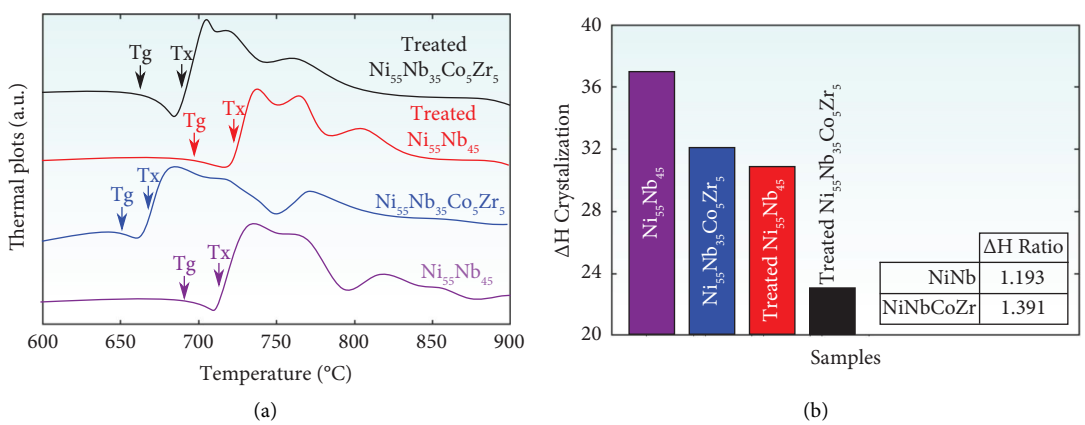

Figure 2: (a) thermographs of samples in the crystallization region for raw and treated samples, (b) enthalpy of crystallization for the samples.

up to the end of full crystallization. First of all, it is detected that the minor addition decreased the T_g value and thermal stability (ΔT_x) in the $Ni_{55}Nb_{35}Co_5Zr_5$ alloy (See Table 1). Moreover, compared to the BMG state, the thermomechanical process leads to a shift of crystallization peaks to the higher temperatures. The exothermic peaks of crystallization are also weakened, which is a sign of a decrease in the enthalpy of crystallization for the treated samples (See Figure 2(b)). This result is consistent with the formation of crystalline phases under thermomechanical processes, as also concluded from the XRD patterns. Considering the inset of Figure 2(b), the enthalpy ratio ($\Delta H_{crys\text{-}untreated}/\Delta H_{crys\text{-}treated}$) of $Ni_{55}Nb_{45}$ is lower than the $Ni_{55}Nb_{35}Co_5Zr_5$ system, approving that that of the crystallization under thermomechanical process is less pronounced in the $Ni_{55}Nb_{45}$ alloy.

Figure 3 demonstrates the polarization curves for all the samples. Based on the results, the i_{corr} for the amorphous $Ni_{55}Nb_{45}$ and $Ni_{55}Nb_{35}Co_5Zr_5$ are 0.07 and 0.11 $\mu A{\cdot}cm^{-2}$, while their E_{corr} values are measured at 0.105 and 0.091 V_{SCE}, respectively. This result indicates that the corrosion resistance of amorphous $Ni_{55}Nb_{45}$ is slightly better than that of $Ni_{55}Nb_{35}Co_5Zr_5$ BMG. However, both amorphous samples

Table 1: thermal parameters of samples.

Sample	T_g (°C)	T_x (°C)	ΔT_x (°C)
Treated $Ni_{55}Nb_{45}$	697	726	29
Untreated $Ni_{55}Nb_{45}$	691	719	28
Treated $Ni_{55}Nb_{35}Co_5Zr_5$	668	693	25
Untreated $Ni_{55}Nb_{35}Co_5Zr_5$	654	672	18

exhibit superior corrosion resistance compared to the stainless steel 316L with the i_{corr} and E_{corr} values of 10.7 $\mu A{\cdot}cm^{-2}$ and −0.25 V_{SCE}. The polarization curves also reveal that the thermomechanical process leads to the conflicting effects on the corrosion behavior of amorphous alloys. For treated $Ni_{55}Nb_{45}$, the i_{corr} and E_{corr} values are 0.58 $\mu A{\cdot}cm^{-2}$ and −01 V_{SCE}, respectively. This outcome implies that the crystallization induces the elemental partitioning and increases the anomalous chemical interfaces, leading to deterioration of corrosion resistance in the alloy [8]. On the other hand, the treated $Ni_{55}Nb_{35}Co_5Zr_5$ alloy shows excellent corrosion behavior with the i_{corr} and E_{corr} values of 0.05 $\mu A{\cdot}cm^{-2}$ and 0.143 V_{SCE}; however, this sample also includes the crystalline phases in its microstructure, as seen in Figure 1. The improvement of corrosion resistance in

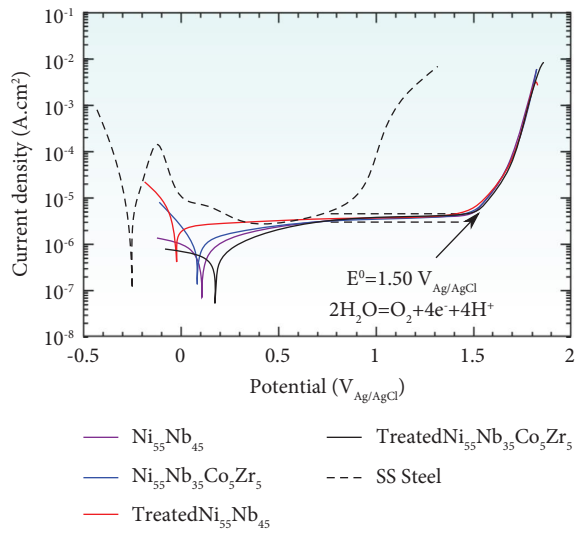

Figure 3: Potentiodynamic polarization curves of raw and treated samples in the condition simulated for proton exchange membrane fuel cell.

the treated $Ni_{55}Nb_{35}Co_5Zr_5$ can be associated to the minor addition of Co and Zr into the alloying composition, which will be discussed later. Another point in the polarization curves is the existence of a passivation plateau for all the samples with a current density in the range of 3.8-4.1 μA·cm^{-2}. It is seen that the passive films exhibit a stable condition, while the water oxidation occurs near +1.5 $V_{Ag/AgCl}$ [8], leading to rise of current density under the polarization. It is worth noting that the criterion for selecting an alloy as bipolar plates is to have i_{corr} less than 16 μA·cm^{-2} [26]. Hence, all of the samples, including the BMGs and their partially-crystalline states, meet the requirements for application in proton exchange membrane fuel cells.

Figure 4(a) illustrates the electrochemical impedance spectroscopy for the BMGs and their treated states. In general, the truncated feature of curves indicates high corrosion resistance, while the weak corrosion behavior of material can be defined by greater Z'/Z'' ratios. One can see that the results are consistent with that detected from the polarization curves. The treated $Ni_{55}Nb_{35}Co_5Zr_5$ exhibited the highest Z''/Z' ratio, meaning the best corrosion behavior among the samples. In the following, the $Ni_{55}Nb_{45}$ and $Ni_{55}Nb_{35}Co_5Zr_5$ BMGs showed the good corrosion resistance and finally the treated $Ni_{55}Nb_{45}$ with partially-crystalline state stands at the end of list. The spectroscopy result of stainless steel 316L is given in the inset of figure. To give a quantitative example, it can be estimated that the Z''/Z' ratio for the treated $Ni_{55}Nb_{35}Co_5Zr_5$ at Z' value of 0.05×10^5 Ω·cm^2 is 12 times higher than the stainless steel, showing the superior corrosion resistance in the glassy systems. The graphs of the frequency response (Bode plot) for the samples are given in Figure 4(b). It is unveiled that the hot compression leads to increase of $|Z|$ value at the minimum of applied frequency for $Ni_{55}Nb_{35}Co_5Zr_5$, which is 9 times higher than its glassy state. On the other hand, the treated $Ni_{55}Nb_{45}$ exhibited a low $|Z|$ value (11 times smaller than its glassy state), showing that the thermomechanical process does not affect the corrosion behavior of amorphous alloys in the same way.

As described above, the response of BMGs to the hot compression strongly depends on the chemical compositions. In the $Ni_{55}Nb_{45}$ alloy, the treatment is accompanied with partial crystallization in the microstructure and the deterioration of corrosion resistance through the introduction of anomalous chemical interfaces. On the other hand, the hot deformation affects the $Ni_{55}Nb_{35}Co_5Zr_5$ BMG in a positive way so that the corrosion behavior improves compared with the glassy states. It is suggested that the presence of Zr and Co into the BMG is the main reason for this event. Zhang et al. [27] unveiled that the creation of a stable passivation layer can be expedited with the addition of cobalt to a Zr-based glassy alloy. Using the Co microalloying process on the high-entropy BMGs, it is found that the anticorrosion property significantly increases under the harsh marine environment [28]. Considering the ZrCuAl BMG, the Co minor addition depletes the copper in the surface film and decreases the corrosion current density [29]. Inoue et al. [7] also reported that the Zr addition into the NiNb glassy system declines the corrosion rate. Another investigation showed that the Zr addition to the NiNb BMG effectively decreases the metallic state Ni content in the surface films, leading to a reduction in passive current density in the corrosion test [30]. In our work, the hot deformation induces some NiNb crystalline constitutents in the microstructure of $Ni_{55}Nb_{35}Co_5Zr_5$ BMG, leading to the enrichment of the glassy matrix from the Zr and Co, compared to the full glassy state. As a result, the effects of the minor addition were intensified, and the anticorrosion property was markedly improved in the $Ni_{55}Nb_{35}Co_5Zr_5$ alloy.

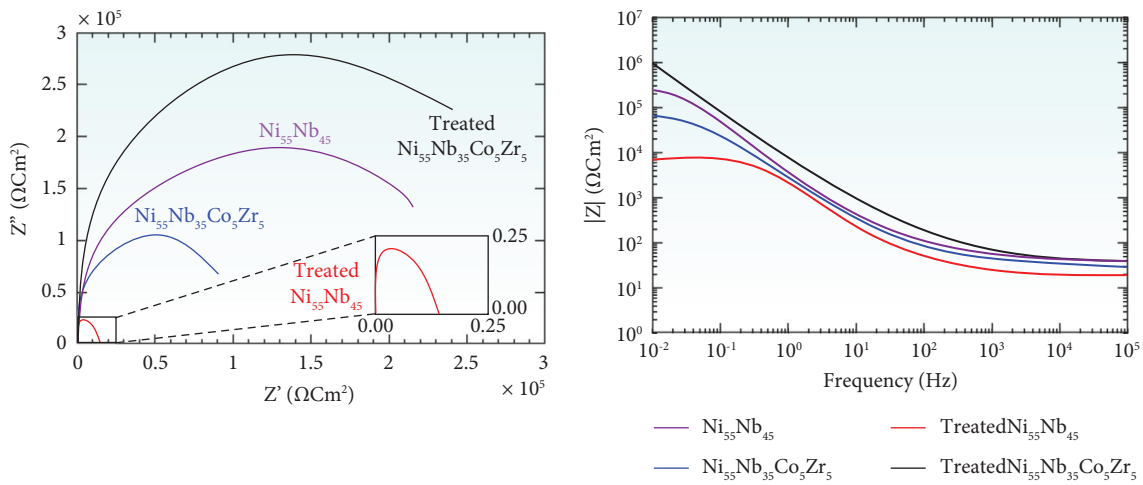

(a) (b)

Figure 4: (a) EIS results of raw and treated samples, (b) the curves of $|Z|$ value as a function of Frequency.

4. Conclusion

The corrosion resistance of $Ni_{55}Nb_{45}$ and $Ni_{55}Nb_{35}Co_5Zr_5$ BMGs and their hot-compressed states was characterized in an environment similar to proton exchange membrane fuel cells. The main outcomes are as follows:

(i) The XRD results demonstrated that the hot compression process led to formation of crystalline species, i.e., Ni_3Nb and Nb_7Ni_6, in both of $Ni_{55}Nb_{45}$ and $Ni_{55}Nb_{35}Co_5Zr_5$ alloys; however, it was more pronounced in the $Ni_{55}Nb_{35}Co_5Zr_5$ sample.

(ii) The DSC curves indicated that the Co and Zr minor additions decreased the T_g value and thermal stability (ΔT_x) of the NiNb-based alloy from 691°C and 28°C to 654°C and 18°C, respectively. Moreover, the thermomechanical process leads to the shift of crystallization peaks to the higher temperatures.

(iii) The polarization test exhibited that the hot compression deteriorated the corrosion resistance of the $Ni_{55}Nb_{45}$ alloy through the introduction of anomalous chemical interfaces. On the other hand, the hot deformation affected the $Ni_{55}Nb_{35}Co_5Zr_5$ alloy in a positive way, so that the corrosion behavior improved compared with its fully glassy state. The quantitative analysis showed that the Z''/Z' ratio for the treated $Ni_{55}Nb_{35}Co_5Zr_5$ at Z' value of $0.05 \times 10^5\ \Omega{\cdot}cm^2$ is 12 times higher than the stainless steel, showing the superior corrosion resistance in the glassy systems.

Data Availability

Data are available upon reasonable request to the corresponding author.

Conflicts of Interest

The authors declare that they have no conflicts of interest.

References

[1] X. Han, S. Feng, S. Chen, Q. Cao, C. Zhang, and Q. Chen, "An investigation of Zr-based bulk metallic glasses as bipolar plates for proton exchange membrane fuel cells," *International Journal of Hydrogen Energy*, vol. 45, no. 4, pp. 3132–3144, 2020.

[2] H. W. Yoon, J. Y. Choi, H. J. Park, J. H. Sun, S. Y. Shin, and K. I. Moon, "Zr-based thin-film metallic glass for bipolar plate in proton exchange membrane fuel cells," *Advanced Engineering Materials*, vol. 22, no. 10, Article ID 2000369, 2020.

[3] N. Li, J. Pan, Z. Liu, and L. Liu, "Metallic glass nanostructures: forming strategies and functional applications," *Materials Today Advances*, vol. 15, Article ID 100253, 2022.

[4] F. Bahrami, R. Amini, and A. H. Taghvaei, "Microstructure and corrosion behavior of electrodeposited Ni-based nanocomposite coatings reinforced with Ni60Cr10Ta10P16B4 metallic glass particles," *Journal of Alloys and Compounds*, vol. 714, pp. 530–536, 2017.

[5] Q. Li, S. S. Liu, X. H. Wang et al., "Mechanical and corrosion properties of Ti-Ni-Cu-Zr metallic glass matrix composites," *Journal of Alloys and Compounds*, vol. 727, pp. 1344–1350, 2017.

[6] H. Joress, B. L. DeCost, S. Sarker et al., "A high-throughput structural and electrochemical study of metallic glass formation in Ni–Ti–Al," *ACS Combinatorial Science*, vol. 22, no. 7, pp. 330–338, 2020.

[7] A. Inoue, T. Shimizu, S. Yamaura, Y. Fujita, S. Takagi, and H. Kimura, "Development of glassy alloy separators for a proton exchange membrane fuel cell (PEMFC)," *Materials Transactions*, vol. 46, no. 7, pp. 1706–1710, 2005.

[8] G. Figueira, S. Dulnee, G. Y. Koga et al., "Influence of thermomechanical post-treatment on the corrosion behavior of Ni57Nb33Zr5Co5 bulk metallic glass," *Materials Letters*, vol. 288, Article ID 129350, 2021.

[9] A. Espinoza Vazquez, A. Soriano Carranza, I. A. Figueroa Vargas, and F. Rodriguez, "Effect of the pH on the corrosion behaviour for a $Ni_{59.5}$ $Nb_{40.5}$ binary metallic glass," *ECS Transactions*, vol. 106, no. 1, pp. 63–70, 2022.

[10] K. Zhao, N. Wang, S. Li et al., "Corrosion behavior of Ni62Nb33Zr5 bulk metallic glasses after annealing and cryogenic treatments," *ChemPhysMater*, 2022.

[11] C. Poddar, J. Jayaraj, C. Mallika, and U. Kamachi Mudali, "Oxidation behaviour of Ni60Nb30Ta10 metallic glass below its glass transition temperature," *Journal of Alloys and Compounds*, vol. 728, pp. 1146–1152, 2017.

[12] C. Poddar, J. Jayaraj, and S. Ningshen, "Passive film characteristics and corrosion behavior of thermally oxidized Ni60Nb30Ta10 metallic glass in nitric acid medium," *Journal of Alloys and Compounds*, vol. 783, pp. 680–686, 2019.

[13] C. Poddar, S. Ningshen, and J. Jayaraj, "Corrosion assessment of Ni60 Nb30Ta10 metallic glass and its partially crystallized alloy in concentrated nitric acid environment," *Journal of Alloys and Compounds*, vol. 813, Article ID 152172, 2020.

[14] L. Jiang, Z. Q. Chen, H. B. Lu et al., "Corrosion protection of NiNb metallic glass coatings for 316SS by magnetron sputtering," *Journal of Materials Science and Technology*, vol. 79, pp. 88–98, 2021.

[15] C. Poddar, J. Jayaraj, S. Amirthapandian, and S. Ningshen, "Effect of thermally grown amorphous oxide film on the corrosion resistance properties of Ni50Zr25Nb25 metallic glass in nitric acid medium," *Intermetallics*, vol. 113, Article ID 106571, 2019.

[16] Z. M. Wang, J. Zhang, X. C. Chang, W. L. Hou, and J. Q. Wang, "Structure inhibited pit initiation in a Ni–Nb metallic glass," *Corrosion Science*, vol. 52, no. 4, pp. 1342–1350, 2010.

[17] Z. F. Wu, Q. P. Cao, Y. Ma et al., "Thickness-dependent pitting corrosion behavior in Ni–Nb thin film metallic glass," *Thin Solid Films*, vol. 564, pp. 294–298, 2014.

[18] K. Zhang, X. Gao, Y. Dong, Q. Xing, and Y. Wang, "Effect of annealing on the microstructure, microhardness, and corrosion resistance of Ni62Nb33Zr5 metallic glass and its composites," *Journal of Non-crystalline Solids*, vol. 425, pp. 46–51, 2015.

[19] R. Wang, Y. Wang, J. Yang, J. Sun, and L. Xiong, "Influence of heat treatment on the mechanical properties, corrosion behavior, and biocompatibility of Zr56Al16Co28 bulk metallic glass," *Journal of Non-crystalline Solids*, vol. 411, pp. 45–52, 2015.

[20] X. Zhao, J. Sun, M. Yu et al., "Effects of heat treatment on the thermal, mechanical and corrosion properties of deformed Zr-based bulk metallic glasses," *Materials Chemistry and Physics*, vol. 256, Article ID 123705, 2020.

[21] G. Perumal, H. S. Grewal, A. Ayyagari, S. Mukherjee, and H. S. Arora, "Enhancement in bio-corrosion resistance of metallic glass by severe surface deformation," *Applied Surface Science*, vol. 487, pp. 1096–1103, 2019.

[22] Q. Xing, K. Zhang, Y. Wang et al., "Effects of pre-compression on the microstructure, mechanical properties and corrosion resistance of RE65Co25Al10 (RE = Ce, La, Pr, Sm and Gd) bulk metallic glasses," *Intermetallics*, vol. 67, pp. 94–101, 2015.

[23] L. Duclos, M. Lupsea, G. Mandil, L. Svecova, P.-X. Thivel, and V. Laforest, "Environmental assessment of proton exchange membrane fuel cell platinum catalyst recycling," *Journal of Cleaner Production*, vol. 142, pp. 2618–2628, 2017.

[24] W. J. Song, H. Chen, H. Guo, F. Ye, and J. R. Li, "Research progress of proton exchange membrane fuel cells utilizing in high altitude environments," *International Journal of Hydrogen Energy*, vol. 47, no. 59, pp. 24945–24962, 2022.

[25] H. Wang, M. A. Sweikart, and J. A. Turner, "Stainless steel as bipolar plate material for polymer electrolyte membrane fuel cells," *Journal of Power Sources*, vol. 115, no. 2, pp. 243–251, 2003.

[26] B. D. Cunningham and D. G. Baird, "Development of bipolar plates for fuel cells from graphite filled wet-lay material and a compatible thermoplastic laminate skin layer," *Journal of Power Sources*, vol. 168, no. 2, pp. 418–425, 2007.

[27] Y. Zhang, L. Yan, X. Zhao, and L. Ma, "Enhanced chloride ion corrosion resistance of Zr-based bulk metallic glasses with cobalt substitution," *Journal of Non-crystalline Solids*, vol. 496, pp. 18–23, 2018.

[28] S. Zhang, Z. Zhang, P. He, Y. Gao, and X. Liang, "Effect of Co addition on the microstructure, thermal stability and anti-corrosion properties of AlNiZrYCo high-entropy metallic glass ribbons," *Journal of Non-crystalline Solids*, vol. 585, Article ID 121555, 2022.

[29] W. Zhou, W. P. Weng, and J. X. Hou, "Glass-forming ability and corrosion resistance of ZrCuAlCo bulk metallic glass," *Journal of Materials Science and Technology*, vol. 32, no. 4, pp. 349–354, 2016.

[30] D. Li, Z. Zhu, H. Zhang, A. Wang, and Z. Hu, "The influence of Zr substitution for Nb on the corrosion behaviors of the Ni-Nb-Zr bulk metallic glasses," *Science China Physics, Mechanics and Astronomy*, vol. 55, no. 12, pp. 2362–2366, 2012.

Hindawi
Advances in Materials Science and Engineering
Volume 2023, Article ID 6232579, 8 pages
https://doi.org/10.1155/2023/6232579

Research Article

Mechanism of Imprinting Process in the Ni-P Metallic Glass Films: A Molecular Dynamics Study

Tri Widodo Besar Riyadi,[1] Ramaswamy Sivaraman,[2] Alaa Mohammed Hussein Wais,[3] Farag M. A. Altalbawy,[4,5] Ulugbek Oybutaevich Khudanov,[6] and Dinesh Kumar Chaudhary[7]

[1]*Faculty of Engineering, Universitas Muhammadiyah Surakarta, Surakarta, Indonesia*
[2]*Department of Mathematics, Dwaraka Doss Goverdhan Doss Vaishnav College, University of Madras, Chennai Arumbakkam, India*
[3]*Biomedical Engineering Department, Al-Mustaqbal University College, Hillah 51001, Babil, Iraq*
[4]*National Institute of Laser Enhanced Sciences (NILES), Cairo University, Giza 12613, Egypt*
[5]*Department of Chemistry, University College of Duba, Tabuk University, Duba 71911, Saudi Arabia*
[6]*Department of Chemistry and Its Teaching Methods, Jizzakh State Pedagogical Institute Named After Abdullah Kadiri, Jizzakh, Uzbekistan*
[7]*Department of Physics, Amrit Campus, Tribhuvan University, Kathmandu, Nepal*

Correspondence should be addressed to Dinesh Kumar Chaudhary; din.2033@gmail.com

Received 28 July 2022; Revised 18 October 2022; Accepted 18 January 2023; Published 31 January 2023

Academic Editor: Shahin Khademinia

Copyright © 2023 Tri Widodo Besar Riyadi et al. This is an open access article distributed under the Creative Commons Attribution License, which permits unrestricted use, distribution, and reproduction in any medium, provided the original work is properly cited.

In this study, the molecular dynamics (MD) simulation was used to evaluate the role of imprinting temperature and the mold-cavity geometry on the imprinted Ni-P metallic glass (MG) films. Considering the outcomes of simulation, it was found that the tip-like and groove patterns showed different filling time for the imprinting process. At room temperature (300 K), the plastic deformation in the tip-like pattern was in a ring shape enclosing the mold, while the plastic deformation in the groove-pattern geometry was mainly localized at the wall of mold. Moreover, it was determined that the imprinting at high temperature (700 K) led to the shortening of pattern filling time and the decrease of loading force in both geometries. The strain concentration and localized plastic deformation were also removed in the high-temperature imprinting process. On the other hand, the unloading process at room temperature (300 K) improved the imprinting quality due to the lower elastic recovery.

1. Introduction

Fabrication of engineering components at micro/nanoscale is one of the huge challenges in the high-tech industries [1–3]. To overcome this issue, nanoimprinting lithography (NIL) has been proposed as a novel technique in which the fabricated patterns and components are the potential candidates for application in optical devices, micro-integration systems, nanomold production, and biological devices [4, 5]. In this method, a mechanical deformation process is conducted to transfer the pattern onto the metallic films by an imprinting-release procedure [6–8].

Due to their disordered atomic structure, metallic glasses (MGs) typically exhibit superior mechanical properties and excellent viscous flow formability [9–13]. Hence, a great interest has been taken by researchers to employ this kind of metallic alloys in the NIL method [14–16]. To provide sample examples, Xiaoyu et al. [17] indicated that the $Fe_{40}Co_{35}P_{10}C_{10}B_5$ amorphous alloy is a favored composition for producing various nano-patterns with adaptable magnetic properties. Li et al. [18] fabricated a nano-patterned template with an amorphous surface through the electrodeposition technique. Their results indicated that the nanoimprint templates exhibited an excellent flexibility and

environmental stability, which was suitable for high-resolution imprint lithography with good industrialization prospects. Using molecular dynamics (MD) simulation, the pattern transfer mechanism of ZrCu MG films under a nanoimprinting process was evaluated, and it was found that the imprinting at large aspect ratio or high temperatures shortened the filling time [19]. Doan et al. [20] indicated that the increase in angle of the punch led to rise of imprinting force and the shear transformation zones (STZs) of the CuZr glassy films. Wu and Hou [21] unveiled that the imprinting process was more efficient at the temperature slightly higher than the glass transition temperature, followed by unloading at room temperature. It was also determined that the tip-like pattern on the mold required a smaller loading force and longer filling time, compared to the groove pattern. Another investigation exhibited that the capillary force and boundary condition played crucial roles in the nanoimprinting process, and the mold filling speed was influenced by the thickness of MG films [22]. Singer et al. [23] applied sacrificial imprint lithography for multiscale patterning of MGs, in which the cost and complexity of generating controlled nanostructures on sophisticated geometries were eliminated. Wang et al. [24] produced large dimensions of nanostructures using an inexpensive thermal imprint method in air with a new composition of Au-based MG exhibiting negative dielectric constants. The $Cu_{50}Zr_{25}Ti_{25}$ MG was also selected for the NIL patterning, and the corresponding microstructural investigations showed that the STZs were generated at the substrate surface underneath the mold during the forming process [25]. Tran et al. [26] investigated the NIL process of CuAgAu films through MD simulation and found that the change in the change in imprinting conditions markedly affected the final mechanical properties and induced the nanocrystallization in the structure. Wang et al. [27] reported that the deformation mechanism of Ni-Zr glassy film can be described through the rearrangement of short-range scale clusters with fractal configuration. It was also demonstrated that the pileup index strongly depended on the temperature and alloying composition in the Ni-Zr amorphous films. Kumar et al. [28] developed a model based on the flow and pressure fields in the NIL process of MGs. They also took into account an additional threshold pressure for breaking the oxide layer on the MG surfaces.

As depicted, the NIL process of MGs plays a crucial role in the production of microcomponents. Hence, it is important to characterize the mechanism of plastic deformation and the mechanics of imprinting for obtaining the optimal parameters. This work aims to analyze the atomic-scale features of imprinted MG films through the MD simulation. Using the atomic-scale modeling, it is possible to accurately study the thermodynamics and mechanical properties by preventing the experimental noises [29–31].

2. Computational Methodology

For MD simulation, the $Ni_{80}P_{20}$ MG was constructed through the embedded-atom method (EAM) potential of the Ni-P system proposed by Sheng et al. [32]. To establish the atomic configuration, the Ni and P atoms with a random distribution were heated to the temperature of 2100 K and kept for 2 ns. Afterwards, the melted alloy was quenched to the room temperature with cooling rate of 10^{11} K/s, followed by a relaxation treatment at 500 K to remove any cooling effect. This simulation was carried out under the isothermal isobaric ensemble (NPT) and time step of 1 fs through the large-scale atomic/molecular massively parallel simulator code. Moreover, the three-dimensional periodic boundary conditions (PBCs) were considered for the simulation and the temperature was controlled by the Nosé–Hoover thermostat [33].

Figure 1 shows that the NIL physical model includes a rigid mold along with the Ni-P MG film, which was cut from the atomic block prepared previously. The NIL process was carried out with two types of patterns, facilitating the evaluation of mold-cavity geometry effects. The MG films included two types of atoms, i.e., Newtonian atoms and fixed atoms, in the simulation. The fixed atoms, located at the top of film, stabilized the whole system during the NIL process. Furthermore, the NVT ensemble and PBCs (at X and Y directions) were applied in the simulation. In the NIL process, the imprinting was conducted through the constant movement of mold (5×10^{-5} nm per time step) followed by a holding time of 60 ps at the maximum displacement and finally the mold was unloaded instantly. The details for the evaluation of atomic interaction in the film and mold/film are given in Ref. [21].

3. Results and Discussion

Figure 2 represents the imprinting process by the tip-like mold at the different displacements (D) and constant temperature of 300 K. When the mold touched the MG film at $D = 0$ nm, some of the MG atoms at the surface were adsorbed onto the mold, which was due to the Van der Waals force at the interface. At the initial stage of NIL process ($D = 1.8$ nm), the shear strain gradually increased underneath the mold and it instantly continued with a rise of D value to 2.4 nm. With the further increment of displacement ($D = 3.1$ nm), the high-strained atoms were nucleated from the sides of mold and generated in a ring-like shape in the microstructure of the MG film. These atoms (red regions) are indicative of shear transformation zones (STZs), which are the sources of plastic deformation in the amorphous structure [34]. Finally, one can see that an apparent ring of strained atoms is formed at the D value of 4.5 nm. Unlike mechanism of dislocations in crystalline alloys, the plastic deformation of MGs is defined by the formation and percolation of nanoscale defects such as STZs [35].

The effects of imprinting temperature on the strain distribution of MG films are illustrated in Figure 3. The strain snapshots give the instant of entire tip-like mold filling in the NIL process. As can be seen, the D value for the entire filling significantly decreases with the rise of temperature, which may be owing to the easier cooperative atomic movement at high temperatures. Moreover, it is observed that the higher temperature facilitates the generation of atomic strain in the bulk of film so that the ring-like shape of

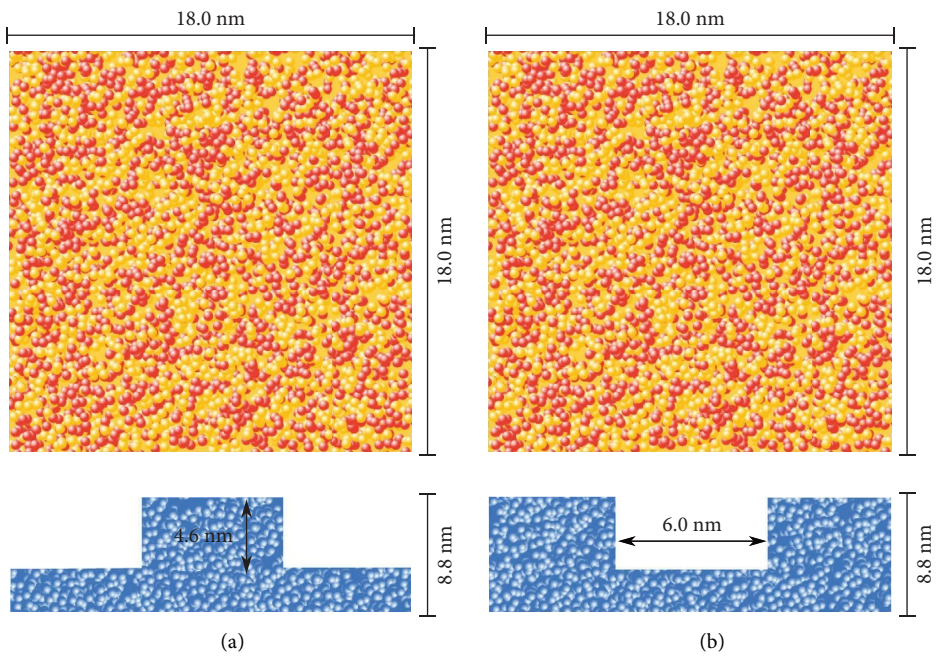

Figure 1: Schematic of (a) tip-like and (b) groove patterns on mold for nanoimprinting process.

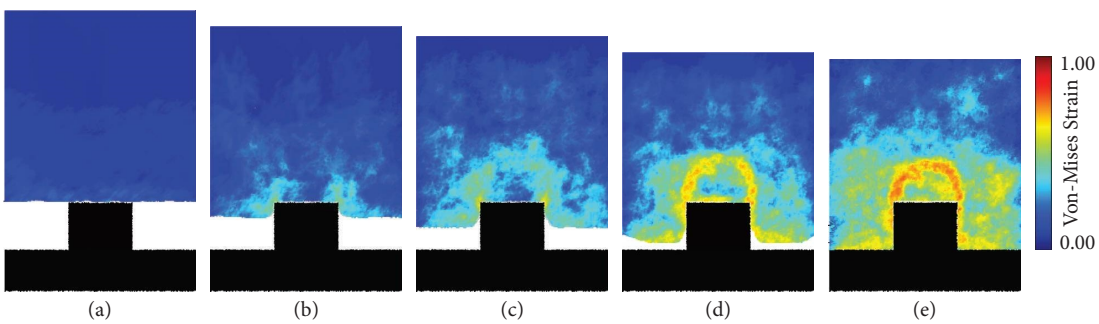

Figure 2: Evolution of imprinting process with tip-like pattern at 300 K for mold displacement of (a) 0 nm, (b) 1.8 nm, (c) 2.4 nm, (d) 3.1 nm, and (e) 4.5 nm.

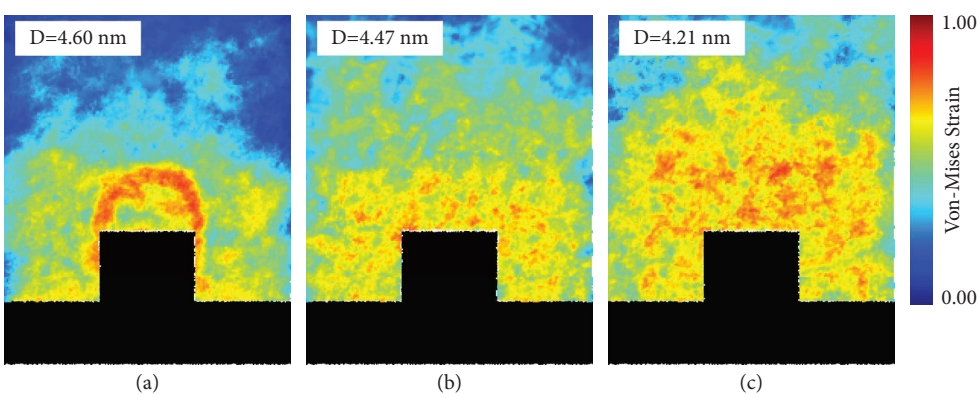

Figure 3: Imprinting process with tip-like pattern in the complete filling stage at (a) 300 K, (b) 500 K, and (c) 700 K.

induced strain at 300 K approximately disappears in the sample imprinted at 700 K (above the glass transition temperature). Figure 4 shows the loading force and filling height as a function of mold displacement for imprinting process at 300 K, 500 K, and 700 K. At the beginning of NIL process, the curves show a negative value which is related to

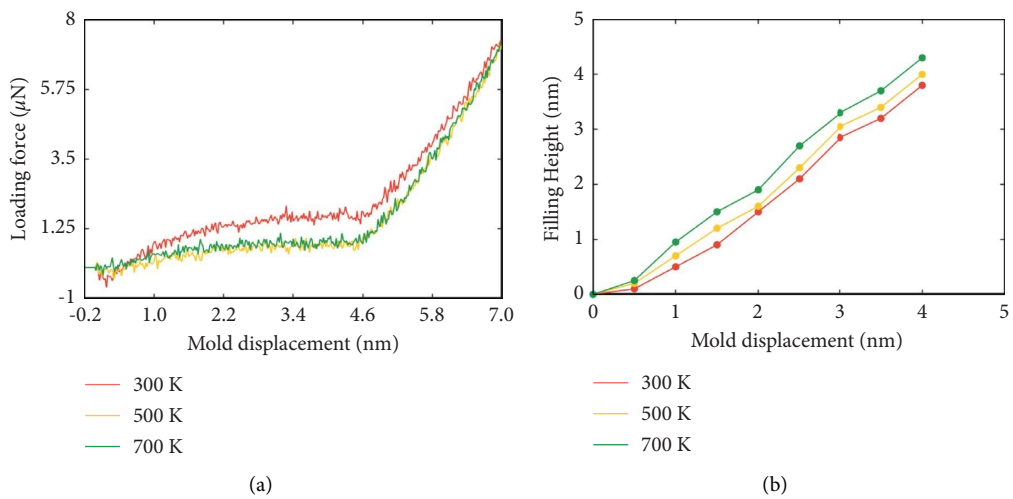

Figure 4: (a) Loading force and (b) filling height as a function of mold displacement for the tip-like pattern imprinting process.

the Van der Waals attractive force between the MG film and the mold (see Figure 4(a)). This negative force is more intensified at lower temperatures. With the increase of mold displacement, the loading force gently rises so that a steady state can be detected in the middle of the imprinting process. Finally, a sharp increment of loading occurs, which is due to the overfilling. In all the imprinting temperatures, the trend of loading force is similar; however, it is clearly found that the lower temperature (300 K) intensifies the force variations. This is due to the fact that the energy barrier for atomic rearrangement and STZ formation is higher at room temperature [21, 22]. Figure 4(b) shows that the high temperature improves the filling efficiency so that the amorphous film readily flows into the cavity and completes the imprinting process at shorter times.

It is feasible to study the recovery of elastic features in the imprinted samples after the unloading. As can be seen in Figure 5(a), there are geometrical parameters defining the elastic recovery in the system. In this criterion, W, H, and h are width of the pattern, height of the whole film, and height of the whole film minus the height of the pattern, respectively. Moreover, W', H', and h' are the indicative of geometrical dimensions after the elastic recovery. Using the mentioned parameters, the elastic recovery can be defined as follows [21]:

$$\eta_x = (|x - x'|/x), \quad (1)$$

in which x and x' are the geometrical parameters before and after the elastic recovery, respectively. Figure 5(b) depicts the change of elastic recovery ratios as a function of imprinting temperature for the tip-like mode. It is found that the mean lowest recovery of elasticity occurs at the room temperature (300 K), meaning that the low-temperature unloading does not significantly affect the final geometry of the imprinted sample. With the rise of temperature, the elastic recovery is intensified, especially at the width direction. According to the results, the mean elastic recovery in the sample imprinted at 700 K is 3-4 times higher than that in the sample proceeded at the room temperature, indicating that the high temperature may lead to the poor pattern transfer with inaccurate final dimensions.

Figure 6 represents the imprinting process at the different displacements (D) and constant temperature of 300 K through the groove pattern on the mold. As can be seen, the typical extrusion process is similar to the backward NIL process with a groove pattern [21]. At the beginning of the imprinting process ($D = 1.1$ nm), some part of MG film is extruded into the groove of mold, leading to the formation of a bow at the arrival. With the increase of D value to 2.9 nm, the extruded atoms into the groove part of the mold markedly rise so that the bow is extended in the groove space. As marked in the figure, the angle between the mold wall and the bow is identified as the dynamic contact angle ($\theta \sim 131^\circ$). The θ value measured in this work is similar to that reported in other investigations focusing on the MGs and polymers [21, 36]. Finally, the groove is completely filled at $D = 4.3$ nm, in which the localized shear strain occurs at the mold walls and the arrival of the groove. It is suggested that the application of the loading force during the NIL process leads to significant stress concentration at the mold walls and subsequent atomic rearrangements in this region. The effects of imprinting temperature on the strain distribution of MG films extruded in the groove mold are illustrated in Figure 7. Similar to the tip-like pattern on mold, the NIL process at higher temperatures declines the time of filling, which is due to the improvement of plastic deformation. Moreover, one can see that the higher temperature leads to the extension of atomic movement from the mold walls and the bow position to the bulk of groove and some regions underneath the mold. It is believed that the higher temperature decreases the energy barrier for the nanoscale atomic rearrangement, and consequently, the atoms in the bulk of samples can locally move and form new structural configurations. In general, the MGs have amorphous structures, in which the loosely packed regions such as free volumes or STZs are embedded in the glassy matrix with densely packed structures [37, 38]. At the higher temperatures, the generation and percolation of loosely packed regions are facilitated, and as a consequence, the plastic deformation is extended in the bulk of material. However,

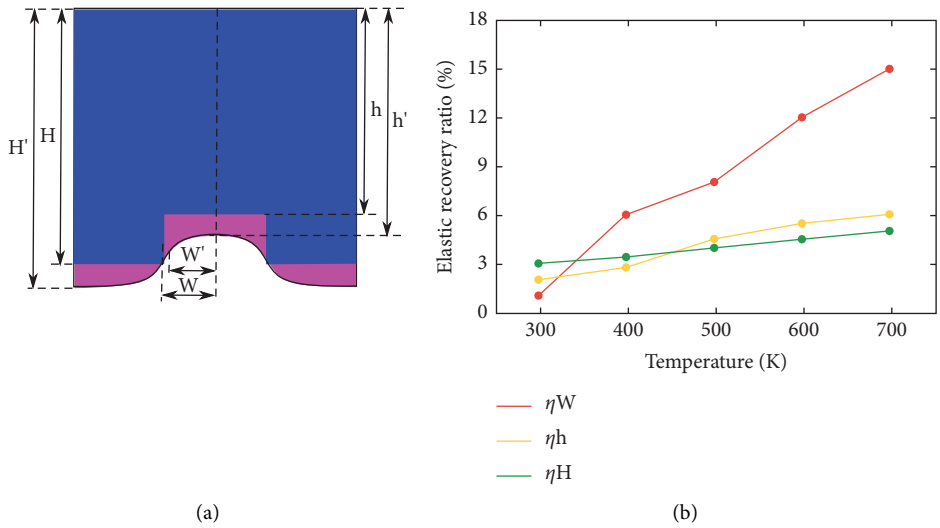

Figure 5: (a) Illustration of parameters defining the elastic recovery and (b) elastic recovery as a function of imprinting temperature for the tip-like pattern.

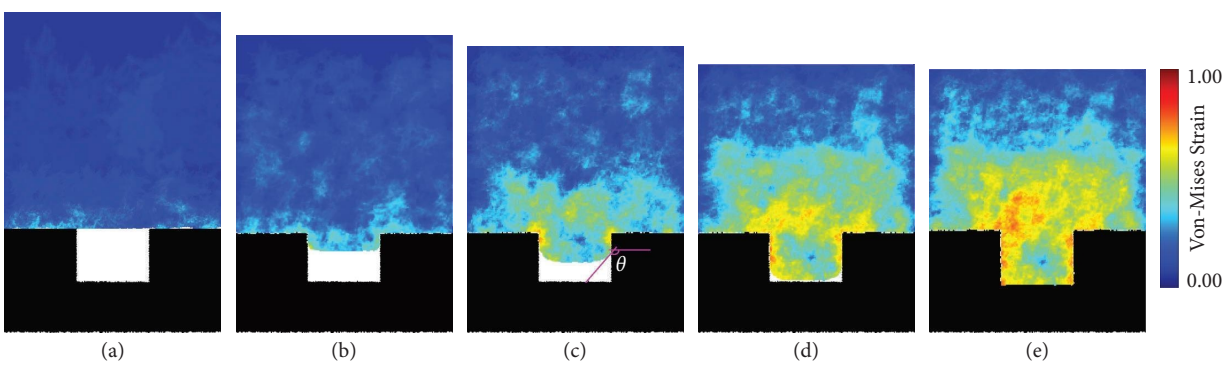

Figure 6: Evolution of imprinting process with groove pattern at 300 K for mold displacement of (a) 0 nm, (b) 1.1 nm, (c) 2.9 nm, (d) 3.5 nm, and (e) 4.38 nm.

one should note that the mentioned event is resulted by the MD simulation, in which the NIL process is conducted in nanoseconds. In the real conditions, the process time is longer which may induce structural relaxation in the MG film so that the imprinting temperature shows a reverse effect. Hence, it is strongly suggested that the high temperature imprinting process for amorphous alloys should be performed in a short time.

Figure 8 indicates the loading force and filling height as a function of mold displacement for the imprinting process with a groove-like mold at 300 K, 500 K, and 700 K. In comparison to the tip-like mode, the Van der Waals force is much higher which may be owing to the larger contact area between the MG film and the mold at the beginning of imprinting process. Furthermore, the fluctuation of loading force, i.e., serrations, is more intensified in this mode, meaning that there is strong interaction between the mold and film. However, Figure 8(b) clearly determines that the groove pattern on the mold improves the performance of filling during the NIL process. This result shows that the mold walls in the groove pattern concentrate the induced stress and enhance the rate of plastic deformation during the process.

As can be observed in Figure 9(a), there also exist geometrical features enabling the evaluation of elastic recovery in the NIL process. In this criterion, W_a' and W_b' are the width of the pattern at the top and the bottom after the recovery, respectively. Moreover, h_1 and h_2 are the height of the whole film and the height of the whole film minus the pattern height, respectively. Using equation (1), it is possible to estimate the elastic recovery based on the mentioned parameters. Figure 9(b) represents the trend of elastic recovery as a function of imprinting temperature for the groove-pattern mold. Similar to the tip-like pattern, the low-temperature process at 300 K leads to the minimum recovery, while the rise of temperature can increase the average elastic variations more than 6-7 times. It is also detected that the increment of pattern width at the top is markedly higher than that at the bottom, implying huge expansion at the width direction. In summary, it was concluded that the high temperature is suitable for the loading stage, while the room temperature should be considered for the unloading stage to minimize the elastic recovery in the imprinted film.

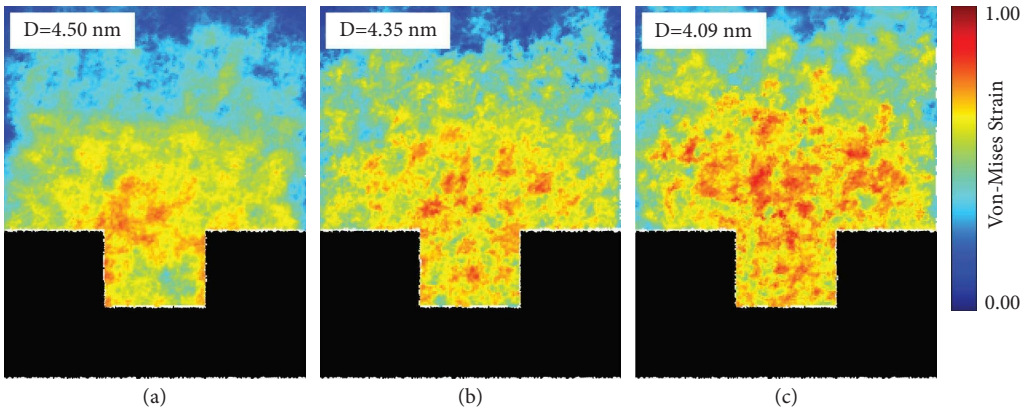

Figure 7: Imprinting process with groove pattern in the complete filling stage at (a) 300 K, (b) 500 K, and (c) 700 K.

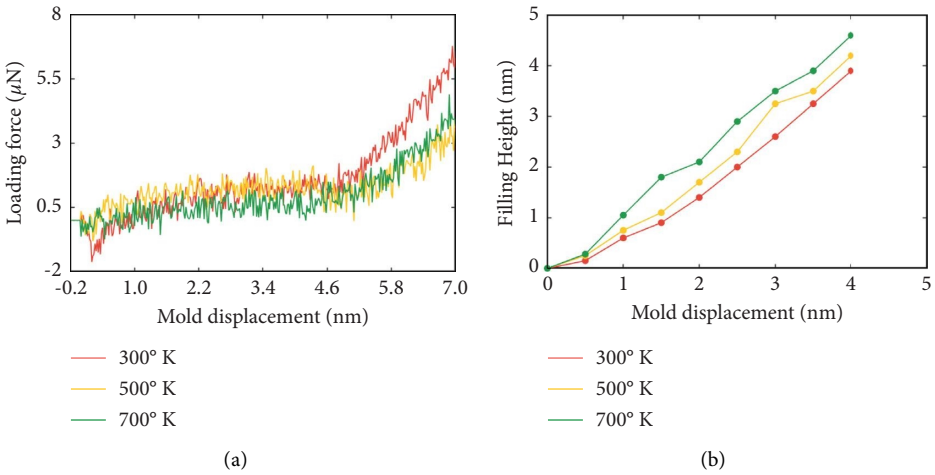

Figure 8: (a) Loading force and (b) filling height as a function of mold displacement for the groove pattern imprinting process.

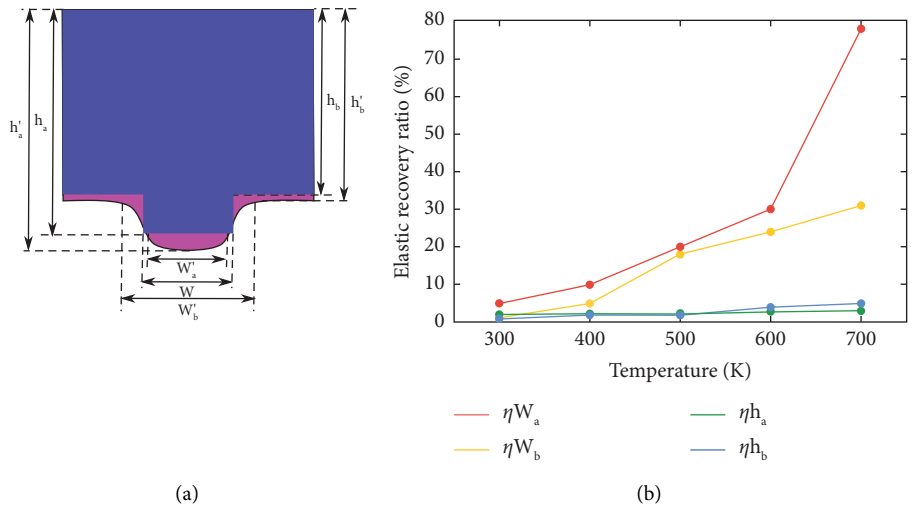

Figure 9: (a) Illustration of parameters defining the elastic recovery and (b) elastic recovery as a function of imprinting temperature for the groove pattern.

4. Conclusion

In this study, the MD simulation was applied to show the influence of imprinting temperature and mold geometry on the quality of imprinted MG films. Based on the MD outcomes, the tip-like geometry of mold cavity led to the formation of plastic regions in a ring-like shape at 300 K, while the increase in the temperature was the main reason for the distribution STZs in the bulk of the MG structure. On the other hand, the groove pattern intensified the plastic deformation at the mold walls and the entrance of the cavity at 300 K. The plastic deformation was also delocalized in this system at high temperatures. It was also demonstrated that the high imprinting temperature was the major factor declining the essential loading force and shortening the filling time in both of imprinting processes. In both of the imprinting systems, the height direction included the lower elastic recovery than that of the width direction. This event was more apparent in the groove pattern.

Data Availability

The data that support the findings of this study are available from the corresponding author upon reasonable demand.

Conflicts of Interest

The authors declare that they have no conflicts of interest.

References

[1] M. Zhang, C. Han, W. Q. Cao, M. S. Cao, H. J. Yang, and J. Yuan, "A nano-micro engineering nanofiber for electromagnetic absorber, green shielding and sensor," *Nano-Micro Letters*, vol. 13, pp. 27–12, 2021.

[2] T. Zhang, Z. Wen, H. Lei et al., "Surface-microengineering for high-performance triboelectric tactile sensor via dynamically assembled ferrofluid template," *Nano Energy*, vol. 87, Article ID 106215, 2021.

[3] A. Khalid, Y. Wei, M. R. Saleem, and W. A. Lughmani, "Meso scale component manufacturing: a comparative analysis of non-lithography and lithography-based processes," *Journal of Micromechanics and Microengineering*, vol. 32, no. 6, Article ID 63002, 2022.

[4] H. C. Jeong, D. H. Kim, D. W. Lee et al., "Solution-driven imprinting lithography of sol–gel ZnO thin films for liquid crystal display," *Langmuir*, vol. 38, no. 8, pp. 2561–2568, 2022.

[5] B. Liu, Y. Yu, Z. Hu et al., "Ag metal interconnect wires formed by pseudoplastic nanoparticles fluid imprinting lithography with microwave assistant sintering," *Nanotechnology*, vol. 33, no. 27, Article ID 275301, 2022.

[6] B. Kumar, P. S. Choubey, and B. N. S. Bhaktha, "High-quality-factor dye-doped polymeric microdiscs fabricated by soft imprint lithography," *The European Physical Journal - Special Topics*, vol. 231, no. 4, pp. 781–789, 2022.

[7] Y. Lee, H. Chae, K. C. Lee et al., "Fabrication of integrated lensless cameras via UV-imprint lithography," *IEEE Photonics J*, vol. 14, no. 2, pp. 1–8, 2022.

[8] J. H. Kang, K. S. Kim, and K. W. Kim, "Molecular dynamics study on the effects of stamp shape, adhesive energy, and temperature on the nanoimprint lithography process," *Applied Surface Science*, vol. 257, no. 5, pp. 1562–1572, 2010.

[9] J. Wegner, M. Frey, M. Piechotta et al., "Influence of powder characteristics on the structural and the mechanical properties of additively manufactured Zr-based bulk metallic glass," *Materials and Design*, vol. 209, Article ID 109976, 2021.

[10] M. Ghidelli, A. Orekhov, A. L. Bassi et al., "Novel class of nanostructured metallic glass films with superior and tunable mechanical properties," *Acta Materialia*, vol. 213, Article ID 116955, 2021.

[11] M. Li, H. Guan, S. Yang, X. Ma, and Q. Li, "Minor Cr alloyed Fe–Co–Ni–P–B high entropy bulk metallic glass with excellent mechanical properties," *Materials Science and Engineering*, vol. 805, Article ID 140542, 2021.

[12] R. Sivaraman, I. Patra, Z. M. Najm, N. M. Hameed, T. Alawsi, and S. Hashemi, "The effects of minor element addition on the structural heterogeneity and mechanical properties of ZrCuAl bulk metallic glasses," *Advances in Materials Science and Engineering*, vol. 2022, Article ID 6528470, 8 pages, 2022.

[13] I. Patra, A. M. Abdulhadi, F. S. Fahim, B. S. Bashar, T. Alawsi, and M. Salmani, "The effects of temperature and impact velocity on the shock wave response of pore-embedded metallic glasses," *Advances in Materials Science and Engineering*, vol. 2022, Article ID 6111294, 8 pages, 2022.

[14] Z. Chen, Y. Xie, A. Datye et al., "Angstrom-scale replication of surfaces with crystallized bulk metallic glasses," *Materials Today Nano*, vol. 16, Article ID 100145, 2021.

[15] J. P. Singer, M. Gopinadhan, Z. Shao, A. D. Taylor, J. Schroers, and C. O. Osuji, "Nanoimprinting sub-100 nm features in a photovoltaic nanocomposite using durable bulk metallic glass molds," *ACS Applied Materials and Interfaces*, vol. 7, no. 6, pp. 3456–3461, 2015.

[16] X. Liang, P. Sharma, Y. Zhang, and H. Kato, "Nanoimprinting of magnetic FeCo-based metallic glass thin films," *Journal of Magnetism and Magnetic Materials*, vol. 542, Article ID 168455, 2022.

[17] L. Xiaoyu, P. Sharma, Y. Zhang, A. Makino, and H. Kato, "Nano-imprinting potential of magnetic FeCo-based metallic glass," *Nanotechnology*, vol. 30, Article ID 305302, 2019.

[18] M. Li, W. Luo, J. Xu, J. Zhang, K. W. Ng, and X. Cheng, "Fabrication and oxidation of amorphous Zr-based alloy for imprint lithography," *Microelectronic Engineering*, vol. 256, Article ID 111722, 2022.

[19] C. D. Wu and R. E. Li, "Effects of alloy composition, cavity aspect ratio, and temperature of imprinted ZrCu metallic glass films: a molecular dynamics study," *Applied Physics A*, vol. 126, no. 3, p. 209, 2020.

[20] D. Q. Doan, T. H. Fang, A. S. Tran, and T. H. Chen, "Residual stress and elastic recovery of imprinted Cu-Zr metallic glass films using molecular dynamic simulation," *Computational Materials Science*, vol. 170, Article ID 109162, 2019.

[21] C.-D. Wu and C.-J. Hou, "Molecular dynamics analysis of plastic deformation and mechanics of imprinted metallic glass films," *Computational Materials Science*, vol. 144, pp. 248–255, 2018.

[22] Y. Zhu, G. Liao, T. Shi, M. Li, Z. Tang, and F. Xiong, "Thermoplastic deformation and structural evolutions in nanoimprinting metallic glasses using molecular dynamics analysis," *Journal of Non-crystalline Solids*, vol. 427, pp. 46–53, 2015.

[23] J. P. Singer, C. I. Pelligra, N. Kornblum et al., "Multiscale patterning of a metallic glass using sacrificial imprint lithography," *Microsystems and Nanoengineering*, vol. 1, Article ID 15040, 2015.

[24] C. Wang, L. W. Nien, H. C. Ho, Y. C. Lai, and C. H. Hsueh, "Surface plasmon excited on imprintable thin-film metallic

glasses for surface-enhanced Raman scattering applications," *ACS Applied Nano Materials*, vol. 1, no. 2, pp. 908–914, 2018.

[25] C. D. Wu, "Atomistic simulation of nanoformed metallic glass," *Applied Surface Science*, vol. 343, pp. 153–159, 2015.

[26] A. S. Tran, D. Q. Doan, and V. T. Chu, "Molecular simulation study on mechanical properties and elastic recovery of nanoimprinted CuAgAu metallic glasses," *Journal of Non-crystalline Solids*, vol. 596, Article ID 121861, 2022.

[27] C. H. Wang, K. C. Chao, T. H. Fang, I. Stachiv, and S. F. Hsieh, "Investigations of the mechanical properties of nano-imprinted amorphous Ni–Zr alloys utilizing the molecular dynamics simulation," *Journal of Alloys and Compounds*, vol. 659, pp. 224–231, 2016.

[28] G. Kumar, J. Blawzdziewicz, and J. Schroers, "Controllable nanoimprinting of metallic glasses: effect of pressure and interfacial properties," *Nanotechnology*, vol. 24, no. 10, Article ID 105301, 2013.

[29] D. Lau, W. Jian, Z. Yu, and D. Hui, "Nano-engineering of construction materials using molecular dynamics simulations: prospects and challenges," *Composites Part B: Engineering*, vol. 143, pp. 282–291, 2018.

[30] D. Surblys, H. Matsubara, G. Kikugawa, and T. Ohara, "Application of atomic stress to compute heat flux via molecular dynamics for systems with many-body interactions," *Physical Review E*, vol. 99, no. 5, Article ID 51301, 2019.

[31] J. I. Odujole and S. Desai, "Molecular dynamics investigation of material deformation behavior of PMMA in nanoimprint lithography," *AIP Advances*, vol. 10, no. 9, Article ID 95102, 2020.

[32] H. W. Sheng, E. Ma, and M. J. Kramer, "Relating dynamic properties to atomic structure in metallic glasses," *Journal of Occupational Medicine*, vol. 64, no. 7, pp. 856–881, 2012.

[33] C. Braga and K. P. Travis, "A configurational temperature Nosé-Hoover thermostat," *The Journal of Chemical Physics*, vol. 123, no. 13, Article ID 134101, 2005.

[34] C. M. Meylan, F. Papparotto, S. Nachum et al., "Stimulation of shear-transformation zones in metallic glasses by cryogenic thermal cycling," *Journal of Non-crystalline Solids*, vol. 548, Article ID 120299, 2020.

[35] K. E. Avila, S. Küchemann, I. Alabd Alhafez, and H. M. Urbassek, "Shear-transformation zone activation during loading and unloading in nanoindentation of metallic glasses," *Materials*, vol. 12, no. 9, p. 1477, 2019.

[36] C. D. Wu, T. H. Fang, and J. F. Lin, "Effects of mold geometry and taper angles on the filling mechanism of a nanoimprinted polymer using molecular dynamics," *Applied Surface Science*, vol. 316, pp. 292–300, 2014.

[37] J. L. Gu, H. W. Luan, S. F. Zhao et al., "Unique energy-storage behavior related to structural heterogeneity in high-entropy metallic glass," *Materials Science and Engineering*, vol. 786, Article ID 139417, 2020.

[38] Y. Lou, X. Liu, X. Yang et al., "Fast rejuvenation in bulk metallic glass induced by ultrasonic vibration pre-compression," *Intermetallics*, vol. 118, Article ID 106687, 2020.

Hindawi
Advances in Materials Science and Engineering
Volume 2023, Article ID 5963742, 8 pages
https://doi.org/10.1155/2023/5963742

Research Article

Characterization of Plastic Deformation in CuZr Metallic Glasses Subjected to the Rolling Process

Ramaswamy Sivaraman,[1] Farag M. A. Altalbawy,[2,3] Alaa Mohammed Hussein Wais,[4] Holya A. Lafta,[5] and Seyedmasoud Hashemi[6]

[1]*Department of Mathematics, Dwaraka Doss Goverdhan Doss Vaishnav College, Arumbakkam, University of Madras, Chennai, India*
[2]*National Institute of Laser Enhanced Sciences (NILES), Cairo University, Giza 12613, Egypt*
[3]*Department of Chemistry, University College of Duba, Tabuk University, Duba 71911, Saudi Arabia*
[4]*Biomedical Engineering Department, Al-Mustaqbal University College, 51001 Hillah, Babil, Iraq*
[5]*Al-Nisour University College, Baghdad, Iraq*
[6]*Department of Chemistry, Iran University of Science and Technology (IUST), Tehran, Iran*

Correspondence should be addressed to Seyedmasoud Hashemi; smhashemi33@gmail.com

Received 3 August 2022; Revised 15 October 2022; Accepted 24 November 2022; Published 21 January 2023

Academic Editor: Shahin Khademinia

Copyright © 2023 Ramaswamy Sivaraman et al. This is an open access article distributed under the Creative Commons Attribution License, which permits unrestricted use, distribution, and reproduction in any medium, provided the original work is properly cited.

Using the rolling process, it is possible to induce multiple shear bands in the microstructure of metallic glasses (MGs) and improve the overall plasticity in the subsequent mechanical loadings. Hence, it is crucial to understand the mechanism of shear banding and plastic deformation under the rolling process. In this work, molecular dynamics (MD) simulation was applied to evaluate the formation and generation of shear bands in a CuZr MG under cold- and hot-rolling processes. Based on the results, it is found that the shear bands are formed with secondary branches in the cold rolling, while the shear events are scattered in the bulk of material in the hot rolling. Considering Voronoi analysis, it is revealed that the hot rolling is accompanied by the recovery of crystalline-like clusters provided that rolling process continues for subsequent passes. On the other hand, the cold-rolled sample shows a stable behavior in the evolution of crystalline-like clusters; however, the population of main icosahedral polyhedrons decreases in the system.

1. Introduction

Metallic glasses (MGs) are in the category of amorphous materials that are known to exhibit superior mechanical properties and excellent functional behaviors [1–4]. However, the poor ductility at room temperature is one of their drawbacks for application in the engineering systems [5–7]. It is generally accepted that the plastic deformation of MGs is occurred in the narrow sheared regions, named as shear bands, which is resulted from the sliding of energetically favorable defects under an external force [8–10]. Recently, many investigations have been conducted to mitigate the brittle behavior of MGs through the formation and interaction of multiple shear bands in the microstructure [11–14]. Although, a single shear band changes to a crack due to the severe strain localization, the multiple shear banding extends plastic deformation in the bulk of specimen [15–18]. Ebner et al. [19] indicated that the high pressure torsion (HPT) induced the extra shear strains in the amorphous structure, leading to improvement of plastic defamation. Boltynjuk et al. [20] reported that the HPT process intensified the structural heterogeneity and increased population of shear bands. In this state, the hardness and elastic modulus declined; however, the strain-rate sensitivity was enhanced in the MG. Astanin et al. [21, 22] revealed that the HPT process increased the shear band

density to more than 1.76 μm^{-1}, while the distance between shear bands were in the range of 80–120 μm. Li et al. [23] demonstrated that the introduction of prestrain and shear bands by one-directional cold rolling led to the significant improvement of fracture toughness in the ZrTiCuNiAl BMG. Moreover, the orientation of preshear bands played a major role in the final mechanical properties. Using molecular dynamics (MD) simulation, Zhao et al. [24] evaluated the influence of prestress on the plasticity and mechanical properties of CuZr MGs under the indenting process. Their results indicated that the morphologies of shear band were affected by the magnitude of prestress so that the catastrophic propagation of shear bands in the nanoindentation process was correlated to the large prestress values. Fan et al. [25] indicated that the 10% prestraining of ZrCuAl amorphous alloy increased the Helmholtz activation energy and generated the population of shear transformation zones (STZs), leading to homogenous plasticity under the subsequent external loading. Another investigation showed that the precold rolling decreased the population and magnitude of pop-ins in the load-displacement curves of nanoindentation test, resulting in a gradual transition from inhomogeneous to homogenous flow behavior [26]. Xie and Kruzic [27] reported that the precold rolling improved the fracture toughness more than 50%, which is due to the promotion of numerous shear bands along the main crack path in the rolled sample. Reddy et al. [13] reported that the hot rolling process induced the scattered thick shear bands in the sample, while the dense fine shear events were distributed in the microstructure under the cryo-rolling process. Scudino et al. [28] investigated the role cold rolling on the mechanical behavior of ZrTiCuNiAl BMG and found that the small plastic strain applied by the pretreatment was efficient for enhancing the plastic deformation under the compressive or tensile loadings. It is a proven idea that the prerolling process is an efficient method for improving the plastic deformation in the MGs. However, the identification of shear-banding in the rolled samples has been a hot topic for tuning the plastic deformation and ultimate strength. In this paper, we aimed to characterize the evolution of shear bands in the rolled MGs and show that how the parameters of rolling process (cold or hot) change the shear-banding features.

2. Modeling and Simulation

2.1. Sample Preparation. The simulation box of $Cu_{54}Zr_{46}$ composition with the dimensions of $30 \times 18 \times 12\,nm^3$ was firstly modeled by the Large-scale Atomic/Molecular Massively Parallel Simulator (LAMMPS) and with the consideration of atomic interactions described through the embedded atom method (EAM) potential [29]. For this purpose, the atomic box was heated to 2000 K and held in a molten state for 2 ns, and then it was cooled down to 300 K with the cooling rate of 10^{11} K/s. It should be noted that the sample preparation was conducted under the NPT ensemble and periodic boundary conditions and time step of 1 fs. It is worth to note that it is possible to simulate a wide range of CuZr composition and prepare various MGs through the MD method. However, we selected the $Cu_{54}Zr_{46}$ composition with the moderate mechanical properties in the CuZr system [30–32].

2.2. Nano-Rolling Process. In the nano-rolling process, two sets of rigid rotating rollers were prepared to reduce the sample thickness for 8% and 12%, respectively (See Figure 1). The lower and upper rollers for both of sets rotated (0.003 rot.·ps^{-1}) in the clockwise and anticlockwise directions, respectively. The first step to model the rolling process is to create the rollers with cylindrical geometry with specified dimensions [13]. The rollers were considered as rigid bodies, meaning that they became quite immune to any plastic deformation in the rolling process. The details of rollers including the dimensions are given in Figure 1. After the creation of rollers, the MG sample moved to the rolling system with a constant velocity of 0.1 nm/ps. The x, y, and z directions in the rolling system were considered as rolling direction (RD), transverse direction (TD), and normal direction (ND), respectively. The shrink-wrapped boundary condition was considered along the transverse direction. Prior to the rolling process, the whole system was relaxed by conjugate gradient technique [33]. The temperatures for the process were kept at 300 K and 650 K, providing conditions for evaluation of cold rolling and hot rolling in the MGs. To achieve a stable system, the temperature was equilibrated under microcanonical ensemble [13]. The Nosé–Hoover thermostat was used to maintain the temperature at the certain values [34]. OVITO package was also employed to visualize the evolution of system under the rolling process [35].

3. Results and Discussion

Figure 2(a) represents the snapshots of shear strain at the normal direction (ND) during the cold rolling (300 K). Moreover, the distribution of shear strain for selected regions are plotted in Figure 2(b). Considering the first stage of rolling process, the plastic deformation is accompanied with the low density and weak generation of shear bands in the microstructure, which is owing to the small percentage of thickness reduction (8%). The strain map also shows that the orientation of shear bands is mainly in the range of 43°–47°. Passing through the second stage of rolling process, the density of shear bands enhances in the system, leading to the high intensification of strained regions. It is suggested that the accumulation of previously-formed shear bands along with the formation of new ones are the main sources of the plastic deformation during the second stage [13]. The mechanism of shear band formation and propagation in our study is similar to that reported in other works focusing on the experimental procedures [36, 37]. Figure 2(b) shows the variations of shear strain in the selected regions. The lines A and C belong to the sides of sample, while the line B introduces the evolution of strain at the middle section of sample. Considering the first stage of rolling process, one can see that the curves of A and C exhibit a uniform trend, in which the strain is maximum at the bottom and top regions,

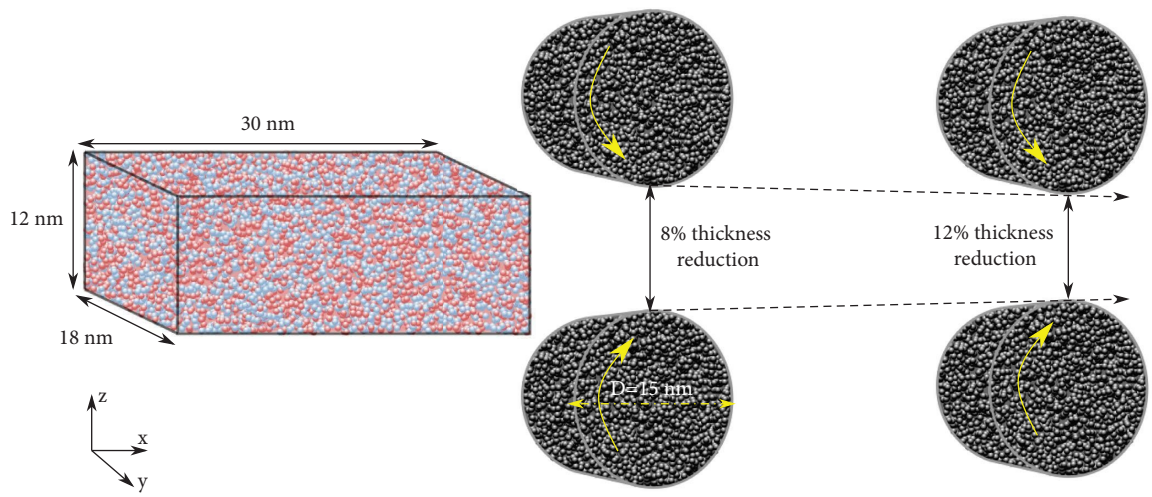

Figure 1: Schematic of rolling process for CuZr MG plate.

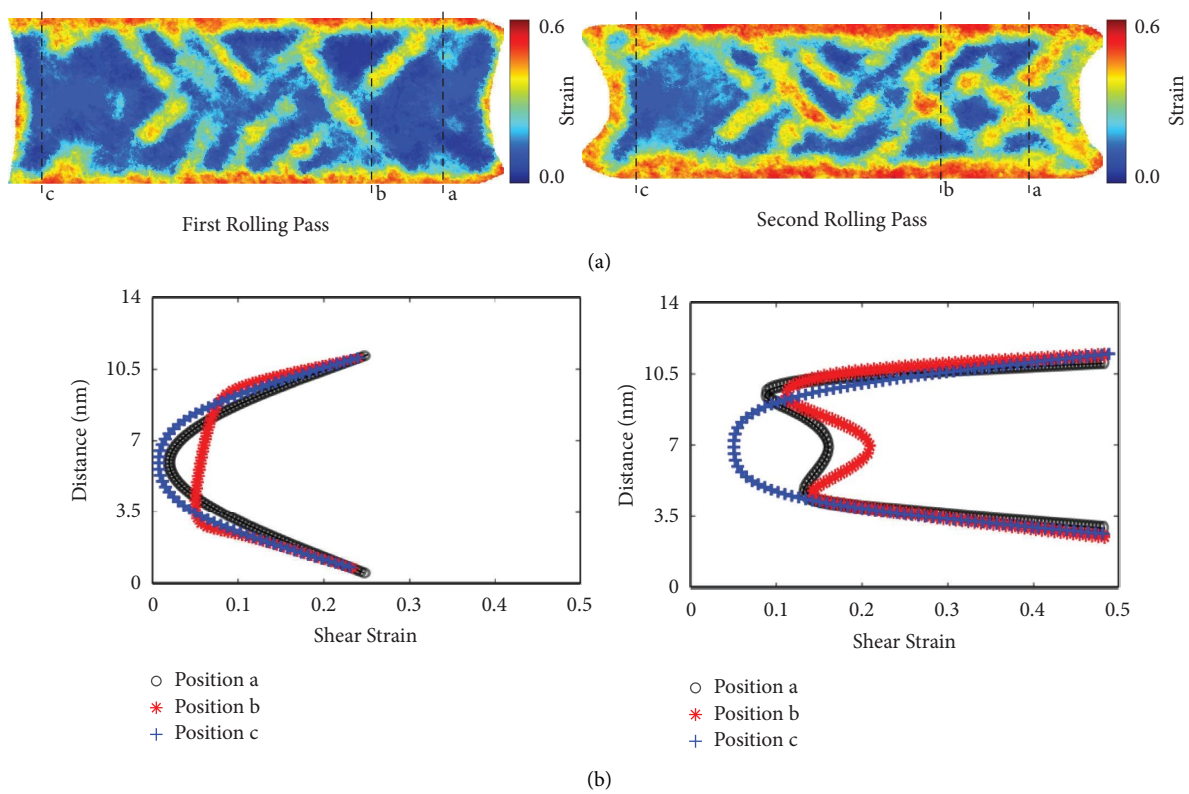

Figure 2: (a) The snapshots of shear strain at the normal direction (ND) during the cold rolling, (b) the linear distribution of shear strain for selected regions.

while the center part includes the minimum strain. The line *B* exhibits a different strain curve with a hump at the center of sample. This event implies that the main shear banding occurs at the center of sample in the position *B*; however, the sheared strain at the sides of sample; i.e. positions *A* and *C*, is mainly restricted near the surfaces. It is suggested that the atoms are constrained at the middle part of sample leading to the strain accumulation at the normal direction and shear band propagation at the center part. On the other hands, the atoms at the sides of the sample can establish cooperative movements at the rolling direction and created strain regions near the surface of sample. Passing through the second stage of rolling process, a higher strain values are accumulated in the bulk of sample, leading to the creation of strain humps in the curves *A* and *B*. This result indicates that the center part of sample is accumulated with the extreme sheared regions, compared with the first stage of rolling process. Moreover, it is observed that all of the strain curves shift to the right side, indicating the total increment of plastic deformation after the second stage of rolling process.

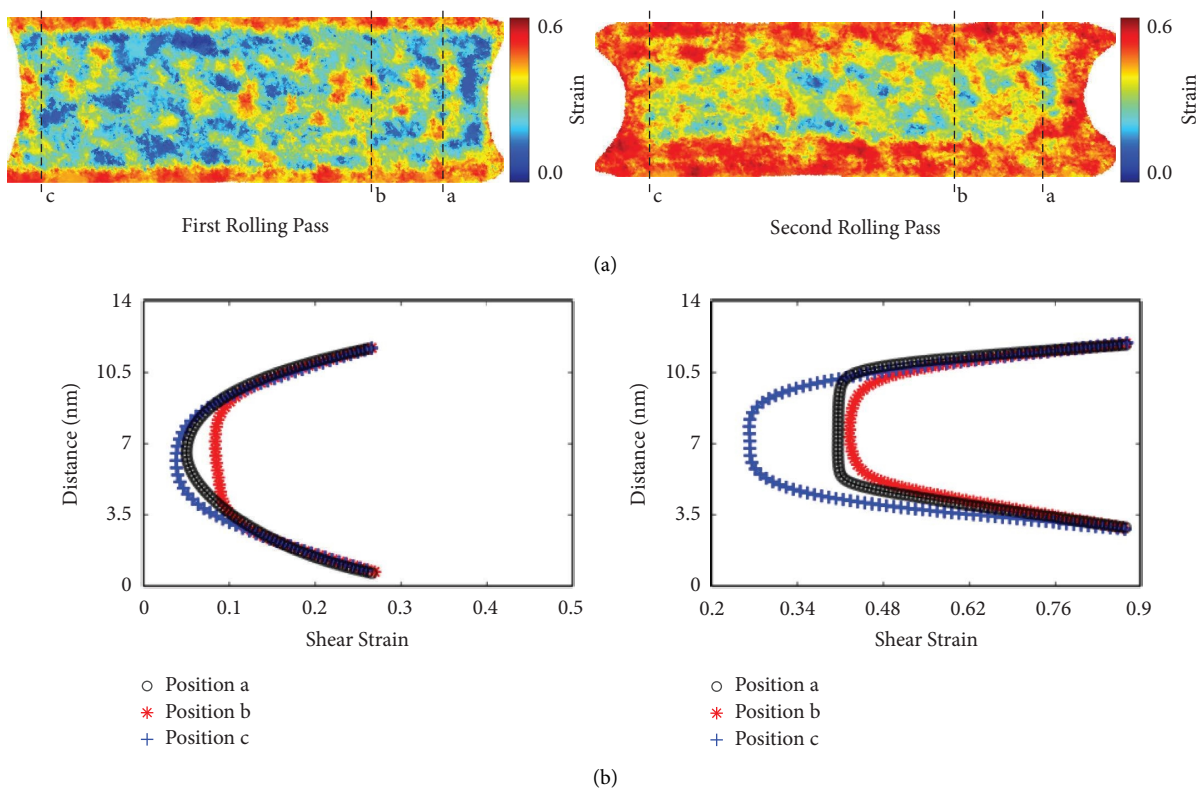

Figure 3: (a) The snapshots of shear strain at the normal direction (ND) during the hot rolling, (b) the linear distribution of shear strain for selected regions.

Figure 3(a) indicates the shear strain snapshots of MG sample rolled in two stages at 650 K. Figure 3(b) shows the variations of shear strain in the selected regions. Compared to the cold rolling, the shear strain was randomly distributed in the microstructure. It is apparent that the density of shear bands is lower in the hot rolling, meaning that the elevated temperature led to the high thermal activity of atoms in the system. Moreover, after the second rolling stage, one can see that the density of shear bands is still low. The trend of strain in the selected regions also shows that there is no sign of serious hump in the curves for both stages of rolling process, implying that the shear banding is not prevailing in the center of specimen at high temperatures. This phenomenon was also detected in other works [13, 38]. Nevertheless, one should note that the shift of curves to the right side at the second stage is much more than the cold rolling process. This means that plastic deformation in the hot rolling process is more homogenous and the nanoscale shear events are randomly distributed in the structure.

In the following, the structural evolution in the cold- and hot-rolled samples is compared and the details of shear-banding mechanism are presented. Figure 4(a) illustrates the atomic strain tensor along the rolling direction for the regions involved with the shear process. According to the results, the cold rolling is accompanied with the formation of primary shear bands with a few second branching evolution. On the other side, the shear transformation zones are homogeneously dispersed in the hot-rolled sample, indicating the uniform plastic deformation, compared to the cold rolling condition. To make a detailed comparison, we evaluated the rotation of the atomic displacement vector, affecting the mechanism of shear banding in the system. Recently, it has been reported that the type of movement and rotation of atoms in the vicinity of shear bands are different from the nonstrained zones [39]. Figure 4(b) represents the scatter data correlating the displacement vector rotations to the atomic shear strain of regions involved in the shear banding. One can see that the rotation angles in the hot rolling is more sporadic in comparison with the cold rolling. Moreover, there are more atomic rearrangements with higher shear strain and rotation angles in deformed part of the hot-rolled sample. This result is consistent with this fact that the higher thermal activity at the elevated temperature enhances the atomic movements, leading to the intensification of displacement vector rotation in a certain shear strain. Figure 4(c) shows the polynomial fitting of the data along with the regression values for cold and hot rolling processes. This information provides conditions for evaluation of the variability from the average value. According to the results, the hot rolling exhibits a lower regression value, demonstrating that the generation of nanoscale strain at elevated temperature is accompanied with the higher displacement and rotation of atoms in the system.

The application of loading in the rolling process induces the plastic deformation and changes the atomic rearrangement in the microstructure [14, 37, 40]. In this investigation, the Voronoi analysis was carried out to find out how the rolling process alters the population of atomic

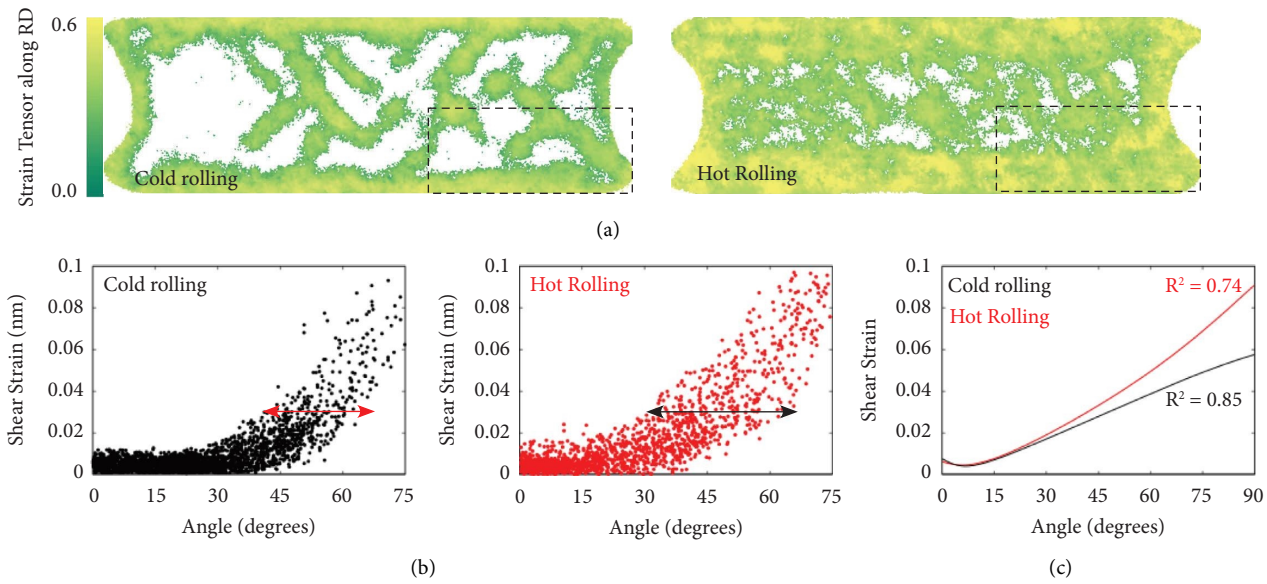

Figure 4: (a) Strain tensor snapshots of the rolled samples under cold-and hot rolling conditions, (b) shear strain as a function of displacement angle, (c) polynomial fitting of the plots given in part b.

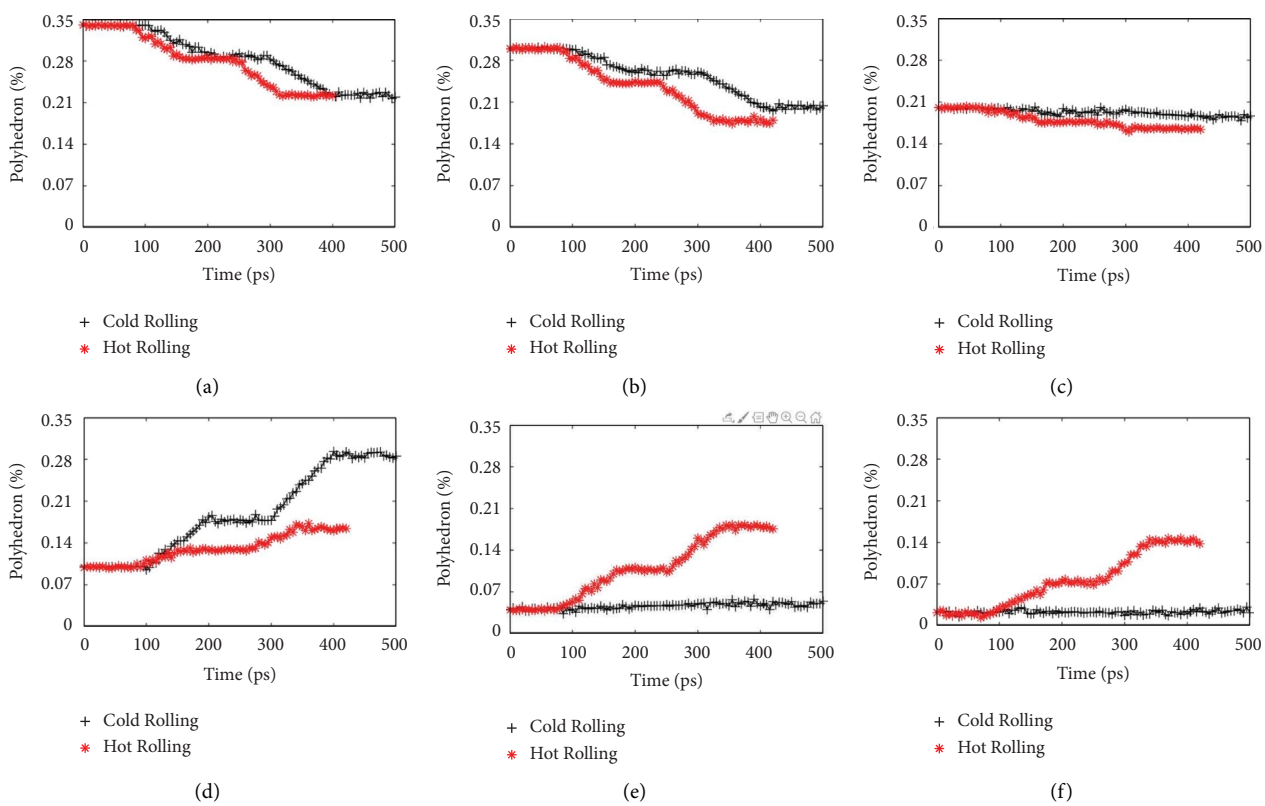

Figure 5: Fraction of main polyhedrons as a function of rolling time for (a) <0 0 12 0> (b) <0 2 8 1> (c) <0 1 10 2>, (d) <0 3 6 3 >, (e) <0 4 4 5> and (f) <0 4 4 6>.

clusters [41, 42]. Figure 5 gives the normalized fraction of main coordination polyhedrons under the overall time of nano-rolling at 300 K and 650 K. Firstly, it is observed that there is a plateau part in the plots for all of the conditions. This plateau is associated to the time between the first and second stages of rolling process, in which no compressive load is applied to the sample. As a result, the change in the polyhedron fraction remains constant. Secondly, one should note that many works have shown that the CuZr MGs include numerous types of polyhedrons [43, 44]. In this work,

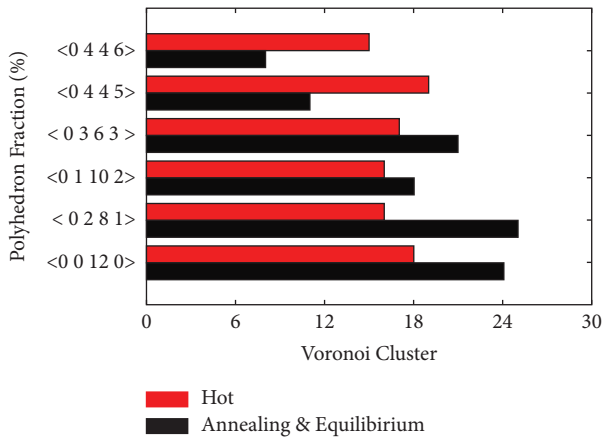

Figure 6: The percentage of main voronoi clusters in the hot rolled and annealed samples.

we selected the main ones comprising the most fraction of clusters as the icosahedral-like clusters and crystal-like clusters in the system. Based on the results, the backbone structure of CuZr sample is dominated by the icosahedral-like clusters with the indices of <0 0 12 0>, <0 2 8 1>, and <0 1 10 2>. Under the rolling process, the polyhedral fractions are markedly changed in the system. In the cold rolling process, a significant decrease occurs in the fraction of <0 0 12 0 > and <0 2 8 1> polyhedrons, while the polyhedron <0 3 6 3 > is mainly recovered. Moreover, polyhedrons <0 1 10 2>, <0 4 4 5>, and <0 4 4 6> show a stable trend during the cold rolling. On the other hand, the crystalline-like polyhedrons, i.e. <0 4 4 5> and <0 4 4 6>, show an increasing trend during the hot rolling process. This outcome indicates that the CuZr MG tends to lose its amorphous nature so that with the rise of thickness reduction, the crystallization may occur in the system [13]. To be sure about our idea, we treated the raw MG sample at 650 K for 1 ns and evaluated the variations of Voronoi polyhedrons after the equilibration. As can be seen in Figure 6, the hot rolling process has more effective in the disintegration of cluster types in the atomic configuration. Moreover, the fractions of polyhedrons <0 4 4 5> and <0 4 4 6> in the relaxed sample are considerably less than the hot-rolled condition. This analysis validates that the application of loading at high temperature influences the amorphous nature of MG sample through the insertion of extra energy into the system, providing energy barrier for crystallization in the microstructure.

4. Conclusion

The cold and hot rolling processes have been carried out to characterize the mechanism of shear banding and plastic deformation in the CuZr MG samples. In accordance with the outcomes of MD simulation, the following conclusions are drawn as follows:

(a) For both of cold and hot states, the density and population of shear bands were limited in the first pass of rolling process, which was due to the lower percentage of thickness reduction. In the second pass, the plastic deformation was extended in the material, which was due to the formation of new shear bands and growth of previous ones.

(b) The local evaluation of strain distribution showed that the cold rolling process was accompanied with the generation of shear bands through the center of sample, while a homogenous shear-strain distribution was observed in the normal direction for the hot-rolled sample.

(c) Considering Voronoi analysis, it is revealed that the hot rolling led to the recovery of crystalline-like clusters, meaning that the glassy structure tends to form crystalline phases. On the other hand, the cold-rolled sample showed a decrease in the population of main icosahedral polyhedrons, while the evolution of crystalline-like clusters remained stable.

Data Availability

All data is available in the manuscript.

Conflicts of Interest

The authors declare that there are no conflicts of interest.

References

[1] Y. Zhang, J. Li, Q. Zhang, S. Ding, W. Wu, and R. Xia, "Tetrachiral nanostructured metallic glasses with mechanically tunable performance," *Materials Chemistry and Physics*, vol. 276, Article ID 125315, 2022.

[2] X. Zhang, L. Lai, S. Xiao et al., "Effect of W on the thermal stability, mechanical properties and corrosion resistance of Fe-based bulk metallic glass," *Intermetallics*, vol. 143, Article ID 107485, 2022.

[3] J. Wegner, M. Frey, M. Piechotta et al., "Influence of powder characteristics on the structural and the mechanical properties of additively manufactured Zr-based bulk metallic glass," *Materials & Design*, vol. 209, Article ID 109976, 2021.

[4] R. Sivaraman, I. Patra, Z. M. Najm, N. M. Hameed, T. Alawsi, and S. Hashemi, "The effects of minor element addition on the structural heterogeneity and mechanical properties of ZrCuAl bulk metallic glasses," *Advances in Materials Science and Engineering*, vol. 2022, pp. 1–8, 2022.

[5] Y. Lu, S. Su, S. Zhang et al., "Controllable additive manufacturing of gradient bulk metallic glass composite with high strength and tensile ductility," *Acta Materialia*, vol. 206, Article ID 116632, 2021.

[6] R. M. O. Mota, E. T. Lund, S. Sohn et al., "Enhancing ductility in bulk metallic glasses by straining during cooling," *Commun. Mater.*vol. 2, pp. 23–28, 2021.

[7] H. Wang, W. Dmowski, Y. Tong et al., "Nonaffine strains control ductility of metallic glasses," *Physical Review Letters*, vol. 128, no. 15, Article ID 155501, 2022.

[8] X. Mu, M. R. Chellali, E. Boltynjuk et al., "Unveiling the local atomic arrangements in the shear band regions of metallic glass," *Advanced Materials*, vol. 33, no. 12, Article ID 2007267, 2021.

[9] X. Li, R. Qu, W. Rao, and X. Jiang, "A new idea of modeling shear band in metallic glass based on the concept of distributed dislocation," *Journal of Non-crystalline Solids*, vol. 577, Article ID 121328, 2022.

[10] I. Patra, A. M. Abdulhadi, F. S. Fahim, B. S. Bashar, T. Alawsi, and M. Salmani, "The effects of temperature and impact velocity on the shock wave response of pore-embedded metallic glasses," *Advances in Materials Science and Engineering*, vol. 2022, pp. 1–8, 2022.

[11] A. Jain, Y. Prabhu, D. Gunderov, E. Ubyivovk, and J. Bhatt, "Study of micro indentation assisted deformation on HPT processed Zr62Cu22Al10Fe5Dy1 bulk metallic glass," *Journal of Non-crystalline Solids*, vol. 566, Article ID 120877, 2021.

[12] K. Nomoto, B. Li, C. Gammer et al., "Deformation-induced medium-range order changes in bulk metallic glasses," *Physical Review Materials*, vol. 6, no. 4, Article ID 043603, 2022.

[13] K. V. Reddy and S. Pal, "Recreating the shear band evolution in nanoscale metallic glass by mimicking the atomistic rolling deformation: a molecular dynamics study," *Journal of Molecular Modeling*, vol. 27, pp. 220–228, 2021.

[14] S. Scudino, "Mechanism of shear banding during cold rolling of a bulk metallic glass," *Journal of Alloys and Compounds*, vol. 773, pp. 883–889, 2019.

[15] X. Lu, S. Feng, L. Li et al., "Severe deformation-induced microstructural heterogeneities in Cu64Zr36 metallic glass," *Modelling and Simulation in Materials Science and Engineering*, 2022.

[16] V. S. Zolotorevsky, A. I. Bazlov, A. G. Igrevskaya, A. S. Aronin, G. E. Abrosimova, and D. V. Louzguine-Luzgin, "Significant mechanical softening of an Al-Y-Ni-Co metallic glass on cold and hot rolling," *Journal of Occupational Medicine*, vol. 71, no. 11, pp. 4079–4085, 2019.

[17] A. Gunti, P. P. Jana, M.-H. Lee, and J. Das, "Effect of Cold Rolling on the Evolution of Shear Bands and Nanoindentation Hardness in Zr41.2Ti13.8Cu12.5Ni10Be22.5 Bulk Metallic Glass," *Nanomaterials*, vol. 11, 2021.

[18] K. E. Avila, S. Küchemann, and H. M. Urbassek, "Interaction between parallel shear bands in a metallic glass," *Journal of Non-crystalline Solids*, vol. 566, Article ID 120882, 2021.

[19] C. Ebner, B. Escher, C. Gammer, J. Eckert, S. Pauly, and C. Rentenberger, "Structural and mechanical characterization of heterogeneities in a CuZr-based bulk metallic glass processed by high pressure torsion," *Acta Materialia*, vol. 160, pp. 147–157, 2018.

[20] E. Boltynjuk, D. Gunderov, E. Ubyivovk et al., "Enhanced strain rate sensitivity of Zr-based bulk metallic glasses subjected to high pressure torsion," *Journal of Alloys and Compounds*, vol. 747, pp. 595–602, 2018.

[21] V. Astanin, D. Gunderov, Z. Q. Ren, R. Valiev, and J. T. Wang, "High density of shear bands in the Vitreloy bulk metallic glass subjected to high-pressure torsion," *IOP Conference Series Materials Science and Engineering*, vol. 1008, no. 1, Article ID 012031, 2020.

[22] D. V Gunderov, V. V Astanin, A. V Sharafutdinov, and J. Bhatt, "Slippage during high-pressure torsion processing of Vitreloy 105 bulk metallic glass," *Journal of Physics: Conference Series*, vol. 1967, Article ID 12062, 2021.

[23] B. Li, S. Scudino, B. Gludovatz, and J. J. Kruzic, "Role of pre-existing shear band morphology in controlling the fracture behavior of a Zr–Ti–Cu–Ni–Al bulk metallic glass," *Materials Science and Engineering A*, vol. 786, p. 139396, Article ID 139396, 2020.

[24] D. Zhao, B. Zhu, S. Wang, Y. Niu, L. Xu, and H. Zhao, "Effects of pre-strain on the nanoindentation behaviors of metallic glass studied by molecular dynamics simulations," *Computational Materials Science*, vol. 186, Article ID 110073, 2021.

[25] H. Fan, N. Wang, C. He, Y. Huang, Z. Ning, and J. Sun, "Effect of pre-straining on the structure and nano-mechanical properties of a CuZrAl bulk metallic glass," *Journal of Alloys and Compounds*, vol. 918, Article ID 165635, 2022.

[26] A. Gunti and J. Das, "Effect of cold rolling on the serrated flow behavior of Zr41.2Ti13.8Cu12.5Ni10Be22.5 bulk metallic glass during nanoindentation," *Journal of Materials Research*, vol. 37, no. 4, pp. 976–989, 2022.

[27] S. Xie and J. J. Kruzic, "Cold rolling improves the fracture toughness of a Zr-based bulk metallic glass," *Journal of Alloys and Compounds*, vol. 694, pp. 1109–1120, 2017.

[28] S. Scudino, B. Jerliu, K. B. Surreddi, U. Kühn, and J. Eckert, "Effect of cold rolling on compressive and tensile mechanical properties of Zr52.5Ti5Cu18Ni14.5Al10 bulk metallic glass," *Journal of Alloys and Compounds*, vol. 509, pp. 128–130, 2011.

[29] M. I. Mendelev, M. J. Kramer, R. T. Ott, D. J. Sordelet, D. Yagodin, and P. Popel, "Development of suitable interatomic potentials for simulation of liquid and amorphous Cu–Zr alloys," *Philosophical Magazine*, vol. 89, no. 11, pp. 967–987, 2009.

[30] C. Tang and C. H. Wong, "Effect of atomic-level stresses on local dynamic and mechanical properties in CuxZr100−x metallic glasses: a molecular dynamics study," *Intermetallics*, vol. 58, pp. 50–55, 2015.

[31] M. Imran, F. Hussain, M. Rashid, Y. Cai, and S. A. Ahmad, "Mechanical behavior of Cu—Zr bulk metallic glasses (BMGs): a molecular dynamics approach," *Chinese Physics B*, vol. 22, no. 9, Article ID 096101, 2013.

[32] C. D. Wu, "Molecular dynamics simulation of nanotribology properties of CuZr metallic glasses," *Applied Physics A*, vol. 122, no. 4, p. 486, 2016.

[33] S. Plimpton, "Fast parallel algorithms for short-range molecular dynamics," *Journal of Computational Physics*, vol. 117, pp. 1–19, 1995.

[34] C. Braga and K. P. Travis, "A configurational temperature Nosé-Hoover thermostat," *The Journal of Chemical Physics*, vol. 123, no. 13, Article ID 134101, 2005.

[35] A. Stukowski, "Visualization and analysis of atomistic simulation data with OVITO–the Open Visualization Tool," *Modelling and Simulation in Materials Science and Engineering*, vol. 18, no. 1, Article ID 015012, 2009.

[36] K. Song, S. Pauly, Y. Zhang et al., "Significant tensile ductility induced by cold rolling in Cu47. 5Zr47. 5Al5 bulk metallic glass," *Intermetallics*, vol. 19, no. 10, pp. 1394–1398, 2011.

[37] M. Stolpe, J. J. Kruzic, and R. Busch, "Evolution of shear bands, free volume and hardness during cold rolling of a Zr-based bulk metallic glass," *Acta Materialia*, vol. 64, pp. 231–240, 2014.

[38] R. Martinez, G. Kumar, and J. Schroers, "Hot rolling of bulk metallic glass in its supercooled liquid region," *Scripta Materialia*, vol. 59, no. 2, pp. 187–190, 2008.

[39] S. Feng, L. Qi, L. Wang et al., "Atomic structure of shear bands in Cu64Zr36 metallic glasses studied by molecular dynamics simulations," *Acta Materialia*, vol. 95, pp. 236–243, 2015.

[40] H. Yan, Y. Hu, Z. Yan, X. Zheng, and Y. Li, "Microstructure evolution of Zr50Cu18Ni17Al10Ti5 bulk metallic glass during cold-rolling," *Journal of Materials Science & Technology*, vol. 28, no. 8, pp. 756–760, 2012.

[41] W. Cui, J. Pan, D. J. Blackwood, and Y. Li, "Voronoi volume recovery during plastic deformation in deep-notched metallic glasses," *Journal of Alloys and Compounds*, vol. 776, pp. 460–468, 2019.

[42] S. Trady, M. Mazroui, A. Hasnaoui, and K. Saadouni, "Molecular dynamics study of atomic-level structure in

monatomic metallic glass," *Journal of Non-crystalline Solids*, vol. 443, pp. 136–142, 2016.

[43] N. Amigo and F. Valencia, "Mechanical and structural assessment of CuZr metallic glasses rejuvenated by thermal-pressure treatments," *Computational Materials Science*, vol. 198, Article ID 110681, 2021.

[44] N. Amigo, F. Urbina, and F. Valencia, "Shear transformation zones structure characterization in Cu50Zr50 metallic glasses under tensile test," *Computational Materials Science*, vol. 184, Article ID 109941, 2020.

Hindawi
Advances in Materials Science and Engineering
Volume 2022, Article ID 5168629, 9 pages
https://doi.org/10.1155/2022/5168629

Research Article

Influence of Microalloying Process on Dynamic Mechanical Relaxation of ZrCo-Based Amorphous Alloy

Rosario Mireya Romero Parra,[1] Indrajit Patra,[2] Fatima Safaa Fahim,[3] Samar Emad Izzat,[4] Ali Thaeer Hammid,[5] and Saeed Razavinejad[6]

[1]*Department of General Studies, Universidad Continental, Lima, Peru*
[2]*NIT Durgapur, Durgapur, West Bengal, India*
[3]*Anesthesia Techniques Department, Al-Mustaqbal University College, Babylon, Iraq*
[4]*Pharmacy Department, Al-Nisour University College, Baghdad, Iraq*
[5]*Computer Engineering Techniques Department, Faculty of Information Technology, Imam Ja'afar Al-Sadiq University, Baghdad, Iraq*
[6]*Department of Mechanical Engineering, Islamic Azad University, Isfahan, Iran*

Correspondence should be addressed to Saeed Razavinejad; saeedrazavinejad.ac@gmail.com

Received 27 May 2022; Revised 1 August 2022; Accepted 8 August 2022; Published 13 September 2022

Academic Editor: Majid Samavatian

Copyright © 2022 Rosario Mireya Romero Parra et al. This is an open access article distributed under the Creative Commons Attribution License, which permits unrestricted use, distribution, and reproduction in any medium, provided the original work is properly cited.

In this study, the dynamic mechanical spectroscopy was used to characterize the effects of minor Ni addition on the relaxation behavior of ZrCoAl bulk metallic glass (BMG). For this purpose, the Kohlrausch–Williams–Watts (KWW) function and quasi-point defect (QPD) model were used for evaluation of relaxation under the different aging temperatures. The results indicated that the Ni addition shifted the relaxation process to the higher temperatures. Moreover, the estimations showed that the activation energy of relaxation was 5.951 eV and 6.205 eV for ZrCoAl and ZrCoAlNi, respectively. It was also revealed that the microalloying process enhanced the structural defects in the system and led to the improvement of dynamic heterogeneity in the BMG. Comparing the physical models, it is suggested that a small change in the structural defects intensifies the dynamic heterogeneity in the material.

1. Introduction

Owing to their amorphous structure, bulk metallic glasses (BMGs) exhibit unique rheological and mechanical properties, opening up many possibilities to apply them in advanced engineering systems [1–4]. However, despite their crystalline counterparts, BMGs show complex relaxation behaviors making it necessary to precisely evaluate their glassy microstructure [5–8]. Among several techniques, dynamic mechanical analysis (DMA) is one of the efficient methods for identification and study of mechanical relaxation in the glassy alloys [9–12]. The studies indicated that the mechanical spectroscopy can reveal the dynamic relaxation of BMGs under different states such as rejuvenation, annealing, thermal variations, and compositional changes [13–16]. Among them, the role of minor addition on the dynamic relaxation of amorphous alloys can be easily analyzed through the DMA experiment [17–19]. To provide some examples, Tao et al. [20] indicated that the minor addition of Dy into the ZrCuAl BMG improved the structural heterogeneity and intensified the dynamic relaxation in the glassy system. Raya et al. [21] applied DMA to conduct strain-rate jump test for ZrCoAl(Si) BMGs. Their results demonstrated that the Si microalloying process weakened the sensitivity of amorphous alloy to the flow stresses and enhanced the structural stability under the rise of temperature and strain rate. Using the DMA method, Xu et al. [22] found that the addition of 10 at.% Nb into the CuZr glassy alloy improved the relaxation enthalpy through the change of local atomic movement from a smaller region

to a larger region. In another work, Qiao et al. [23] reported that the Fe addition into the ZrCuAlNi BMG led to decrement of Kohlrausch exponent and increase of characteristic relaxation time. Liu et al. [14] unveiled that the proper addition of Co and Cu into the LaCeAl glassy alloy intensified the secondary β relaxation and increased the glass transition temperature. The effects of Al and Nb microalloying process on the dynamic relaxation of $Zr_{20}Cu_{20}Ni_{20}Ti_{20}Hf_{20}$ high-entropy BMG were also evaluated through the mechanical spectroscopy [24]. The results unveiled that the activation energy of β relaxation for the Nb-added BMG was significantly higher, which was derived from the generation of severe chemical heterogeneity in the atomic structure. In another study, it was found that the Pd addition into the ZrCuAgAl BMG retarded the relaxation dynamics, which was indicative of defect-concentration reduction in the structure [25]. Previously, it was found that the Ni addition enhanced the total negative heat of mixing and changed the atomic arrangement and population of clusters in the ZrCoAl system, leading to the improvement of glass forming ability and structural heterogeneity [26]. Hence, it is concluded that the Ni element can be a proper minor addition for identification of dynamic response in the ZrCoAl MGs. In the current research, we aimed to focus on the characterization of dynamic relaxation evolution in a ZrCoAl BMG and indicate the importance of Ni microalloying process on the mechanical response of the glassy alloy in different conditions.

2. Experimental Procedure

In this study, $(Zr_{62}Co_{28}Al_{10})_{100\text{-}X}Ni_X$ (X = 0, 3 at.%) alloying compositions were considered for the fabrication. The negative heat of mixing for Ni-Al and Ni-Zr pairs is -22 kJ/mol and -49 kJ/mol [26], respectively, indicating that the Ni addition may improve the total heat of mixing and the structural disordering in the system. The mentioned alloys were firstly prepared by arc-melting process under the pure argon atmosphere. It should be noted that each master alloy was re-melted four times to obtain a homogenous chemical composition. Afterwards, the copper-mold suction casting was applied to fabricate BMGs in the form of plate samples with dimensions of 40 mm × 10 mm × 2 mm. To ensure the amorphousness of prepared samples, X-ray diffraction (XRD-Ultima IV) analysis was carried out at room temperature in the range of $2\theta = 25–90^\circ$. To characterize the thermal features of samples, the differential scanning calorimetry (DSC, TA instruments, 2500) was conducted under a high-purity dry argon environment with heating/cooling rates of 20 K/min. The measurement of relaxation enthalpy was carried out through the heating of sample beyond the glass transition temperature. After that a cooling process was performed to the room temperature. This cooling process was followed by a reheating stage with the identical heating rate. By subtracting the first and second thermal curves, the relaxation region is detected, which is consistent with the enthalpy of relaxation for samples. The dynamic mechanical analysis (DMA-Q800) was also performed in order to study the mechanical relaxation behavior of BMGs as function of frequency and temperature. This experiment was done under a protective atmosphere and different frequency and temperature ranges. From the attained data, the important parameters such as loss modulus (E″) and storage modulus (E′) were calculated [27]. The loss modulus is a criterion for evaluation of energy dissipation in an elastic excitation, while storage modulus is indicative of material ability to store energy elastically [28].

3. Results and Discussion

Figure 1(a) represents the XRD patterns of ZrCoAl and ZrCoAlNi samples with $2\theta = 25–90^\circ$. The results indicated that the XRD patterns included a broad peak with a smooth shoulder, implying the amorphous nature of samples. The DSC curves of samples are also given in Figure 1(b). As observed, the supercooled liquid range ($\Delta T_x = T_x - T_g$) in the ZrCoAl and Ni-added samples is 24 K and 32 K, respectively. The supercooled liquid range is a criterion for thermal stability and shows how easily a glassy alloy can be obtained after solidification. The enthalpy of relaxation is measured about 0.43 kJ/mol and 0.48 kJ/mol for the ZrCoAl and Ni-added samples, respectively. It is concluded that the minor Ni addition not only improves the thermal stability and glass formation but also is a key factor for the enhancement of stored energy in the atomic structure.

To characterize the relaxation processes, the dynamic mechanical response of samples was measured in a wide range of temperature under the heating rate of 5 K/min and driving frequency of 1 Hz. Figure 2(a) represents the normalized E'' and E' values for the ZrCoAl sample, while the loss factor ($\tan\delta = E''/E'$) for both of BMGs is given in Figure 2(b). According to the results, three distinct regions can be detected in the mechanical relaxation curve of ZrCoAl sample. At the first region (300 K–600 K), the loss modulus is low while the storage modulus is in its maximum state. In the temperature range of 600 K–730 K, the loss and storage moduli show the sharp increasing and decreasing trends, respectively. This event is associated to the β and α relaxations, occurring under the glass transition temperature [29, 30]. Finally, the contradictory behavior of moduli above 770 K is correlated to the nucleation and growth of crystals in the microstructure [25]. Using loss factor, it is possible to find out how the Ni microalloying process can change the relaxation behavior of ZrCoAl BMG. As given in Figure 2(b), the minor Ni addition leads to intensification of loss factor; however, a shift is detected in the peak of loss factor to the higher temperature, which is consistent with the DSC results in which the exothermic peak moves to the higher temperature for the Ni-added sample. There are also some published works showing the effects of minor addition on the deferment and intensification of relaxations in the glassy structures [9, 23, 31]. The intensification of relaxation is due to the increase of atomic mobility and free volumes.

The evaluation of mechanical relaxation on the different driving frequencies also gives important information about the activation energy of relaxation processes in the samples. As illustrated in Figure 3, the rise in the driving frequency leads to the shift of α-relaxation peak to the higher

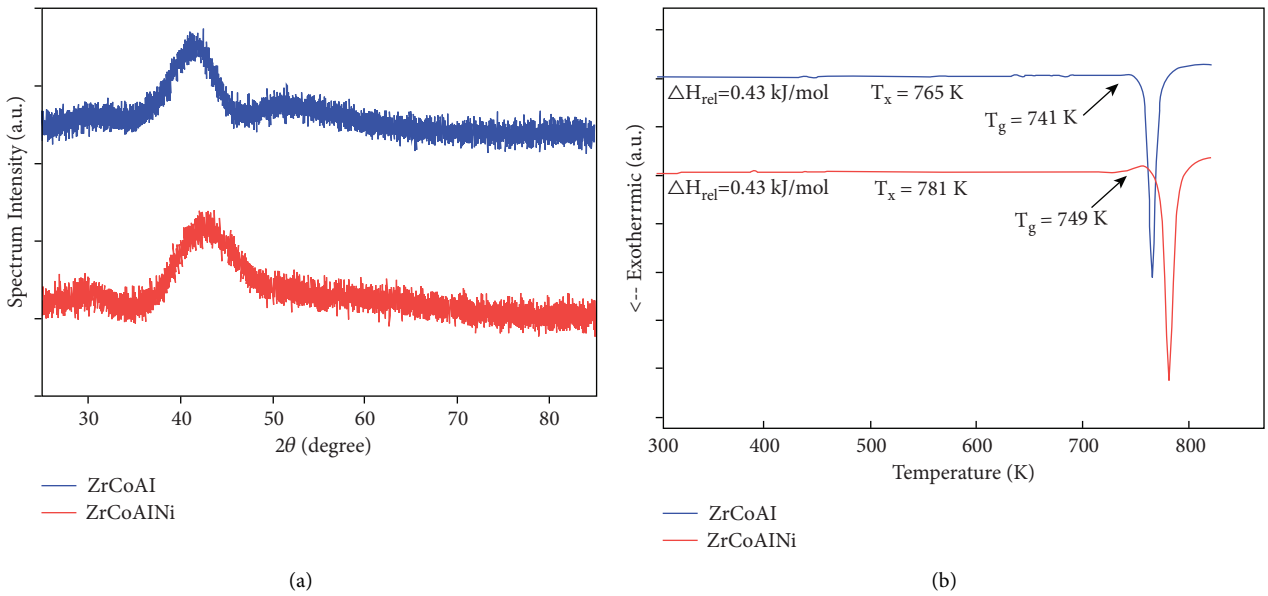

Figure 1: (a) XRD spectra and (b) DSC curves for ZrCoAl and ZrCoAlNi.

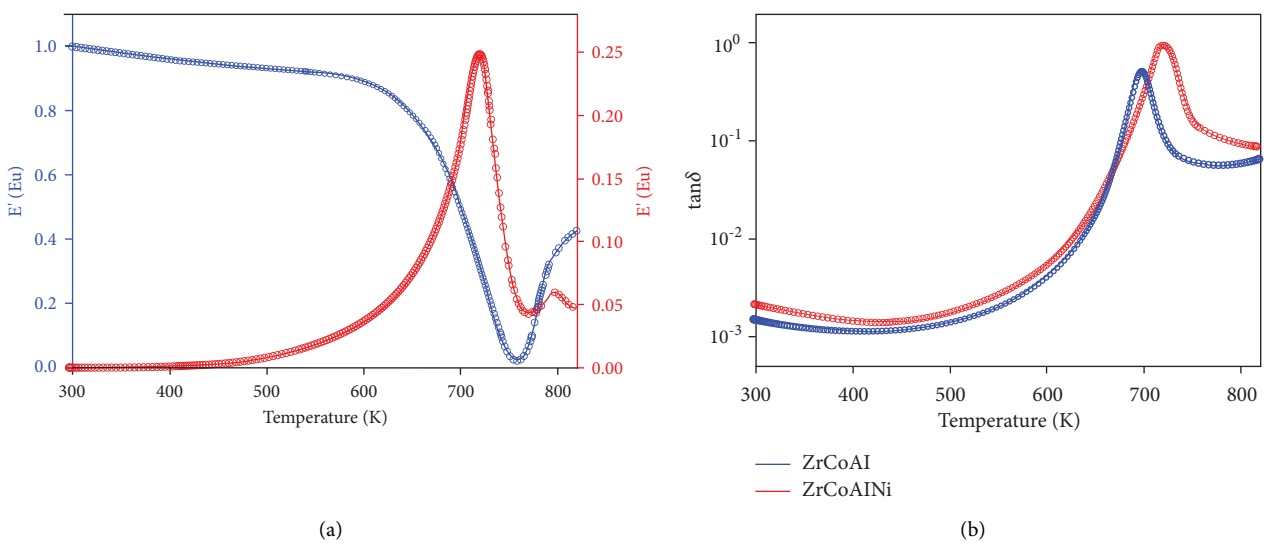

Figure 2: (a) Normalized E'' and E' values for the ZrCoAl sample. (b) Loss factor as a function of temperature for ZrCoAl and ZrCoAlNi.

temperatures for both samples; however, it is more pronounced in the ZrCoAlNi alloy. Using equation (1), it is feasible to calculate the activation energy of α relaxation [25]:

$$f = f_0 \exp\left(-\frac{E_a}{k_B}T\right), \tag{1}$$

in which the driving force and preexponential factor are introduced by f and f_0, respectively. Moreover, K_B and E_α define Boltzmann's constant and the activation energy of main relaxation in the system. As plotted in the insets, the fitted line of logarithm of frequency as a function of reciprocal of peak temperature represents the estimated value of activation energy for the BMGs. The estimations showed that the E_α value was 5.951 eV and 6.205 eV for ZrCoAl and ZrCoAlNi, respectively.

The physical aging below the glass transition temperature was also conducted to characterize the thermal features of samples. Figure 4 illustrates the normalized E' as a function of aging time under the driving frequency of 1 Hz for ZrCoAlNi BMG. Using equation (2), it is possible to describe the evolution of storage modulus in the system [32]:

$$\frac{E'(t)}{E_u} = \frac{A}{1+c}, \qquad c = \left(\frac{\tau_a}{\tau_b + t}\right)^{\beta_C}, \tag{2}$$

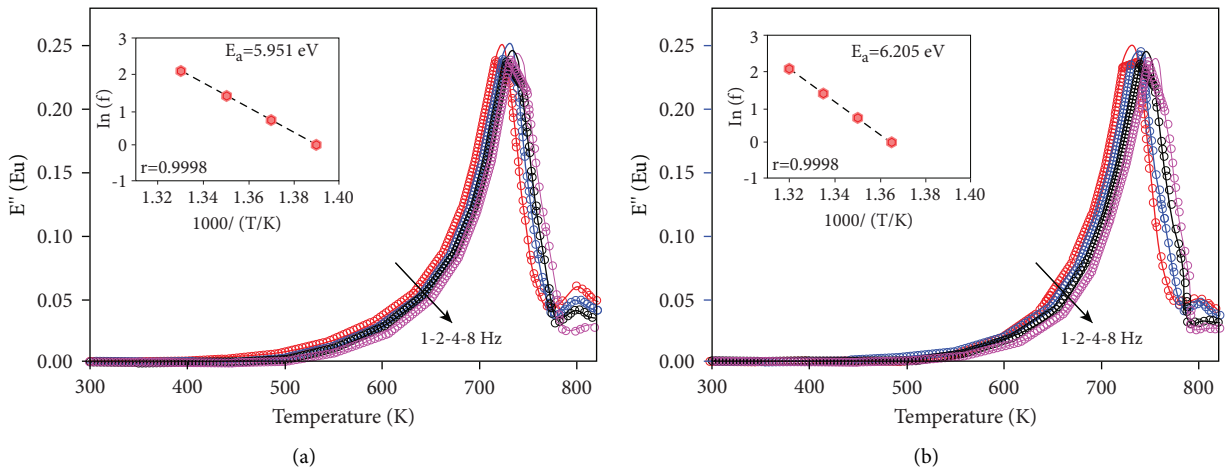

Figure 3: Temperature dependence of normalized loss modulus for different frequencies in (a) ZrCoAl and (b) ZrCoAlNi. The inset shows the estimation of activation energy by fitting driving frequency and temperature.

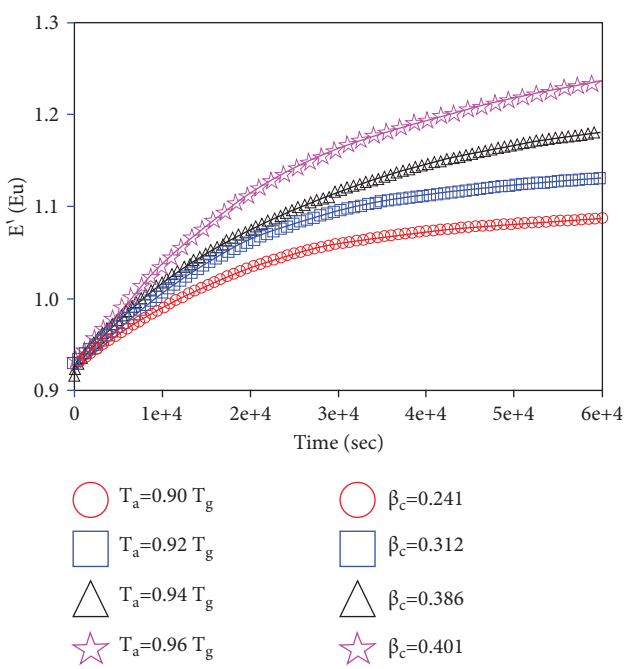

Figure 4: Normalized E' as a function of aging time under the driving frequency of 1 Hz for ZrCoAlNi BMG.

in which τ_a and τ_b are constants at the certain temperature and β_c is correlated to the rate of flow-unit annihilation in the aging process. The parameter "A" also introduces the normalized storage modulus in an infinite aging time. The results indicated that the β_c value is 0.241, 0.312, 0.386, and 0.401 at the annealing temperature of $0.90T_g$ $0.92T_g$, $0.94T_g$, and $0.96T_g$, respectively. Hence, it is concluded that the rise in annealing temperature accelerates the rate of flow-unit annihilation in the structure. Moreover, it is suggested that the sub-Tg annealing treatment stabilizes the amorphous structure at the lower energy levels without formation of any crystals in the material [33]. The Kohlrausch–Williams–Watts (KWW) function was applied to define the internal friction of BMGs [34]:

$$\tan\delta(t_a) - \tan\delta(t_a = 0) = A\left\{1 - \exp\left[-\left(\frac{t_a}{\tau}\right)^{\beta_{\text{aging}}}\right]\right\}, \quad (3)$$

where t_a introduces the aging time and β_{aging} is the KWW exponent describing the level of dynamic heterogeneity. β_{aging} parameter is in the range of 0-1, and it shows the intensified dynamic heterogeneity when it is in the minimum value [34]. The trends of tanδ as a function of annealing time with the driving force of 1 KHz for both samples are given in Figure 5. For ZrCoAlNi sample, β_{aging} declines with the rise of annealing temperature. On the other hand, ZrCoAl shows β_{aging} decreasing trend above the annealing temperature of $0.92T_g$. This means that both samples include a high dynamic heterogeneity at higher annealing temperatures. According to the previous works, β_{aging} dependency on the annealing temperature is different in the amorphous alloys [35, 36]. In addition to the chemical composition, it is strongly suggested that the initial energy state of alloys plays a crucial role in the improvement of dynamic heterogeneity at higher annealing temperatures [9]. In this work, it is also found that the minor Ni addition enhances the intensification of dynamic heterogeneity at high annealing temperature. As indicated in Figure 4, the initial state of storage modulus is in the same value for different annealing temperatures; however, it shows a temperature dependency with the increase of aging time. Moreover, the storage modulus is stabilized when the aging time exceeds from a certain value. On the other hand, Figure 5 indicates that the loss factor exhibited a decreasing trend with the rise of aging time. According to previous studies, the distribution of loosely and densely packed regions in the structure of amorphous alloys is responsible for the dynamic heterogeneity [37]. The loosely packed regions are also identified as the free volumes frozen under the quenching treatment [38]. These regions are potential sites for the generation of plastic deformation and can change the relaxation behavior of amorphous alloys [39]. The free volume also plays a significant role in the atomic mobility, elastic moduli, and mechanical properties of MGs [40].

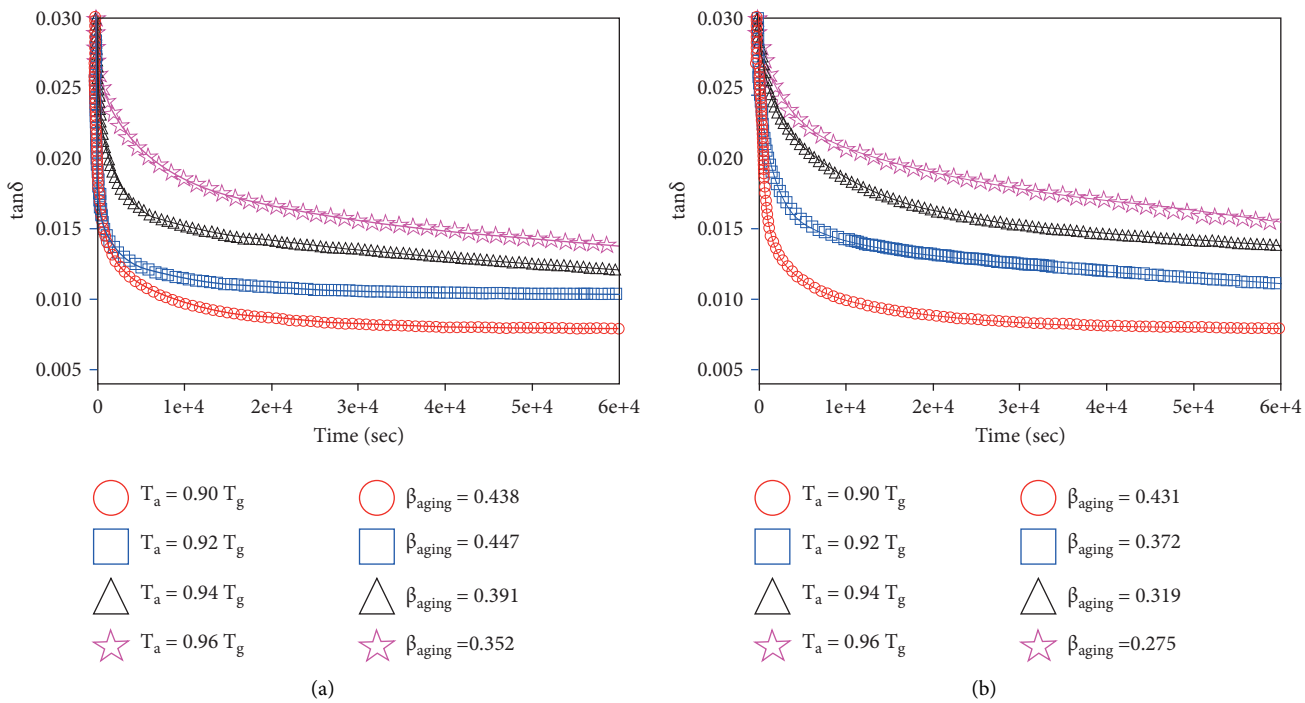

Figure 5: Loss factor as a function of aging time for (a) ZrCoAl and (b) ZrCoAlNi.

Based on Figures 4 and 5, the trends of loss factor and storage modulus of samples imply that the atomic mobility decreases at higher temperatures. Moreover, it is believed that with the increase of aging time, the free volumes are annihilated and the densely packed regions are prevailed in the system, leading to structural relaxation and increment of storage modulus; however, the material reaches an equilibrium state at long aging time, meaning that the rates of free volume annihilation and creation become identical.

The BMG samples were also evaluated through the isothermal frequency scanning method. Figures 6(a) and 6(b) illustrate the trend of normalized storage and loss moduli of ZrCoAlNi as a function of applied frequency. The results demonstrated that the decline of storage modulus is consistent with the decrease of frequency and increase of temperature, respectively. On the other hand, a peak is detected in the curves of loss modulus, shifting to the higher frequencies with the rise of temperature. It is believed that the peak is associated to α relaxation. An empirical function was also proposed by Williams and Watts [41] to characterize α relaxation in the amorphous systems:

$$E'(\omega) = \Delta E_a L_{i\omega}\left[-\frac{d\varphi_a(t,\tau_a)}{dt}\right]\varphi_a(t,\tau_a) = \exp\left[-\left(\frac{t}{\tau_a}\right)^{\beta_{KWW}}\right], \tag{4}$$

in which $L_{i\omega}$ and τ_α are Laplace transform and the primary relaxation time, respectively. ΔE_α introduces the relaxation strength and $\varphi\alpha$ $(t,\ \tau\alpha)$ is the empirical dielectric decay function. Moreover, another relaxation equation with few fitting parameters was proposed by Bergman [42]:

$$E''(\omega) = \frac{E_P}{\left\{1-\beta_{KWW}+\left(\beta_{KWW}/1+\beta_{KWW}\right)\left[\beta_{KWW}\left(\omega_P/\omega\right)+\left(\omega/\omega_P\right)^{\beta_{KWW}}\right]\right\}}, \tag{5}$$

where E_p and ω_p are normalized loss modulus and frequency at the potential peak (see Figure 7). As previously described, β_{KWW} is indicative of dynamic heterogeneity in the system so that with the increase of the exponent value from 0 to 1, the dynamic heterogeneity pales into insignificance in the microstructure. According to Figure 7, β_{KWW} values of the master curves for ZrCoAl and ZrCoAlNi are 0.502 and 0.493, respectively, showing the effects of Ni addition on the improvement of dynamic heterogeneity in the BMG. The figure also confirms that the experimental data are fitted by equation (5) at the peaks; however, there exist some deviations in the high-frequency part of the curves. Figure 7 also shows that the exponent is in the range of 0.5, as also reported in other works related to glassy alloys [43]. For

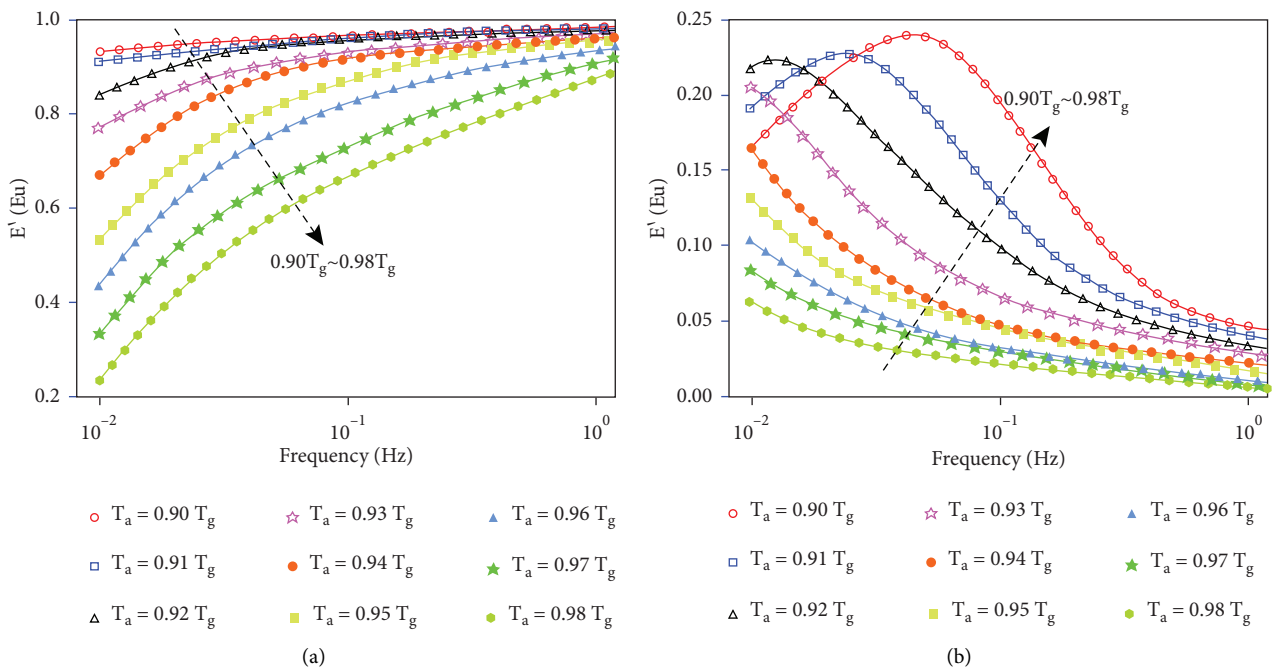

Figure 6: The trend of normalized (a) storage modulus and (b) loss modulus of ZrCoAlNi as a function of applied frequency.

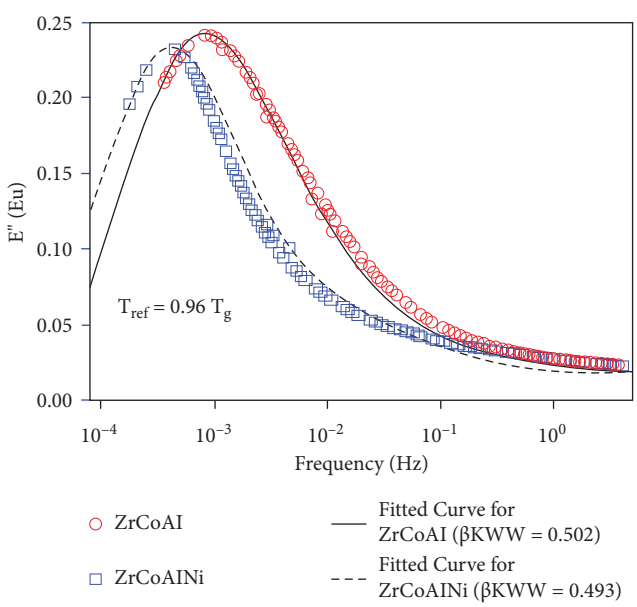

Figure 7: Master curves of ZrCoAl and ZrCoAlNi MGs fitted by the Bergman equation.

evaluation of dynamic mechanical behavior of MGs, it is also possible to apply the theory of quasi-point defects (QPDs) [44]. In this theory, the defect concentration of glassy structure is quantified and correlated to the normalized loss modulus:

$$E''(\omega) = \frac{E_u}{\left[1 + \lambda (i\omega\tau)^{-\chi} + (i\omega\tau)^{-1}\right]}. \quad (6)$$

By fitting the loss modulus-frequency curve, it is possible to obtain correlation factor (χ), numerical factor (λ), and global characteristics time (τ) for the samples. The correlation factor (χ) is indicative of concentration of quasi-point defects in the system and it stands between 0 and 1. At $\chi = 1$, the material shows the state of an ideal gas, while a perfect crystal has a minimum correlation factor ($\chi = 0$). Figure 8 shows the fitted data of loss modulus-frequency based on the QPD model. According to the results, the correlation factor is 0.417 and 0.431 for ZrCoAl and ZrCoAlNi samples, respectively. This means that the Ni addition may increase the defect concentration and lead to the rise of loss modulus in the glassy alloy, which is consistent with the data fitted by the Bergman equation (see Figure 7). In general, it is believed that the increase in dynamic heterogeneity is accompanied with the generation and distribution of loosely packed structure and intensifies the structural defects in the system. However, one should note that the rate of dynamic heterogeneity improvement and defect generation is not similar. As can be seen in Figure 9, the relative variation of β_{KWW} is sharper than χ parameter with the increase of temperature. This implies that it is possible to improve the dynamic heterogeneity through a small introduction of defects, i.e., free volumes, into the system. As a topological point of view, it was found that the Ni addition into the ZrCoAl MGs leads to the rise in types of atomic clusters, i.e., short range orders, stabilizing the liquid and glass formation [26]. However, one should note that the increase of cluster types is a main reason for generation of nanoscale defects in the structure, leading to the improvement of heterogeneity. This event was also reported in other works. For instance, the minor addition of Ni and Co in the LaGa-based MGs leads to the shift of relaxation peak to higher temperatures, while the

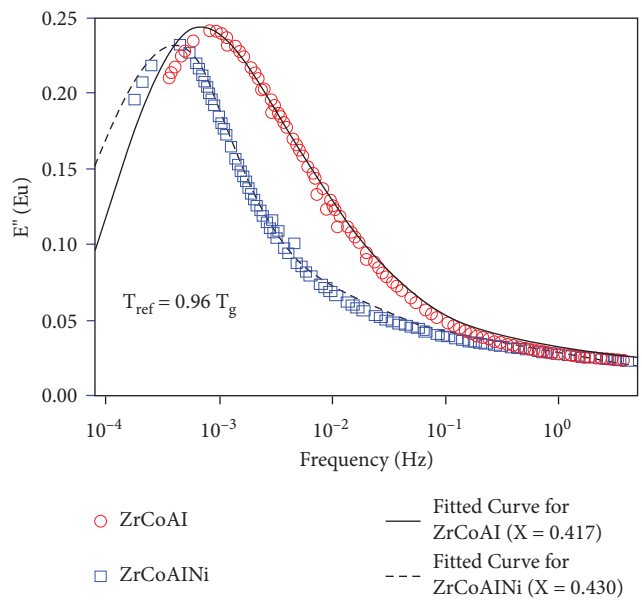

Figure 8: Master curves of ZrCoAl and ZrCoAlNi MGs fitted by the QPD equation.

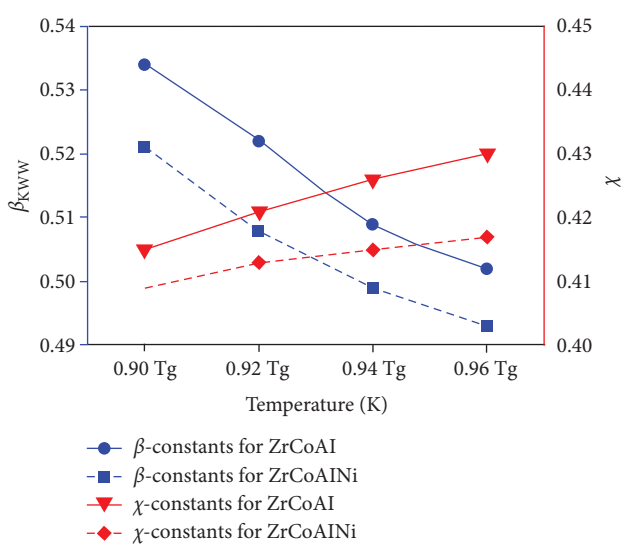

Figure 9: Variations of β_{KWW} and χ parameters as a function of temperature.

peak becomes more pronounced [45]. It was also reported that the minor Gd addition in the CuZr-based MG intensifies the boson peaks in the thermographs and improves the structural heterogeneity [46].

4. Conclusions

In this study, the mechanical relaxation behaviors of BMGs with alloying compositions of ZrCoAl and ZrCoAlNi were investigated in detail. The main outcomes are as follows:

(i) The minor Ni addition not only improved the thermal stability but also enhanced the enthalpy of relaxation. Moreover, it was found that the relaxation event was retarded in the Ni-added sample.

(ii) The DMA results indicated that the Ni addition generated the loosely packed structure and enhanced the dynamic heterogeneity in the amorphous alloy.

(iii) The fitted data of loss modulus-frequency based on the QPD model show that the correlation factor is 0.417 and 0.431 for ZrCoAl and ZrCoAlNi samples, respectively. This means that the Ni addition may increase the defect concentration and lead to the rise of loss modulus in the glassy alloy, which is consistent with that resulting from the KWW model.

Data Availability

The data used to support the findings of this study are included within the article.

Conflicts of Interest

The authors declare that they have no conflicts of interest.

References

[1] M. Li, H. Guan, S. Yang, X. Ma, and Q. Li, "Minor Cr alloyed Fe–Co–Ni–P–B high entropy bulk metallic glass with excellent mechanical properties," *Mater. Sci. Eng*, vol. 805, 2020.

[2] Z. Li, M. Zhang, J. Wang, N. Li, and L. Liu, "Pronounced softening of a Zr-based metallic glass in micro annular gap flow," *Materials Research Letters*, vol. 10, no. 2, pp. 62–69, 2022.

[3] M. Shi, J. Chen, and C. Chen, "Inverse size effects in unnotched and notched metallic glass thin films," *Journal of Non-crystalline Solids*, vol. 575, Article ID 121172, 2022.

[4] P. Sonia and S. Kumari, "Performance evaluation of multi-fibre (hybrid) polymer composite," *IOP Conference Series: Materials Science and Engineering*, vol. 1116, no. 1, Article ID 012027, 2021.

[5] L. T. Zhang, Y. J. Wang, E. Pineda, H. Kato, Y. Yang, and J. C. Qiao, "Sluggish dynamics of homogeneous flow in high-entropy metallic glasses," *Scripta Materialia*, vol. 214, Article ID 114673, 2022.

[6] S. Zhang, W. Wang, and P. Guan, "Dynamic crossover in metallic glass nanoparticles," *Chinese Physics Letters*, vol. 38, no. 1, Article ID 016802, 2021.

[7] D. Bandhu, J. J. Vora, S. Das et al., "Experimental study on application of gas metal arc welding based regulated metal deposition technique for low alloy steel," *Materials and Manufacturing Processes*, pp. 1–19, 2022.

[8] S. Kumari, B. Nakum, D. Bandhu, and K. Abhishek, "Multi-attribute group decision making (MAGDM) using fuzzy linguistic modeling integrated with the VIKOR method for car purchasing model," *International Journal of Decision Support System Technology*, vol. 14, pp. 1–20, 2022.

[9] W. H. Wang, "Dynamic relaxations and relaxation-property relationships in metallic glasses," *Progress in Materials Science*, vol. 106, Article ID 100561, 2019.

[10] Q. Hao, W. Y. Jia, and J. C. Qiao, "Dynamic mechanical relaxation in Zr65Ni7Cu18Al10 metallic glass," *Journal of Non-crystalline Solids*, vol. 546, Article ID 120266, 2020.

[11] G. J. Lyu, J. C. Qiao, J.-M. Pelletier, and Y. Yao, "The dynamic mechanical characteristics of Zr-based bulk metallic glasses and composites," *Materials Science and Engineering A*, vol. 711, pp. 356–363, 2018.

[12] D. R. Tripathi, K. H. Vachhani, D. Bandhu, S. Kumari, V. R. Kumar, and K. Abhishek, "Experimental investigation and optimization of abrasive waterjet machining parameters for GFRP composites using metaphor-less algorithms," *Materials and Manufacturing Processes*, vol. 36, no. 7, pp. 803–813, 2021.

[13] L. Zhang, Y. Duan, D. Crespo et al., "Dynamic mechanical relaxation and thermal creep of high-entropy La30Ce30-Ni10Al20Co10 bulk metallic glass," *Science China Physics, Mechanics & Astronomy*, vol. 64, no. 9, Article ID 296111, 2021.

[14] M. Liu, J. Qiao, Q. Hao et al., "Dynamic mechanical relaxation in LaCe-based metallic glasses: Influence of the chemical composition," *Metals*, vol. 9, p. 1013, 2019.

[15] K. Tao, J. C. Qiao, Q. F. He, K. K. Song, and Y. Yang, "Revealing the structural heterogeneity of metallic glass: mechanical spectroscopy and nanoindentation experiments," *International Journal of Mechanical Sciences*, vol. 201, Article ID 106469, 2021.

[16] A. Das, E. M. Dufresne, and R. Maaß, "Structural dynamics and rejuvenation during cryogenic cycling in a Zr-based metallic glass," *Acta Materialia*, vol. 196, pp. 723–732, 2020.

[17] T. Pérez-Castañeda, C. Rodríguez-Tinoco, J. Rodríguez-Viejo, and M. A. Ramos, "Suppression of tunneling two-level systems in ultrastable glasses of indomethacin," *Proceedings of the National Academy of Sciences*, vol. 111, no. 31, pp. 11275–11280, 2014.

[18] J. C. Qiao, Y. Yao, J. M. Pelletier, and L. M. Keer, "Understanding of micro-alloying on plasticity in Cu46Zr47−xAl7Dyx (0≤ x ≤ 8) bulk metallic glasses under compression: based on mechanical relaxations and theoretical analysis," *International Journal of Plasticity*, vol. 82, pp. 62–75, 2016.

[19] G. R. Garrett, M. D. Demetriou, J. Chen, and W. L. Johnson, "Effect of microalloying on the toughness of metallic glasses," *Applied Physics Letters*, vol. 101, no. 24, Article ID 241913, 2012.

[20] K. Tao, J. C. Qiao, L. Zhang, and J. M. Pelletier, "Dynamic mechanical response of ZrCu-based bulk metallic glasses," *International Journal of Mechanical Sciences*, vol. 211, Article ID 106770, 2021.

[21] I. Raya, T.-C. Chen, S. H. Pranoto et al., "Role of Si minor addition on glass formation and flow stress characteristics of a Zr-based metallic glass," *Materials Research*, vol. 24, no. 6, 2021.

[22] L. Xu, Q. Lu, and Q. Zhang, "Effects of refractory Nb on glass-forming ability and structure inhomogeneity of Cu50Zr50 binary metallic glass," *Materials Research Express*, vol. 6, no. 9, Article ID 095203, 2019.

[23] J. C. Qiao, J. Cong, Q. Wang, J. M. Pelletier, and Y. Yao, "Effects of iron addition on the dynamic mechanical relaxation of Zr55Cu30Ni5Al10 bulk metallic glasses," *Journal of Alloys and Compounds*, vol. 749, pp. 262–267, 2018.

[24] D. Li, C. Jiang, H. Li, and M. Pandey, "Crystallization evolution and relaxation behavior of high entropy bulk metallic glasses using microalloying process," *Chinese Physics B*, vol. 30, no. 6, Article ID 066401, 2021.

[25] Y. T. Cheng, Q. Hao, J. C. Qiao, D. Crespo, E. Pineda, and J. M. Pelletier, "Effect of minor addition on dynamic mechanical relaxation in ZrCu-based metallic glasses," *Journal of Non-crystalline Solids*, vol. 553, Article ID 120496, 2021.

[26] M. Samavatian, R. Gholamipour, and V. Samavatian, "Discovery of novel quaternary bulk metallic glasses using a developed correlation-based neural network approach," *Computational Materials Science*, vol. 186, Article ID 110025, 2021.

[27] Q. Wang, S. T. Zhang, Y. Yang, Y. D. Dong, C. T. Liu, and J. Lu, "Unusual fast secondary relaxation in metallic glass," *Nature Communications*, vol. 6, no. 1, p. 7876, 2015.

[28] J. D. Ju and M. Atzmon, "A comprehensive atomistic analysis of the experimental dynamic-mechanical response of a metallic glass," *Acta Materialia*, vol. 74, pp. 183–188, 2014.

[29] L. T. Zhang, Y. J. Duan, T. Wada et al., "Dynamic mechanical relaxation behavior of Zr35Hf17. 5Ti5. 5Al12. 5Co7. 5Ni12Cu10 high entropy bulk metallic glass," *Journal of Materials Science & Technology*, vol. 83, pp. 248–255, 2021.

[30] X. Cui, J. Guo, J. c Qiao et al., "Influence of the chemical composition on the β-relaxation and the mechanical behavior of LaCe-based bulk metallic glasses," *Journal of Non-crystalline Solids*, vol. 562, Article ID 120779, 2021.

[31] S. H. Xie, X. R. Zeng, and H. X. Qian, "Correlations between the relaxed excess free volume and the plasticity in Zr-based bulk metallic glasses," *Journal of Alloys and Compounds*, vol. 480, no. 2, pp. L37–L40, 2009.

[32] D. P. Wang, Z. G. Zhu, R. J. Xue, D. W. Ding, H. Y. Bai, and W. H. Wang, "Structural perspectives on the elastic and mechanical properties of metallic glasses," *Journal of Applied Physics*, vol. 114, no. 17, Article ID 173505, 2013.

[33] J. W. Lv, D. W. Yin, F. L. Wang, Y. J. Yang, M. Z. Ma, and X. Y. Zhang, "Influence of sub-Tg annealing on microstructure and crystallization behavior of TiZr-based bulk metallic glass," *Journal of Non-crystalline Solids*, vol. 565, Article ID 120855, 2021.

[34] J. C. Qiao and J. M. Pelletier, "Dynamic mechanical relaxation in bulk metallic glasses: a review," *Journal of Materials Science & Technology*, vol. 30, no. 6, pp. 523–545, 2014.

[35] A. Ishii, "Spatial and temporal heterogeneity of Kohlrausch–Williams–Watts stress relaxations in metallic glasses," *Computational Materials Science*, vol. 198, Article ID 110673, 2021.

[36] W. Zhai, C. H. Wang, J. C. Qiao, J.-M. Pelletier, F. P. Dai, and B. Wei, "Distinctive slow β relaxation and structural heterogeneity in (LaCe)-based metallic glass," *Journal of Alloys and Compounds*, vol. 742, pp. 536–541, 2018.

[37] J.-L. Gu, H.-W. Luan, S.-F. Zhao et al., "Unique energy-storage behavior related to structural heterogeneity in high-entropy metallic glass," *Materials Science and Engineering A*, vol. 786, Article ID 139417, 2020.

[38] F. Zhu, S. Song, K. M. Reddy, A. Hirata, and M. Chen, "Spatial heterogeneity as the structure feature for structure–property relationship of metallic glasses," *Nature Communications*, vol. 9, no. 1, p. 3965, 2018.

[39] C. Ma, S. Suslov, C. Ye, and Y. Dong, "Improving plasticity of metallic glass by electropulsing-assisted surface severe plastic deformation," *Materials & Design*, vol. 165, Article ID 107581, 2019.

[40] W. Guo, R. Yamada, and J. Saida, "Rejuvenation and Plasticization of Metallic Glass by Deep Cryogenic Cycling Treatment," *Intermetallics*, vol. 93, pp. 141–147, 2018.

[41] G. Williams and D. C. Watts, "Non-symmetrical dielectric relaxation behaviour arising from a simple empirical decay function," *Transactions of the Faraday Society*, vol. 66, p. 80, 1970.

[42] R. Bergman, "General susceptibility functions for relaxations in disordered systems," *Journal of Applied Physics*, vol. 88, no. 3, pp. 1356–1365, 2000.

[43] J. C. Qiao and J. M. Pelletier, "Kinetics of structural relaxation in bulk metallic glasses by mechanical spectroscopy:

determination of the stretching parameter βKWW," *Intermetallics*, vol. 28, pp. 40–44, 2012.

[44] J. C. Qiao, Y. X. Chen, J.-M. Pelletier et al., "Viscoelasticity of Cu-and La-based bulk metallic glasses: interpretation based on the quasi-point defects theory," *Materials Science and Engineering A*, vol. 719, pp. 164–170, 2018.

[45] R. J. Xue, L. Z. Zhao, B. Zhang, H. Y. Bai, W. H. Wang, and M. X. Pan, "Role of low melting point element Ga in pronounced β-relaxation behaviors in LaGa-based metallic glasses," *Applied Physics Letters*, vol. 107, no. 24, Article ID 241902, 2015.

[46] Y. Li, H. Y. Bai, W. H. Wang, and K. Samwer, "Low-temperature specific-heat anomalies associated with the boson peak in CuZr-based bulk metallic glasses," *Physical Review B: Condensed Matter*, vol. 74, no. 5, Article ID 052201, 2006.

Hindawi
Advances in Materials Science and Engineering
Volume 2022, Article ID 6528470, 8 pages
https://doi.org/10.1155/2022/6528470

Research Article

The Effects of Minor Element Addition on the Structural Heterogeneity and Mechanical Properties of ZrCuAl Bulk Metallic Glasses

R. Sivaraman,[1] Indrajit Patra,[2] Zainab Mohsen Najm,[3] Noora M. Hameed,[4] Taif Alawsi,[5] and Seyedmasoud Hashemi[6]

[1]*Department of Mathematics, Dwaraka Doss Goverdhan Doss Vaishnav College, University of Madras, Chennai, India*
[2]*Ph.D from NIT Durgapur, West Bengal, India*
[3]*Anesthesia Techniques Department, Al-Mustaqbal University College, Babylon, Iraq*
[4]*Anesthesia Techniques Department, Al-Nisour University College, Baghdad, Iraq*
[5]*Scientific Research Center, Al-Ayen University, Thi-Qar, Iraq*
[6]*Department of Chemistry, Iran University of Science & Technology (IUST), Tehran, Iran*

Correspondence should be addressed to Seyedmasoud Hashemi; smhashemi33@gmail.com

Received 19 June 2022; Revised 15 July 2022; Accepted 27 July 2022; Published 27 August 2022

Academic Editor: Majid Samavatian

Copyright © 2022 R. Sivaraman et al. This is an open access article distributed under the Creative Commons Attribution License, which permits unrestricted use, distribution, and reproduction in any medium, provided the original work is properly cited.

The present study reveals the role of Nb and Ni minor addition on the nanomechanical properties and nanostructure of ZrCuAl bulk metallic glass (BMG). For this purpose, atomic force microscopy (AFM) was used to evaluate the viscoelastic response of the BMG surface at the nanoscale, while the nanoindentation technique was applied to show the mechanism of plastic deformation. The results indicated that minor Nb addition decreased the relaxation of enthalpy accompanied by the weakening of structural heterogeneity. On the other hand, Ni addition improved the stored energy of the material and intensified the distribution of loosely packed regions in the microstructure. Moreover, the mechanical test unveiled that Ni addition enhanced the viscoelastic response; however, it came at the expense of creep resistance. The evaluation of the magnitude of the derivative in the nanoindentation test also demonstrated that the Ni-added sample exhibited a multiple shear-band mode for plastic deformation.

1. Introduction

Due to their amorphous structure, bulk metallic glasses (BMGs) possess excellent properties such as good corrosion resistance, superior strength, and sound magnetic features [1–5]. However, the inhomogeneous plastic deformation under the external loadings limits their applications in the industries [6, 7]. In recent years, minor element addition has been one of the main methods for improving the homogenous plastic deformation and strength in the BMGs [8–10]. The intensification of structural heterogeneity in the amorphous alloy determines the level of homogenous plasticity. The heterogeneity in the glassy structure has originated from the random scatter of loosely packed region free volumes in a rigid backbone with short and medium orders [11]. Considering the microalloying process, Zhu et al. [12] indicated that Sc addition into ZrCuNiAlTi BMG improved spatial heterogeneity and plastic deformation, which was due to the large atomic radius of Sc and the significant atomic size mismatch in the structure. Liang et al. [13] reported that an appropriate substitution of Fe by W enhanced both plastic deformation and ultimate compressive strength in the FeCrMoWCBY BMG. Teng et al. [14] revealed that the hydrogen microalloying process induced more liquid-like regions and abundant flow units, triggering the shear events and homogenous plastic deformation. It was also found that the hydrogen microalloying activated soft spots and improved structural heterogeneity, leading to the promotion of multiple shear bands [15]. Jin et al. [16] demonstrated that partial substitution of Hf with Cu

enhanced the compressive yield strength with a large plastic strain. Cao et al. [17] reported that minor element addition with positive heat of mixing into a ZrCuAl amorphous alloy not only improved the glass formation but also induced homogenous plastic deformation. Based on their results, the elements with smaller positive heat of mixing were more efficient in the improvement of glass formation owing to liquid stabilization, while elements with medium positive heat of mixing enhanced plastic deformation through the intensification of structural heterogeneity.

As aforementioned, proper minor addition may improve the structural heterogeneity and homogenous plastic deformation in the BMGs. Nevertheless, it is required to identify the microalloying effect on the structural heterogeneity with the high-resolution instruments. In recent years, atomic force microscopy (AFM) has been offered for this purpose [18–20]. For example, Mahmoud et al. [21] applied dynamic AFM to characterize the relaxation of nanoscale regions in a shock-peened BMG. Using high-resolution AFM, it was found that chemical variations changed the structural heterogeneity in the amorphous alloys [22]. Samavatian et al. [23] indicated that the low-dissipated regions resisted the energy alterations under repetitive AFM scanning, while high-dissipated regions exhibited a stochastic behavior. Using a contact resonance AFM, it was reported that the nanoscale zones with eminent heterogeneity induced a broad energy state distribution in the system [24]. The mentioned works clearly indicate that the AFM is an efficient instrument for the evaluation of nanoscale regions at the surface of BMGs. Hence, we used this method to characterize the nanoscale structural heterogeneity of BMGs under the minor addition. For this purpose, the $Zr_{57}Cu_{32}Al_{10}$ BMG was selected as the base alloy, while Ni and Nb elements were applied as the dopants. It is believed that the differences in the atomic size and thermodynamic behaviors of Ni and Nb significantly change the thermal behavior, microstructure, and mechanical properties in the ZrCuAl alloy. Hence, it is expected that the results shed light on the relation between the structural evolution, plastic deformation, and strength in this alloy.

2. Materials and Methods

For materials preparation, ingots with the alloying compositions of $Zr_{57}Cu_{32}Al_{10}$, $(Zr_{57}Cu_{32}Al_{10})_{97}Ni_3$, and $(Zr_{57}Cu_{32}Al_{10})_{97}Nb_3$ were fabricated through the arc melting of elements with >99.8% purity. Afterwards, the water-cooled copper mold casting was applied to produce BMG plates with dimensions of $10\,mm \times 10\,mm \times 3\,mm$. The differential scanning calorimetry (DSC) and X-ray diffraction (XRD) tests were also carried out to characterize the thermal features and amorphousness of BMG plates.

To study the structural heterogeneity, high-resolution atomic force microscopy (AFM) was applied in the tapping mode. In this experiment, the samples were cut from the plates and polished to obtain a uniform surface. A sharp probe with a tip diameter of $\sim 2\,nm$ facilitates the high-resolution scanning of samples. The energy dissipation of surfaces was calculated from the phase shift measurement [21]. To attain reliable results, AFM scanning was conducted in different windows on the sample surfaces. Considering (1), the energy dissipation of the surface can be calculated in accordance with the phase shift measurements [25]:

$$E_{\mathrm{dis}} = \left[\frac{\pi.K.A_{sp}.A_0.(\sin(\pi/2-\varphi))}{Q}\right] - \frac{A_{sp}}{A_0}. \quad (1)$$

In this equation, Q and K are the damping factor and the spring constant. The phase shift is defined by φ, while the set-point amplitude and free amplitude are shown by A_{sp} and A_0, respectively. The details for the calculation of energy dissipation are given in [25, 26]. The nanomechanical properties of BMG samples were also evaluated by the nanoindentation test. The experiment was conducted at room temperature under loading rates of $1\,\mathrm{mNs}^{-1}$. The holding time at maximum load was 10 s, whereas the maximum load was 25 mN. Thermal drift correction was also performed to remove drift effects and obtain accurate results with minimum fluctuations. To make the statistical evaluation possible, 80 indenting points were tested for each sample. Moreover, the magnitude of the derivative ($dh/dp^{0.5}$) was calculated for each state. In general, this term indicates the variations of pop-ins concerning the indenting load.

3. Results and Discussion

The XRD patterns of specimens are illustrated in Figure 1(a). The results indicated that there existed no sign of sharp Bragg peaks in the XRD patterns, meaning the absence of long-range orders in the atomic structure of samples. Figure 1(b) represents the thermal history of samples in the relaxation region. As observed, the enthalpy of relaxation is 7.7 J/g, 8.1 J/g, and 6.9 J/g in the ZrCuAl, ZrCuAlNi, and ZrCuAlNb samples, respectively. This outcome implies that Ni addition increases the stored energy in the system, leading to the intensification of structural heterogeneity, while Nb addition creates a relaxed structure with a more stable atomic configuration.

To characterize the structural heterogeneity, it is required to measure the distribution of energy dissipation in the amorphous alloys. One should note that the tapping load of the AFM tip is restricted so that no plastic deformation occurs on the surfaces. Hence, the energy dissipation of the surface is just a result of the viscoelastic response of the amorphous structure to the external excitation (tip tapping) [27]. Figure 2 shows the linear scanning of phase shift and topography analysis in the same position for the ZrCuAl sample. As can be seen, the phase shift and the height variation exhibit a different trend, meaning that there is no strong correlation between the phase lag and the roughness of the sample. Moreover, the height fluctuation at the surface is in the range of 0.2–0.75 nm, which indicates that careful polishing leads to a smooth surface. Figure 3 gives the 2D maps of energy dissipation for all the samples. As demonstrated, the high-dissipated-energy regions are embedded in a backbone with low dissipated energy. Generally, structural defects such as free volumes are the regions that dissipated

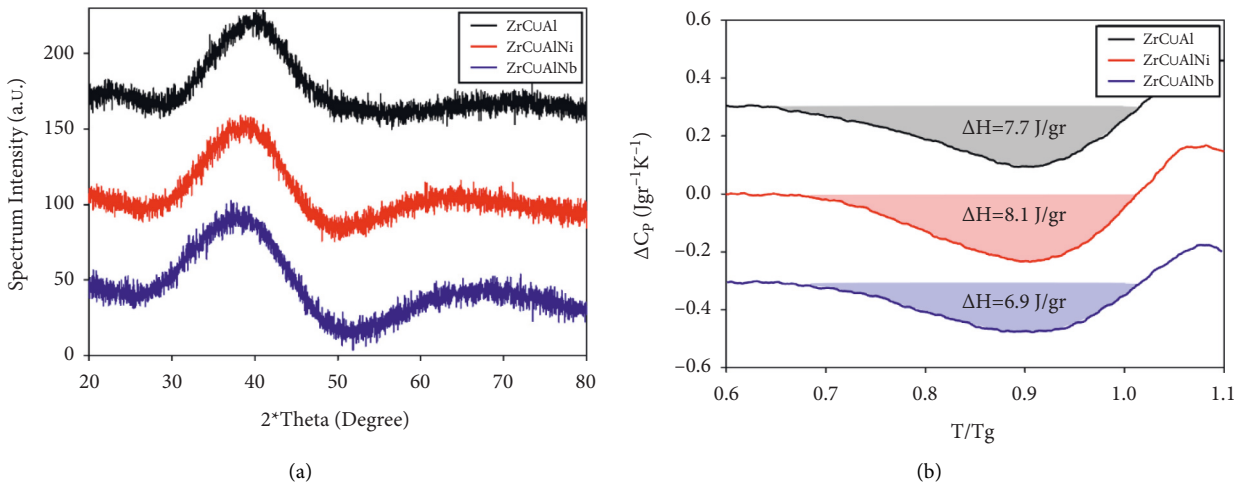

Figure 1: (a) XRD patterns and (b) DSC curves at the relaxation region for all the samples.

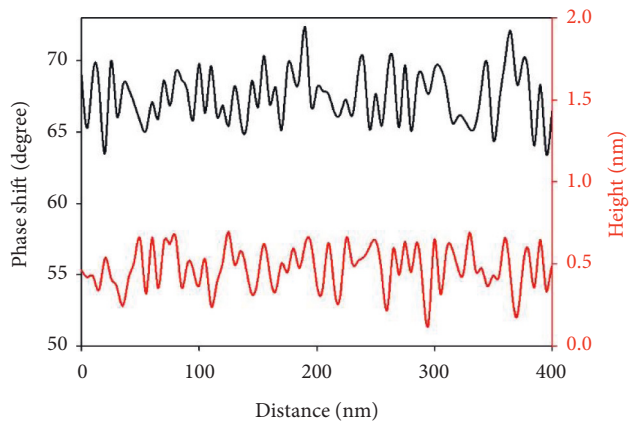

Figure 2: Linear scanning of phase shift and topography in the same position for ZrCuAl.

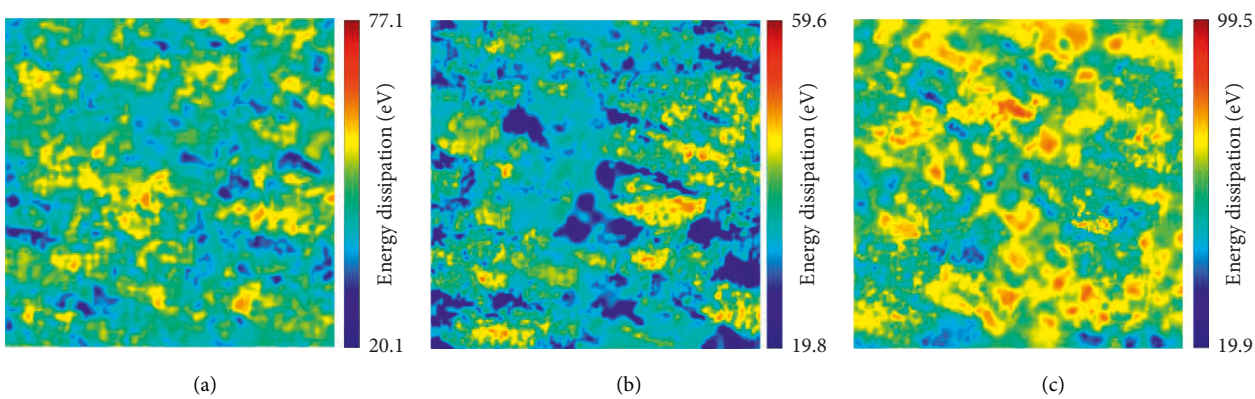

Figure 3: 2D maps of energy dissipation with a scanning size of 400×400 nm^2 for (a) ZrCuAl, (b) ZrCuAlNb, and (c) ZrCuAlNi.

energy significantly, while the short-range and medium-range orders are densely packed structures with low dissipated energy [18]. This event is due to the fact that the free volumes exhibit a viscoelastic response under tip tapping, leading to a huge energy release, while the dense regions show a rigid reaction such as crystalline alloys [28]. This description clearly indicates that why the metallic glasses have heterogeneous structures at the nanoscale. However, the results revealed that the intensification of heterogeneity is different in each sample. For the ZrCuAl alloy, the energy dissipation is in the range of 20.1–77.1 eV. On the other hand, ZrCuAlNi exhibits an energy dissipation range of

19.8–99.5 eV, showing the intensification of structural heterogeneity, whereas, the Nb-added sample shows a weak heterogeneity with a narrow range of energy dissipation values of 19.8–59.6 eV. As mentioned in Figure 1, the Nb-added sample included the minimum stored energy which is consistent with the weak structural heterogeneity. On the other hand, the Ni-added sample has a high enthalpy of relaxation, meaning that the system tends to show sharp heterogeneity in its structure. To conduct a detailed study, the FFT analysis of energy dissipation based on a polar presentation is given in Figure 4. According to the results, the data for the ZrCuAl alloy are distributed in an oval shape at the center of the figure. For ZrCuAlNi, the data distribution is more sporadic and has a sharp oval deviated configuration at the center. On the other hand, the collected data for the Nb-added sample are intensified at the center, implying the weak structural heterogeneity in this state. The Gaussian-type distribution of energy dissipation for the samples is represented in Figure 5(a)–5(c). As measured, the mean values of energy for ZrCuAl, ZrCuAlNb, and ZrCuAlNi are 40.2 eV, 48.3 eV, and 51.5 eV, respectively. The results also indicated that the ZrCuAlNb alloy has a sharp energy distribution, whereas the Ni-added sample exhibits a widened distribution which is also shifted to the higher energy values. To quantitatively analyze the structural heterogeneity in the samples, it is possible to determine the correlation function by using the length scale of loosely packed regions (ξ) in the atomic structure [29]:

$$P(r) = 2\sigma^2\left[1 - \exp\left(-\left(\frac{r}{\xi}\right)^{2\alpha}\right)\right], \quad (2)$$

where the α and σ parameters introduce the phase shift exponent and root mean square of phase shift values, respectively. Moreover, the correlation function can be defined through $P(r) = \langle P_1(r) - P(0)\rangle^2$, in which $P_1(r)$ and $P(0)$ are the phase shift values at the coordinate (x, y) and the reference position (0, 0), respectively [29]. Figure 5(d) shows the $P(r)$ curves as a function of distance. Data fitting of $P(r)$ makes possible the extraction of correlation lengths (ξ) for the samples. It is observed that Ni minor addition leads to the increase of correlation length from 6.41 nm (ZrCuAl) to 8.34 nm, while ZrCuAlNb experiences a low ξ value (5.91 nm). This result clarifies that the size of loosely packed regions significantly decreases with the addition of Nb into the base alloy. Other works also confirmed that Nb or Ni addition markedly changes the structural features of ZrCuAl amorphous alloys [30]. Moreover, it is suggested that minor Ni addition enhances the total negative enthalpy of mixing in the material and manifolds the types of short-range order (SRO) clusters but not their populations, leading to an increase of relaxation enthalpy. In this state, the rise in SRO types alters the medium-range orders (MROs) from the interpenetrated arrangements to the loose configurations, which provides potential sites for the nucleation of shear transformation zones (STZs) in the structure. On the other hand, the pair distribution function (PDF) analysis indicates that minor Nb addition leads to the shrinkage of SRO clusters, which is due to the strong interaction of Zr and Nb atoms accompanied by bond shortening in the system [31]. Furthermore, Nb addition densifies the spatial connections in the structure and intensifies the interpenetrated MROs in the ZrCuAlNb alloy. This phenomenon is due to the decrease of Zr-centered and Al-centered clusters that are responsible for the creation of nanoscale loose regions in the ZrCuAl BMG [30]. Hence, it is concluded that Nb addition increases the dense atomic orders and decreases the enthalpy of relaxation and structural heterogeneity in the ZrCuAl BMG.

The load-displacement curves of BMG specimens are represented in Figure 6(a). It is found that Ni addition significantly enhances the displacement (h) of BMG; however, Nb addition leads to the decrease of plastic deformation under the nanoindentation process. Moreover, Ni addition intensifies creep displacement at the maximum load. This means that the Ni-added sample is exposed to higher plastic deformation under constant loading, which is due to the increase of potential sites for the creation and generation of nanoscale shear events during the indenting process. To make a detailed comparison, the maximum indentation depth (d_{max}) and the final indentation depth (d_f) in the curves are evaluated. As given in Figure 6(b), the d_f/d_{max} ratio in the ZrCuAlNi alloy is higher than other samples. High d_f/d_{max} means that the BMG sample stores significant anelastic energy in its microstructure. In general, the creep event in the amorphous alloys includes the viscoelastic and viscoplastic strains. Based on our results, the Ni-added sample shows a great viscoelastic response to external excitation (higher d_f/d_{max}), which is due to the intensified structural heterogeneity; however, this sample experiences a huge viscoplastic strain at the maximum load, showing that it is a sign of severe creep deformation. On the other hand, the Nb-added sample shows a reverse behavior compared to the ZrCuAlNi BMG, which implies that Nb addition improves the creep resistance through the prevention of nanoscale strain localization in its atomic structure. In order to evaluate the variations of strength and mechanical properties, it is necessary to conduct a statistical analysis regarding the hardness and Young's modulus of BMGs. Figure 7 indicates the correlation between the hardness/elastic modulus of samples and the displacement at the maximum load (creep displacement). The results clearly unveil that Ni addition leads to the decrement of hardness and Young's modulus so that the mean values of hardness and Young's modulus for ZrCuAlNi are 13% and 19% lower than the ZrCuAl alloy, respectively. On the other side, the Nb-added sample exhibits higher hardness and Young's modulus values compared to the base alloy. Furthermore, one can see that the distribution of Young's modulus and hardness shows a linear trend with statistical Pearson correlation coefficients of −0.892 and −0.855 and the negative slopes of −2.13 and $-0.94\,\mathrm{nm\,GPa^{-1}}$, respectively. The similarities in the trends of properties indicate that minor addition simultaneously affects Young's modulus and hardness; however, one can see that the elastic modulus is more sensitive to the microalloying process. The results also reveal that the distribution of data in the Ni-added sample is more sporadic compared to the other samples. This outcome

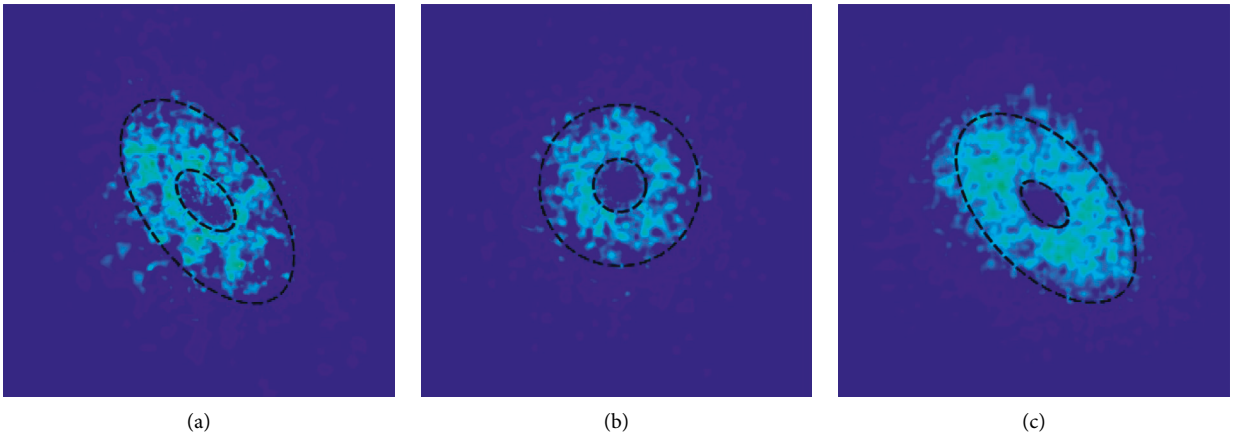

Figure 4: FFT data for energy dissipation in (a) ZrCuAl, (b) ZrCuAlNb, and (c) ZrCuAlNi.

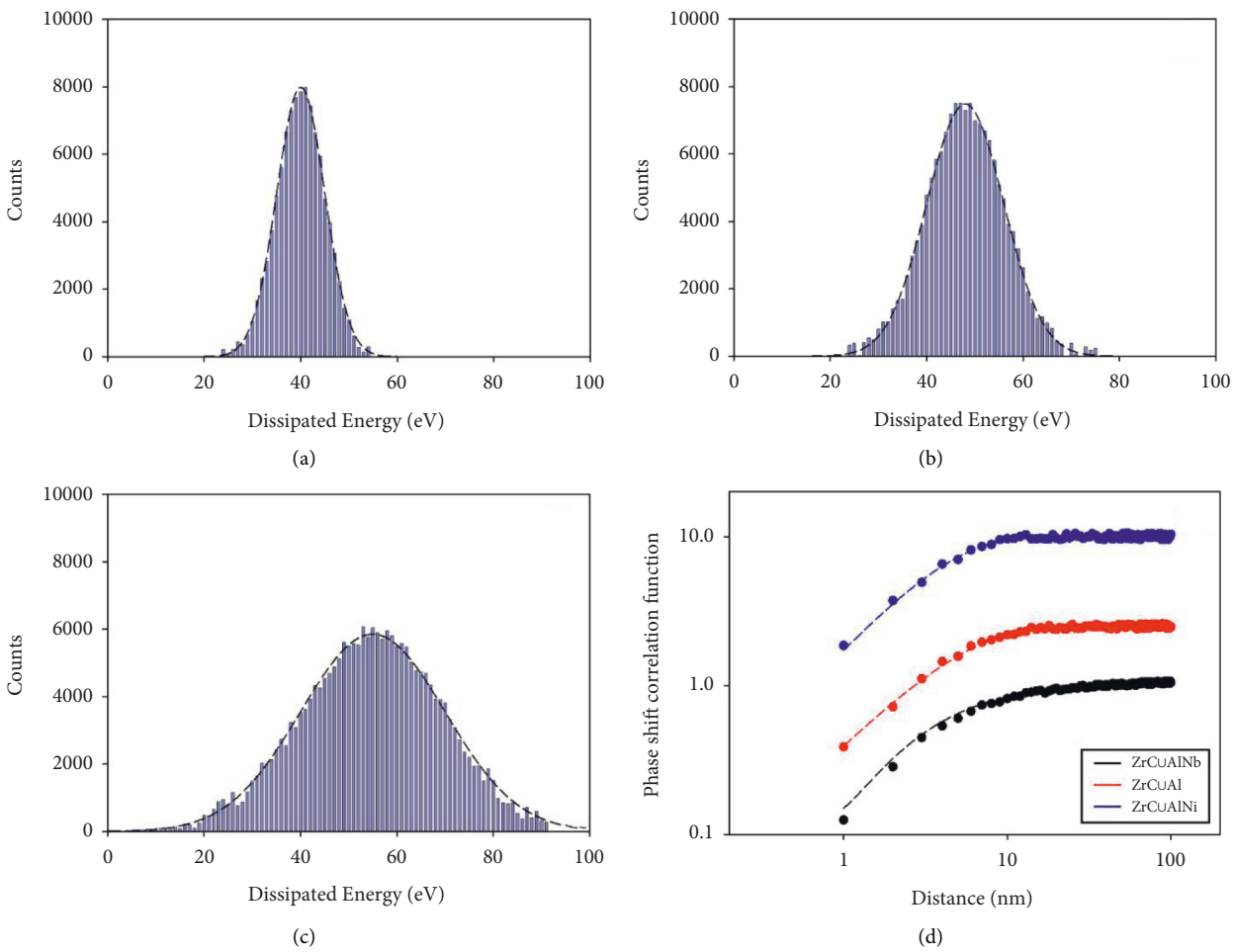

Figure 5: Gaussian energy distribution for (a) ZrCuAl, (b) ZrCuAlNb, (c) ZrCuAlNi, and (d) phase shift correlation function for all the samples.

suggests that the increase of structural heterogeneity is accompanied by the diversity of nanoscale regions with various local mechanical properties, leading to sporadic data distribution.

Figure 8 provides information regarding the correlation between the pop-in displacements and the load/magnitude of the derivative. The results indicate that the low magnitude of derivatives is associated with the small pop-in events. Moreover, it is found that Ni addition leads to shrinkage of data in the plots, meaning that the mechanism of plastic deformation in the Ni-added sample is consistent with the creation and propagation of multiple small shear events in

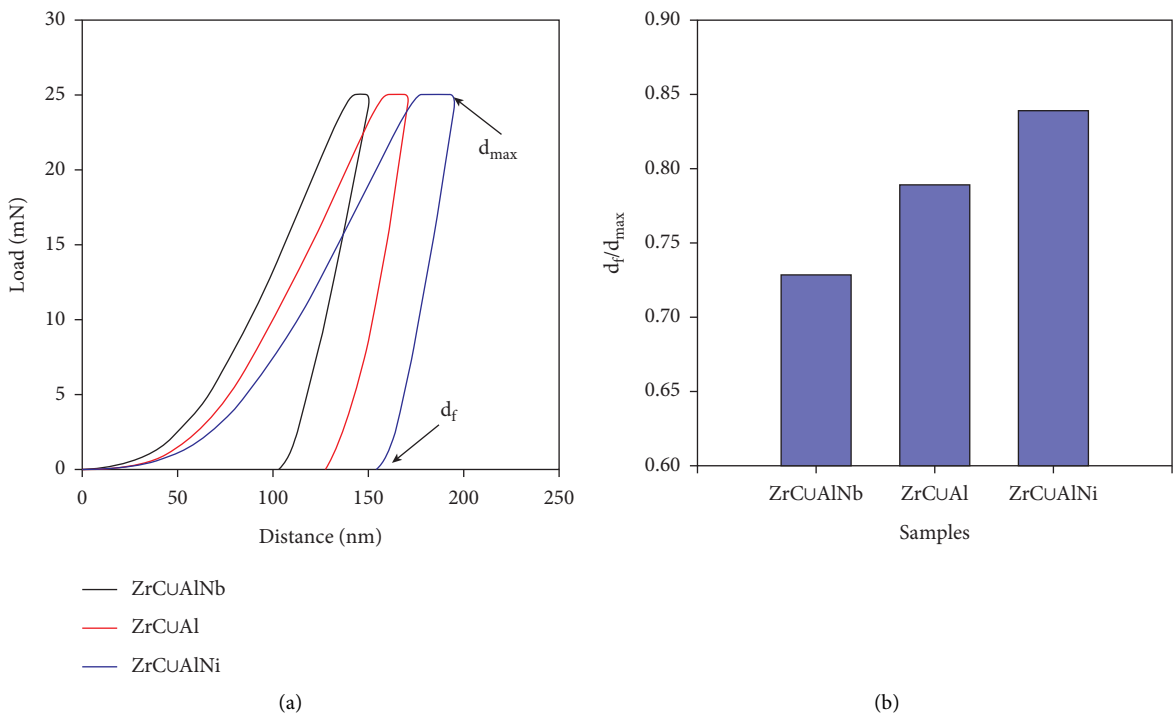

Figure 6: (a) Load-displacement curve and (b) d_f/d_{max} ratio for all the samples.

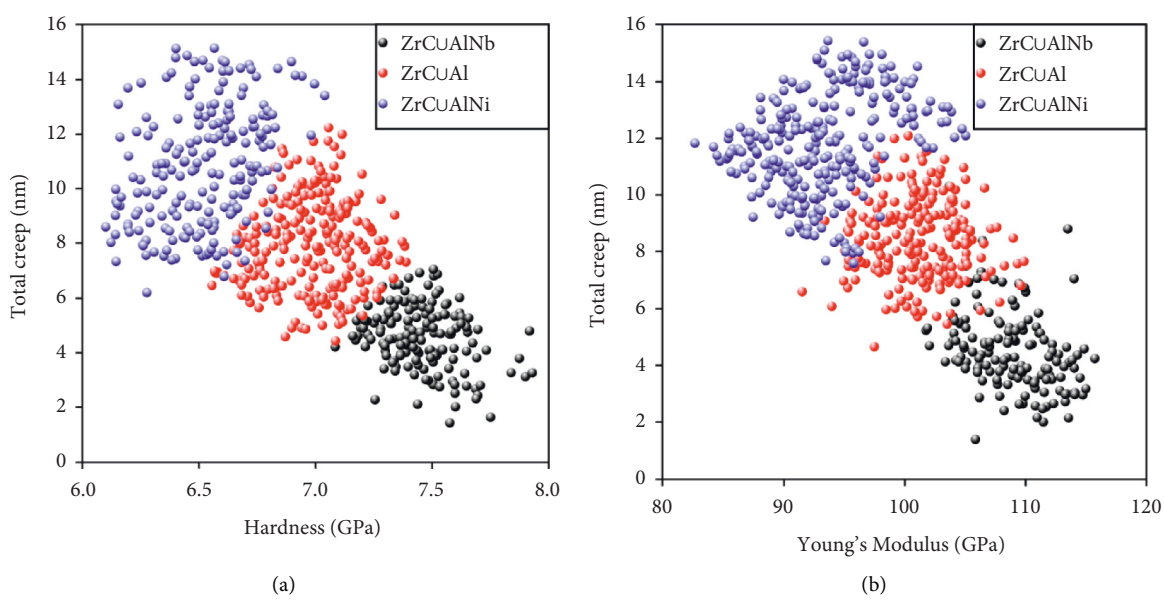

Figure 7: Total creep displacement as a function of (a) hardness and (b) Young's modulus.

the microstructure. On the other hand, the Nb-added sample exhibits the highest sporadic data in the plots, which implies the formation of main shear bands with highly localized strains. In other words, the Ni-added sample with the highest enthalpy of relaxation contains a huge amount of free volumes in its amorphous structure. In this state, the structural heterogeneity is more pronounced in the system, leading to the intensification of stress fields in the nanoscale regions. Hereupon, numerous shear events are formed and generated when an external loading is applied to the material. On the other hand, the high magnitude of the derivative in the Nb-added sample indicates that the shear bands can easily propagate through the sample without any interactions with other shear bands.

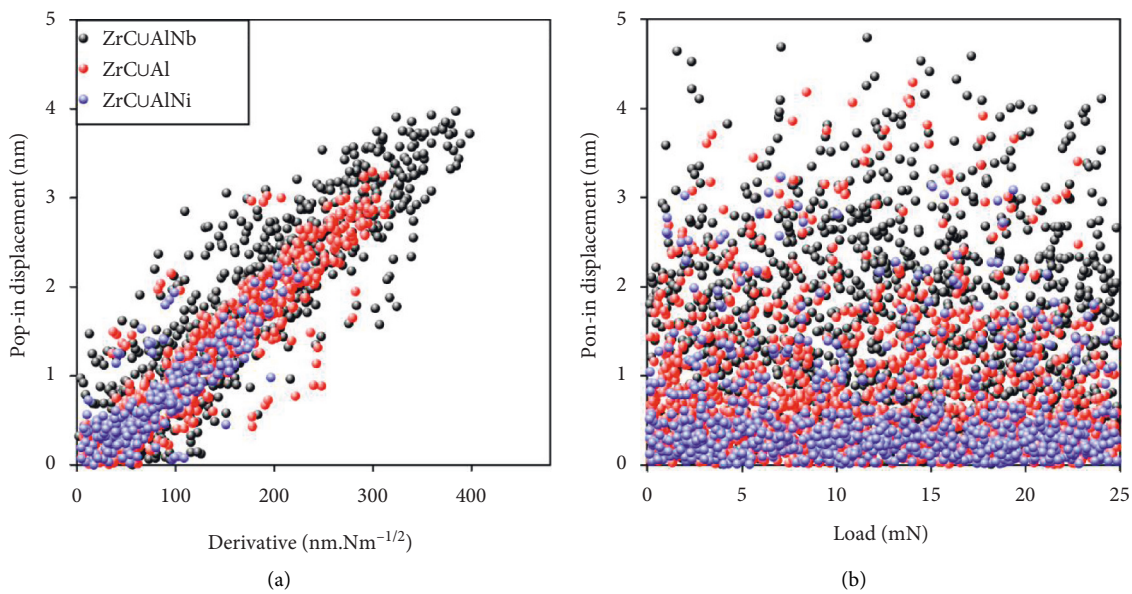

Figure 8: Pop-in displacement variations as a function of (a) load derivative and (b) load value.

4. Conclusions

The outcome of this work indicates how the minor addition of Ni and Nb elements can tune the structural features and nanomechanical properties of the ZrCuAl BMG. Based on the results, it is found that the Ni element is a promising constitute for increasing the total negative heat of mixing in the ZrCuAl system, leading to the improvement of relaxation enthalpy and structural heterogeneity. On the other hand, the Nb element shows a strong interaction with zirconium, which intensifies the SRO and MRO structures and reduces the fluctuations of structural variations in the amorphous alloy. The nanoindentation test also showed that the Nb-added sample has a lower displacement at the maximum load, which is a proper state for creep applications, whereas, the Ni-added sample exhibits a strong viscoelastic response, meaning that Ni addition is responsible for the creation and distribution of more loosely packed regions in the atomic structure.

Data Availability

The [DATA TYPE] data used to support the findings of this study are included within the article.

Conflicts of Interest

The authors declare that they have no conflicts of interest.

References

[1] X. S. Wei, J. L. Jin, Z. Z. Jiang, D. D. Liang, and J. Shen, "FeCrMoWCBY metallic glass with high corrosion resistance in molten lead–bismuth eutectic alloy," *Corrosion Science*, vol. 190, Article ID 109688, 2021.

[2] N. Sohrabi, J. Jhabvala, G. Kurtuldu et al., "Characterization, mechanical properties and dimensional accuracy of a Zr-based bulk metallic glass manufactured via laser powder-bed fusion," *Materials & Design*, vol. 199, Article ID 109400, 2021.

[3] N. Sohrabi, M. Hamidi-Nasab, B. Rouxel et al., "Fatigue performance of an additively manufactured Zr-based bulk metallic glass and the effect of post-processing," *Metals*, vol. 11, no. 7, p. 1064, 2021.

[4] P. Zhang, C. Zhang, and L. Liu, "Toughening 3D-printed Zr-based bulk metallic glass via synergistic defects engineering," *Materials Research Letters*, vol. 10, no. 6, pp. 377–384, 2022.

[5] S.-X. Liang, S. Salamon, S. Zerebecki et al., "A laser-based synthesis route for magnetic metallic glass nanoparticles," *Scripta Materialia*, vol. 203, Article ID 114094, 2021.

[6] W. Zhou, Y. Meng, F. Duan et al., "The effect of oxygen on phase formation in an industrial Zr based bulk metallic glass," *Intermetallics*, vol. 129, Article ID 107055, 2021.

[7] F. Xie, Q. Chen, and J. Gao, "Brittle-ductile transition in laser 3D printing of Fe-based bulk metallic glass composites," *Metals*, vol. 9, no. 1, p. 78, 2019.

[8] Y. J. Yang, B. Y. Cheng, J. W. Lv et al., "Effect of Ag substitution for Ti on glass-forming ability, thermal stability and mechanical properties of Zr-based bulk metallic glasses," *Materials Science and Engineering A*, vol. 746, pp. 229–238, 2019.

[9] Z. Long, P. Tao, G. Wang et al., "Effect of Nb and Ta addition on mechanical properties of Zr-based bulk metallic glasses and composites," *Journal of Alloys and Compounds*, vol. 912, Article ID 165071, 2022.

[10] T. Wang, Q. Hou, and L. Zhang, "Enhanced heterogeneity and plasticity in a Zr-Cu–Al bulk metallic glass with micro-addition of oxygen," *Materials Science and Engineering A*, vol. 831, Article ID 142222, 2022.

[11] H. B. Ke, J. F. Zeng, C. T. Liu, and Y. Yang, "Structure heterogeneity in metallic glass: modeling and experiment," *Journal of Materials Science & Technology*, vol. 30, no. 6, pp. 560–565, 2014.

[12] J. Zhu, W. Gao, S. Cheng et al., "Improving the glass forming ability and plasticity of ZrCuNiAlTi metallic glass by substituting Zr with Sc," *Journal of Alloys and Compounds*, vol. 909, Article ID 164679, 2022.

[13] D. D. Liang, X. S. Wei, C. T. Chang, J. W. Li, X. M. Wang, and J. Shen, "Effect of W addition on the glass forming ability and mechanical properties of Fe-based metallic glass," *Journal of Alloys and Compounds*, vol. 731, pp. 1146–1150, 2018.

[14] Y. Teng, Y. Song, S. J. Xie, and Z. D. Sha, "On the deformation and failure mechanisms of hydrogen alloyed metallic glasses," *Journal of Applied Physics*, vol. 131, no. 8, Article ID 085104, 2022.

[15] L. S. Luo, B. B. Wang, F. Y. Dong et al., "Structural origins for the generation of strength, ductility and toughness in bulk-metallic glasses using hydrogen microalloying," *Acta Materialia*, vol. 171, pp. 216–230, 2019.

[16] Z. S. Jin, Y. J. Yang, Z. P. Zhang et al., "Effect of Hf substitution Cu on glass-forming ability, mechanical properties and corrosion resistance of Ni-free Zr–Ti–Cu–Al bulk metallic glasses," *Journal of Alloys and Compounds*, vol. 806, pp. 668–675, 2019.

[17] D. Cao, Y. Wu, X. J. Liu, H. Wang, X. Z. Wang, and Z. P. Lu, "Enhancement of glass-forming ability and plasticity via alloying the elements having positive heat of mixing with Cu in Cu48Zr48Al4 bulk metallic glass," *Journal of Alloys and Compounds*, vol. 777, pp. 382–391, 2019.

[18] M. Gao and J. H. Perepezko, "Mapping the viscoelastic heterogeneity at the nanoscale in metallic glasses by static force spectroscopy," *Nano Letters*, vol. 20, no. 10, pp. 7558–7565, 2020.

[19] C. Ebner, B. Escher, C. Gammer, J. Eckert, S. Pauly, and C. Rentenberger, "Structural and mechanical characterization of heterogeneities in a CuZr-based bulk metallic glass processed by high pressure torsion," *Acta Materialia*, vol. 160, pp. 147–157, 2018.

[20] F. Zhu, S. Song, K. M. Reddy, A. Hirata, and M. Chen, "Spatial heterogeneity as the structure feature for structure–property relationship of metallic glasses," *Nature Communications*, vol. 9, pp. 3965–3967, 2018.

[21] Z. H. Mahmoud, H. Barazandeh, S. M. Mostafavi et al., "Identification of rejuvenation and relaxation regions in a Zr-based metallic glass induced by laser shock peening," *Journal of Materials Research and Technology*, vol. 11, pp. 2015–2020, 2021.

[22] N. Wang, J. Ding, P. Luo, Y. Liu, L. Li, and F. Yan, "Chemical variation induced nanoscale spatial heterogeneity in metallic glasses," *Materials Research Letters*, vol. 6, no. 12, pp. 655–661, 2018.

[23] M. Samavatian, R. Gholamipour, D. O. Bokov, W. Suksatan, V. Samavatian, and M. Mahmoodan, "Characterization of nanoscale structural heterogeneity in metallic glasses: a machine learning study," *Journal of Non-crystalline Solids*, vol. 578, Article ID 121344, 2022.

[24] D. P. Wang, J. C. Qiao, and C. T. Liu, "Relating structural heterogeneity to β relaxation processes in metallic glasses," *Materials Research Letters*, vol. 7, no. 8, pp. 305–311, 2019.

[25] M. Samavatian, R. Gholamipour, A. A. Amadeh, and V. Samavatian, "Inherent relation between atomic-level stresses and nanoscale heterogeneity in Zr-based bulk metallic glass under a rejuvenation process," *Physica B: Condensed Matter*, vol. 595, Article ID 412390, 2020.

[26] F. Zhu, H. K. Nguyen, S. X. Song et al., "Intrinsic correlation between β-relaxation and spatial heterogeneity in a metallic glass," *Nature Communications*, vol. 7, no. 1, p. 11516, 2016.

[27] Y. M. Lu, J. F. Zeng, S. Wang et al., "Structural signature of plasticity unveiled by nano-scale viscoelastic contact in a metallic glass," *Scientific Reports*, vol. 6, no. 1, Article ID 29357, 2016.

[28] S. Ouyang, L. J. Song, Y. H. Liu et al., "Correlation between the viscoelastic heterogeneity and the domain wall motion of Fe-based metallic glass," *Physical Review Materials*, vol. 2, no. 6, Article ID 063601, 2018.

[29] Z. Z. Yang, L. Zhu, L. X. Ye et al., "Nanoscale structural heterogeneity perspective on the improved magnetic properties during relaxation in a Fe-based metallic glass," *Journal of Non-crystalline Solids*, vol. 571, Article ID 121078, 2021.

[30] Q. H. Pham, S. Chupradit, G. Widjaja et al., "The effects of Ni or Nb additions on the relaxation behavior of Zr55Cu35Al10 metallic glass," *Materials Today Communications*, vol. 29, Article ID 102909, 2021.

[31] S. Y. Wu, S. H. Wei, G. Q. Guo, J. G. Wang, and L. Yang, "Structural mechanism of the enhanced glass-forming ability in multicomponent alloys with positive heat of mixing," *Scientific Reports*, vol. 6, no. 1, Article ID 38098, 2016.

Hindawi
Advances in Materials Science and Engineering
Volume 2022, Article ID 6111294, 8 pages
https://doi.org/10.1155/2022/6111294

Research Article

The Effects of Temperature and Impact Velocity on the Shock Wave Response of Pore-Embedded Metallic Glasses

Indrajit Patra,[1] **Ahmed M. Abdulhadi**,[2] **Fatima Safaa Fahim**,[3] **Bashar S. Bashar**,[4] **Taif Alawsi**,[5] **and Mohammad Salmani**[6]

[1]*Independent Researcher, Durgapur, West Bengal, India*
[2]*Civil Engineering Department, University of Warith Al-Anbiyaa, Karbala, Iraq*
[3]*Anesthesia Techniques Department, Al-Mustaqbal University College, Babylon, Iraq*
[4]*Al-Nisour University College, Baghdad, Iraq*
[5]*Scientific Research Center, Al-Ayen University, Thi-Qar, Iraq*
[6]*Department of Engineering, Payame Noor University, Tehran Branch, Tehran, Iran*

Correspondence should be addressed to Mohammad Salmani; salmanimohammad253@gmail.com

Received 7 May 2022; Revised 2 June 2022; Accepted 14 June 2022; Published 30 June 2022

Academic Editor: Majid Samavatian

Copyright © 2022 Indrajit Patra et al. This is an open access article distributed under the Creative Commons Attribution License, which permits unrestricted use, distribution, and reproduction in any medium, provided the original work is properly cited.

In this work, the shock wave response of a pore-embedded CuZr metallic glass (PEMG) under different impact velocities (0.5–1.5 km/s) and initial temperatures (300–600 K) was evaluated through the molecular dynamics (MD) simulation. The results indicated that the nucleation and growth of nanoscale shear events around the pore were the dominant mechanisms for plastic deformation under the shock wave. It was also found that the increase in the impact velocity led to the filling of pore, which was due to the structural softening and the local temperature increment in the vicinity of pore. Moreover, the spall event originated from the formation and coalescence of tension transformation zones, leading to the formation of nanovoids in the system. At higher velocities, the spallation was accompanied with the formation of more nanovoids with smaller sizes, inducing the brittle failure in the system. The MD outcomes also showed that the increase in initial temperature decreased the shock pressure and flow shear stress and led to the smoother spallation in the PEMG.

1. Introduction

Owing to the absence of long-range orders in their atomic structure, metallic glasses (MGs) exhibit fascinating mechanical properties such as high elastic limit, superior strength, and good self-sharpening [1–4]. Recently, MGs have been also identified as the promising materials for high-velocity impact applications, in which their shock responses grew in considerable importance [5–9]. For instance, Wen et al. [10] reported that the CuZr MGs demonstrates an overdriven plastic state rather than a single elastic shock wave with the piston velocity increasing. It was also found that the increase in Cu content led to the higher resistance to plastic deformation. Li et al. [11] evaluated the shock response of Zr-based MGs under the strain rate of $10^5\ s^{-1}$ and detected some nanocrystals in the impacted specimens. It was also revealed that the rise of impact pressure led to the change of failure mode from spallation to fragmentation accompanied with the combination of spalling cracks and longitudinal cracks. In another study, it was unveiled that the high initial temperature decreased the shear resistance of CuZr BMG under the high-rate loading [12]. Tan et al. [13] carried out the flyer-plate impact experiment and found that the induced stress decreased available free volume under planar impact loading. In this state, the decohesion strength was improved, due to the void coalescence under planar impact loading. Escobedo et al. [14] compared the shock response of two different Zr-based MGs and found that the ZrCuNiAl alloy experienced a higher Hugoniot elastic limit (HEL) and a smooth fracture surface morphology, while the ZrCuAgAl alloy exhibited a rougher fracture surface

with cup-cone features. Wang et al. [15] conducted plate-impact test and figured out that the rise of impact velocity improved the HEL and spall strength. Moreover, they claimed that the MG samples displayed a brittle behavior at macroscopic scale while their microscopic behavior was ductile. In another work, the Hugoniot-compression curve of ZrAlNiCu was measured and the results indicated that a kink was created on the curve at 14 GPa which was due to phase transition in the glassy structure [16].

The effect of embedded pores in the atomic configuration is also one of the main issues in the shock response of MGs. Due to the nanoscale size of pores, the molecular dynamics (MD) simulation has been an efficient method for evaluating the plastic deformation and mechanical properties of porous MGs [17–21]. Using MD simulation, Demaske et al. [22] showed that the mechanism of plastic deformation in the shocked MG is based on the nucleation and growth of shear transformation zones (STZs) around the pores, accompanied with the softening event at the vicinity of pores owing to a regional temperature increment. Song et al. [23] indicated that the void shapes considerably affected the level of atomic strain and fraction of atoms participating in the plastic deformation. They also found that there is no meaningful relation between the void collapse mode and void shape under the weak shocks. In this work, we tried to evaluate the effects of initial temperature and impact velocity on the shock wave response of a pore-embedded MG (PEMG). The results shed light on the design and fabrication of porous MGs for high-strain applications.

2. Computational Method

In general, a wide range of CuZr compositions has been constructed in the MD simulation [24]. In the Cu-rich MGs, the plastic deformation is based on the propagation of main shear bands, while the Zr-rich MGs exhibit a homogenous plasticity with an extensive strain led by the generation of multiple shear events in the structure [25]. Hence, we selected the $Cu_{60}Zr_{40}$ composition which shows a moderate plastic behavior in the CuZr system. In this study, the atomic-scale shock response of $Cu_{60}Zr_{40}$ was characterized through the large-scale atomic/molecular massively parallel simulator package [26]. Moreover, the interaction of Cu and Zr atoms in the structure was described by the embedded-atom method (EAM) potential [27]. At the first step, the $Cu_{60}Zr_{40}$ system with dimensions of $15 \times 15 \times 15\ nm^3$ was heated to 2200 K and kept for 1 ns to produce a homogenous melt. Afterward, the system was cooled to the room temperature (300 K) with cooling rate of 10^{11} K/s. The MG cell was then replicated to produce a large specimen with the dimensions of $30 \times 120 \times 120\ nm^3$. To ensure the removal of replicating effect, the large sample was again heated to 750 K, relaxed for 300 ps, and cooled back to 300 K. In the end, a spherical pore with a diameter of 20 nm was embedded in a lateral direction into the system (see Figure 1). Again, a similar relaxation treatment was conducted to eliminate the interface effects of embedded pore. It should be noted that the MD simulation was carried out under the three-dimensional periodic boundary conditions, the NPT ensemble, and time step of 2 fs [28, 29].

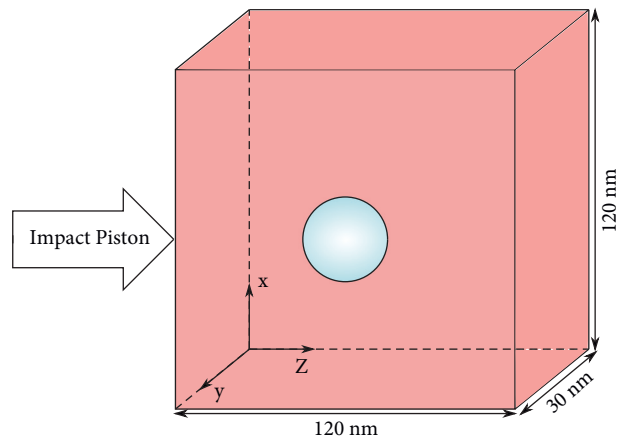

Figure 1: Schematic of PEMG for shock wave process.

After the sample preparation, the shock simulation was performed with the time step of 1 fs in the NVE ensemble under the free boundary conditions in the Z direction and periodic boundary conditions along the X and Y directions. For the shock simulation, an infinite-mass piston with a certain velocity (Up) moved to the MG sample along the Z direction, generating a sudden motion into the system. Consequently, one-dimensional strain with a planar shock wave mode upon a certain velocity (Us) is induced in the MG structure. The impact time was 40 ps and the Up level was set to 0.5–1.5 km/s. Moreover, the initial temperature was in the range of 300–600 K. In the end of impact loading, the piston atoms were unleashed, where the shock wave touched the opposite free surface. At this moment, a rarefaction wave was generated by removal of piston. The total time of shock loading simulation was 100 ps. It is worth mentioning that shock simulation was adopted by the momentum mirror technique [23]. Furthermore, to slice the CuZr MG along the Z direction, 1D binning analysis method was applied through the postprocessing software OVITO [30]. This technique facilitates the thermodynamic and kinetic evaluation of MG structure in each specific bin. To establish a meaningful comparison in the bins, it is also required to subtract the center-of-mass velocity for each bin [31]. The thermodynamic details of microstructure induced by the shock wave are given in [22, 32].

3. Results and Discussion

3.1. Role of Impact Velocity. Firstly, it is required to identify the pore effects on the thermodynamic behavior of PEMGs. Figure 2 represents the distribution of pressure (P_z), shear stress (τ), temperature, and density upon the impact velocity of 1 km/s and initial temperature of 300 K. The results indicated that the elastic wave precursor and the plastic wave front can be distinguished at 20 ps. It is suggested that the Hugoniot elastic limit defines the shock pressure at the point, where the elastic and plastic parts are separated (see

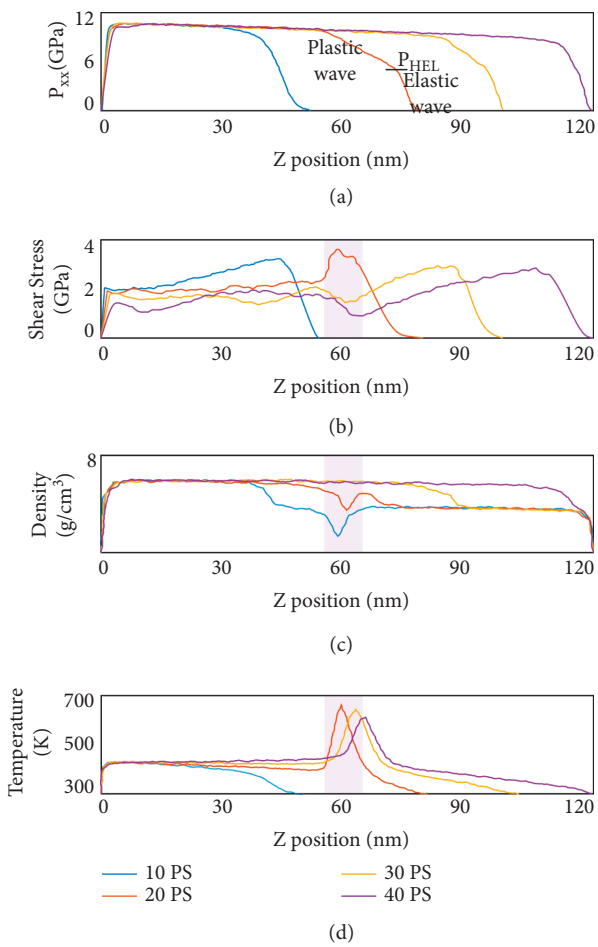

Figure 2: The trend of (a) pressure (P_z), (b) shear stress (τ), (c) density, and (d) temperature during the impact time upon the impact velocity of 1 km/s and initial temperature of 300 K.

Figure 2(a)). It should be noted that it is difficult to make a clear distinction between the elastic precursor and plastic front in the MGs [33]. This event becomes highlighted when the pore comes into play and interacts with the shock wave, leading to attenuation of plastic wave propagation in the atomic structure. As can be seen in Figure 2(b), the shear stress exhibited a significant increment in the pore area at 20 ps, which is consistent with the crossing of shock wave from the pore. This outcome means that the atoms are compressed in the pore site and densify this region, as also shown in Figure 2(c). At the time of 20 ps, the temperature of pore site significantly increases to 690 K, which can be due to the sharp movement of atoms at the pore surface (see Figure 2(d)). Previously, it was unveiled that the sharp rearrangement of atoms in the shear bands led to sudden increment of temperature [34]. It seems that the mechanism of temperature alteration in the shear bands is similar to the pore surfaces, where a sudden atomic rearrangement occurs in the system. Passing the time of 20 ps, a shear-stress relaxation occurs in the pore site, implying the intensification of local softening at the vicinity of pores. As also given in Figure 2(c), there is no difference between the density of pore site and its surrounding at 40 ps, demonstrating that the pore is getting filled under the evolution of shock wave through the MG.

The 2D atomic shear strain snapshots of PEMG under different impact velocities are presented in Figure 3. The results indicated that the atomic strain is negligible far from the pore, when the impact velocity is 0.5 km/s. However, some atomic motion in the plastic mode is detected at the vicinity of embedded pore under the evolution shock wave in the bulk of material. It should be noted that the plastic atomic motion mainly occurs perpendicular to the shock wave; however, the pore remains stable without losing its spherical geometry. Hence, it is totally concluded that the atomic response of PEMG can be mainly in an elastic mode at low velocities (0.5 km/s). With the increase of impact velocity to 1 km/s, the pore is nearly filled by the extreme rearrangement of surrounding atoms (40 ps). It is suggested that the filling of pore is accompanied with the generation of shear transformation zones (STZs) in the pore site [23], leading to stress relaxation in this region at 30–40 ps, as also shown in Figure 2(b). Moreover, the results showed that the pore is compressed in the x-axis so that the spherical shape changes to an ellipse configuration. This event proves that a large strain is introduced into the sample perpendicular to the generation of shock wave. At higher impact velocity (1.5 km/s), the glassy structure is exposed to a sharp void collapse owing to the strong shock pressure. In this state, the pore shrinks immediately and an interior jetting event is created along the pressure direction. The interior jetting event induces a hydrodynamic process, leading to sharp atomic compression along the shock direction and significant transfer of kinetic energy from the left side to the right side of the pore [22]. In crystalline materials, the collapse event under the shock wave is based on the dislocation emission from the free surface of pores [35], whereas the mechanism of plastic deformation in porous MGs originated from the formation of STZs around the pore and their generation into the empty space, as shown in Figure 3.

As indicated in Figure 2, the collapse event leads to temperature increment in the material. This primary result suggests that the porous structure may change the temperature behavior of MGs under the shock loading. Figure 4 illustrates the average peak temperature as a function of loading time in the regions with 5 nm thickness around the surface of the pore embedded in the glassy structure. Before the shock wave arrives at the pore site (see stage A in Figure 4), the impact loading itself increases the temperature in the MG structure. When the shock wave reaches the pore site (stage B), the plastic deformation begins in the system and the atoms fill the porous space, leading to significant temperature increment in the structure. At stage C, where the shock wave passes the pore site, the peak temperature declines, which may be due to the relaxation in the system. When the loading time reaches around 60–70 ps, a shoulder in the temperature profile is created (stage D). This shoulder resulted from the arrival of rarefaction waves to the pore site [22]. Finally, the spallation is completed in the system, leading to sharp temperature increment in the structure (stage E). One should note that the rise of impact velocity

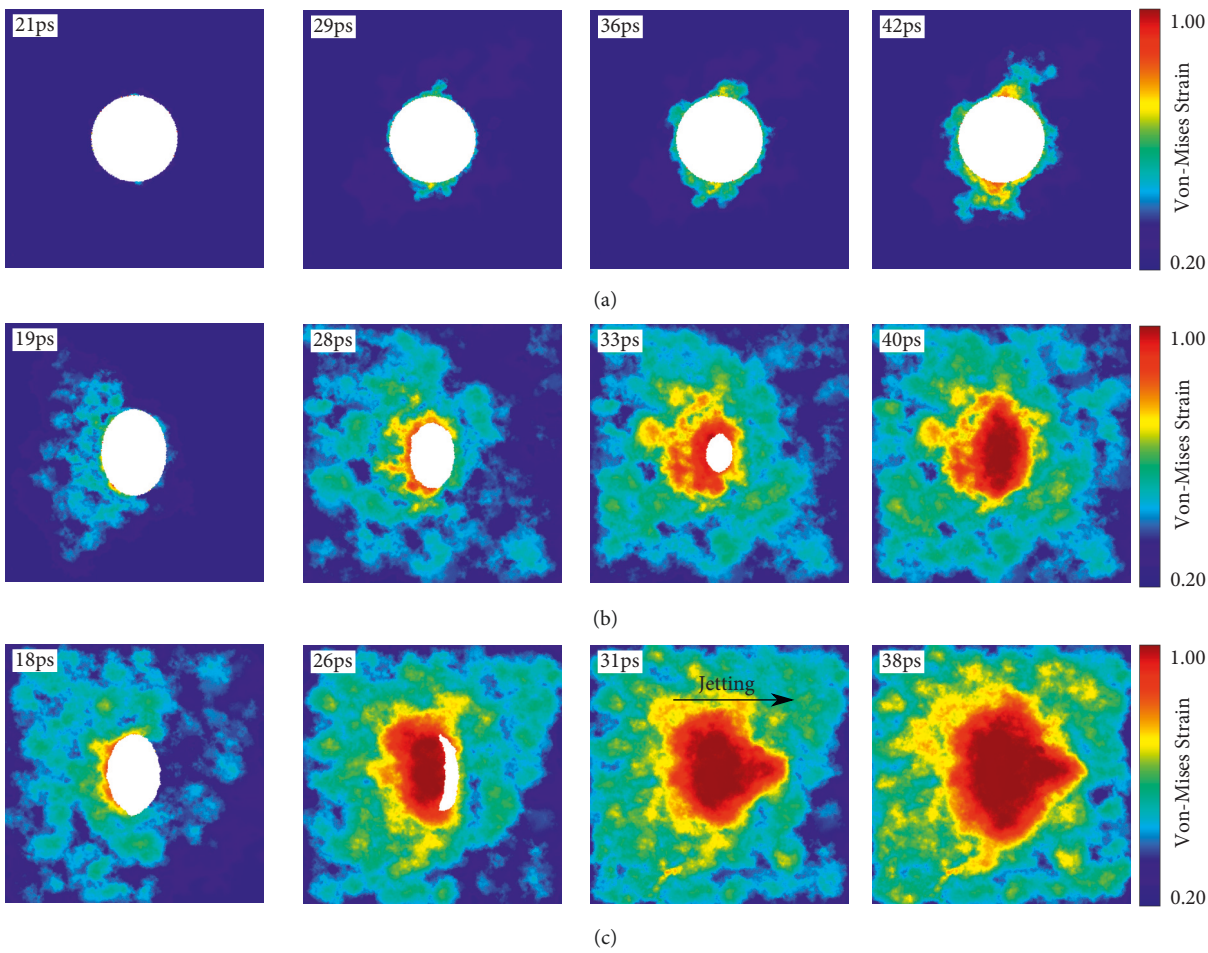

Figure 3: The 2D atomic shear strain snapshots of PEMG under impact velocity of (a) 0.5 km/s, (b) 1 km/s, and (c) 1.5 km/s.

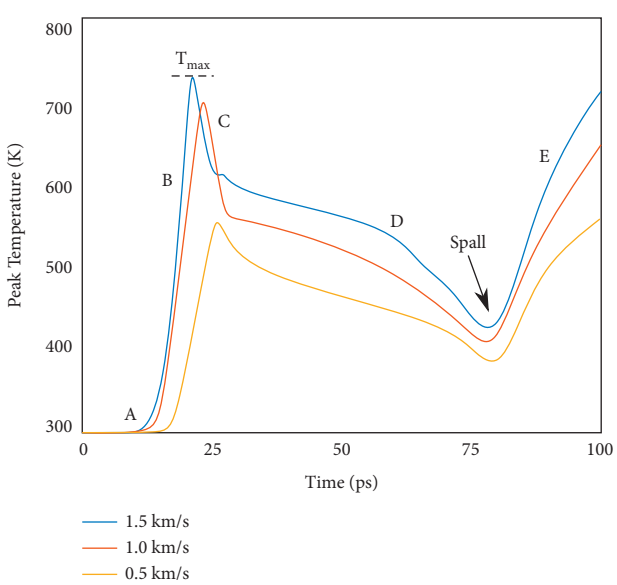

Figure 4: The temperature profile of PEMG under impact velocity of 0.5 km/s, 1 km/s, and 1.5 km/s.

from 1 km/s to 1.5 km/s speeds up the spallation in the system and leads to the intensification of temperature peaks in the pore vicinity. On the other hand, at low velocities (0.5 km/s), the temperature change is negligible, which may be due to the stability of pore geometry under the impact loading.

The plastic deformation of glassy structure under the spallation evolution was studied for the samples exposed to the impact velocities of 1 km/s and 1.5 km/s, in which the pores were filled under the shock wave evolution. Figure 5 indicates the atomic strain snapshots in a thick chunk of sample shocked by a velocity of 1 km/s. At the beginning of spall event, the tension transformation zones (TTZs) nucleate in the structure. It is suggested that the TTZs originated from the rearrangement and annihilation of atomic clusters exposed to the tensile stresses and subsequent sharp dilatation of shear transformation zones (STZs) [36, 37]. Other works also determined that the high-strain state in the shock loading prevents the plastic flow under the generation of STZs and subsequently it induces the fracture of MG through the evolution of TTZs [38]. The TTZs merge into each other and form voids in the system. Finally, the enlargement and coalescence of these voids lead to spall event in the material. Figure 6 illustrates the spallation in the MG structure under impact velocity of 1.5 km/s. As observed, with the increase in impact velocities ($U_p = 1.5$ km/s), the number of TTZs rises and consequently the void growth is restricted to the small sizes. The

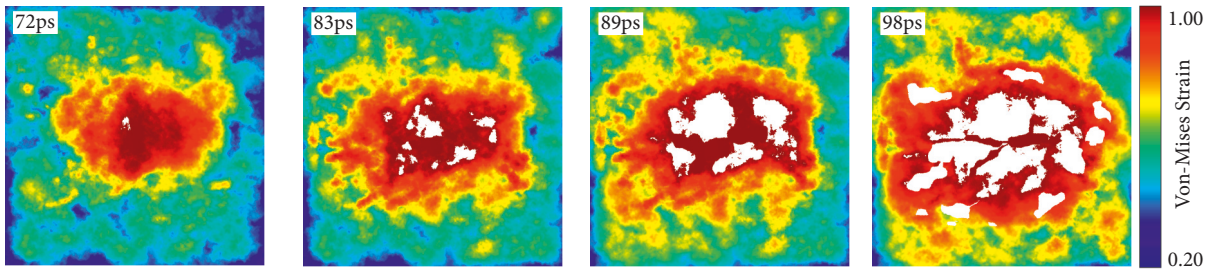

Figure 5: The spall evolution in the sample shocked by the impact velocity of 1 km/s and initial temperature of 300 K.

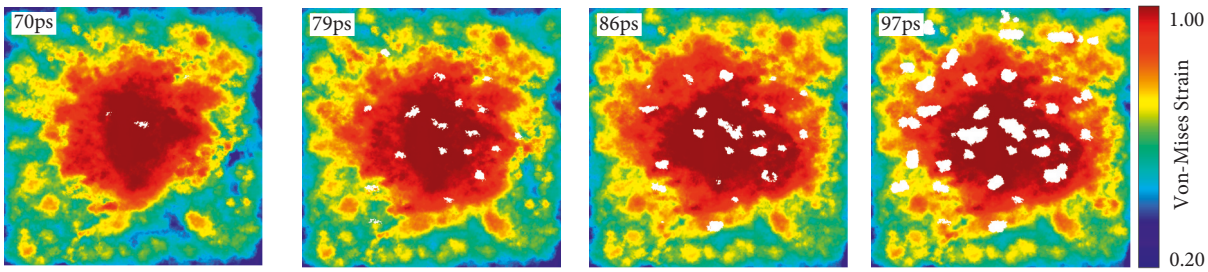

Figure 6: The spall evolution in the sample shocked by the impact velocity of 1.5 km/s and initial temperature of 300 K.

voids also become smaller and are uniformly distributed in the glassy structure at the impact velocity of 1.5 km/s. This outcome determines that there is competition between the void growth and TTZ nucleation with the increase of impact velocity. At lower U_p values, the temperature and strain rate of loading are relatively low, facilitating the stress relaxation and prohibiting the formation of TTZs in the system. On the other hand, the increase of U_p shortens the time of structural relaxation, leading to nucleation of multiple TTZs in the material. The experimental works indicated that creation of numerous small voids under the high impact velocity leads to smoothening of fractured surface in the MGs [39].

3.2. Role of Shock Temperature. Figure 7(a) represents the shear stress and P_z values as a function loading time for the sample shocked by the impact velocity of 1 km/s at room temperature (300 K). The results indicate that the shear stress shows a rapid peak at initial stage of loading and then it drops to a constant value, which is indicative of shear stress flow in the system. Moreover, the critical value of shear stress (τ_{HEL}) is the separator of elastic and plastic regimes under the shock loading. On the other hand, the P_z curve exhibits a two-step trend, in which the first step is associated to the elastic wave and the second step is correlated to the plastic deformation under the shock loading. In general, the pressure in the plastic deformation stage is identified as P_{shock} in the shock loading. Figure 7(b) shows τ_{flow} and P_{shock} as a function of initial temperature. It should be noted that τ_{flow} and P_{shock} values were obtained from the samples shocked through the impact velocities of 0.5–1.5 km/s. The results indicated that the increase in the initial temperature leads to the decline of τ_{flow} and P_{shock} values, meaning that the temperature alteration plays a significant role in the stress distribution. However, one can see that the rate of P_{shock} decrement is sharper than τ_{flow}. This outcome suggests that the shear stress is more dominant at higher temperatures, leading to nucleation and propagation of STZs in the structure, while the TTZ formation is restricted to a few number of sites. Hence, one can conclude that the higher initial temperature facilitates the STZ formation and plastic flow in the system, which causes a smooth spallation with a ductile failure. Figure 8 illustrates the trend of Cu-centered clusters in the samples exposed to the different initial temperatures under the impact velocity of 1 km/s. In general, the Cu-centered clusters are identified as the backbone structure of CuZr MGs and include main polyhedrons in the atomic system [40]. As observed in the figure, the increase in the initial temperature led to the sharp decrement of Cu-centered clusters in the MG structure. This means that higher temperature facilitates the plastic flow and generates the loosely packed regions, i.e., nanoscale free volumes, in the system. Hence, it is found that the plastic deformation is intensified at higher temperatures; however, it originated from the nucleation and propagation of STZ in the structure, as concluded from Figure 7.

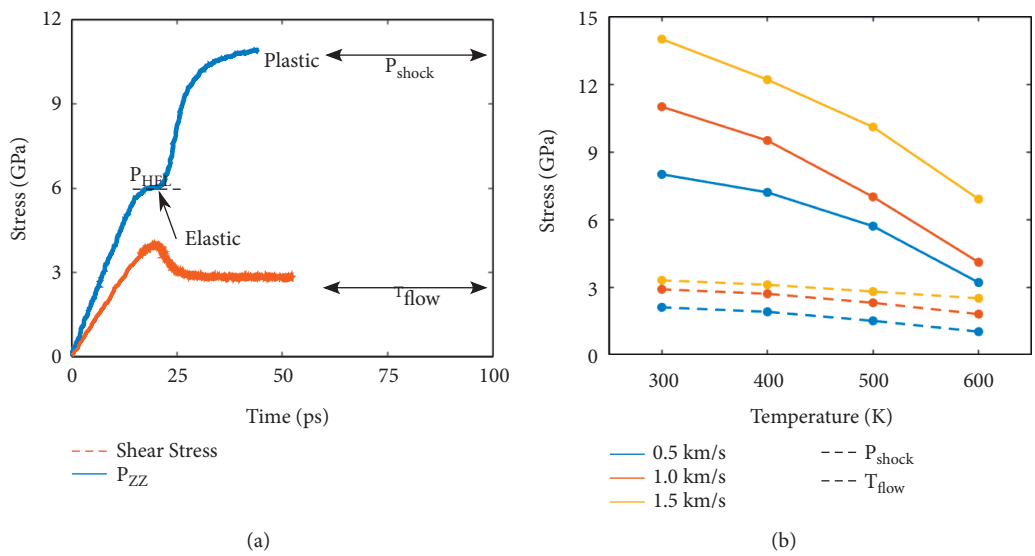

Figure 7: (a) Time dependence of P_z and shear stress τ for impact velocity of 1 km/s and initial temperature of 300 K. (b) Shock pressure and shear-stress flow as a function of initial temperature.

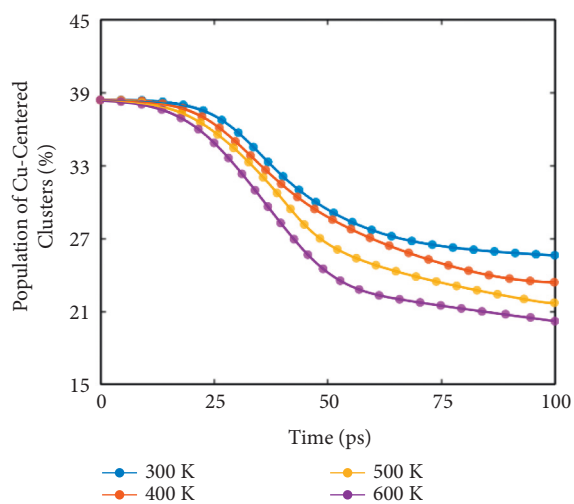

Figure 8: Population of Cu-centered clusters as a function of shock loading time under the impact velocity of 1 km/s and different initial temperatures.

4. Conclusions

In this paper, MD simulation was conducted to study the shock wave response of CuZr PEMG under different initial temperatures and impact velocities. Based on the MD results, the embedded pore was filled under the impact velocities of 1 and 1.5 km/s through the growth of shear events and local softening at the pore boundary. The results also demonstrated that the nucleation and coalescence of TTZs led to the formation of nanovoids under the spall event. The higher velocities induced smaller nanovoids with more population in the strained zones. The initial temperature also played a crucial role in the spall event so that the rise of temperature declined the induced pressure and shear stress in the system, which led to the restriction of TTZ formation and the smoother spallation.

Data Availability

The data used to support the findings of this study are included within the article.

Conflicts of Interest

The authors declare that they have no conflicts of interest.

References

[1] J.-c. Li, X.-w. Chen, and F.-l. Huang, "Ballistic performance of tungsten particle/metallic glass matrix composite long rod," *Defence Technology*, vol. 15, no. 2, pp. 132–145, 2019.

[2] K. Chen, M. Yuan, H. M. Zheng, and S. H. Chen, "On the determination and optimization of apparent "elastic limit" of kirigami metallic glasses," *Physica B: Condensed Matter*, vol. 609, Article ID 412901, 2021.

[3] M. Samavatian, R. Gholamipour, A. A. Amadeh, and S. Mirdamadi, "Correlation between plasticity and atomic structure evolution of a rejuvenated bulk metallic glass," *Metallurgical and Materials Transactions A*, vol. 50, no. 10, pp. 4743–4749, 2019.

[4] W. Bao, J. Chen, X. Yang, T. Xiang, Z. Cai, and G. Xie, "Improved strength and conductivity of metallic-glass-reinforced nanocrystalline CuCrZr alloy," *Materials & Design*, vol. 214, Article ID 110420, 2022.

[5] C. T. Wang, Y. He, C. Ji, Y. He, W. Han, and X. Pan, "Investigation on shock-induced reaction characteristics of a Zr-based metallic glass," *Intermetallics*, vol. 93, pp. 383–388, 2018.

[6] K. V. Reddy, C. Deng, and S. Pal, "Dynamic characterization of shock response in crystalline-metallic glass nanolaminates," *Acta Materialia*, vol. 164, pp. 347–361, 2019.

[7] S. Mishra, K. V. Reddy, and S. Pal, "Impact of crystalline-amorphous interface on shock response of metallic glass Al90Sm10/crystalline Al nanolaminates," *Applied Physics A*, vol. 127, no. 10, p. 774, 2021.

[8] X. C. Tang, C. Li, H. Y. Li et al., "Cup-cone structure in spallation of bulk metallic glasses," *Acta Materialia*, vol. 178, pp. 219–227, 2019.

[9] L. Lu, C. Li, W. H. Wang, M. H. Zhu, X. L. Gong, and S. N. Luo, "Ductile fracture of bulk metallic glass Zr 50 Cu 40 Al 10 under high strain-rate loading," *Materials Science and Engineering*, vol. 651, pp. 848–853, 2016.

[10] P. Wen, B. Demaske, D. E. Spearot, and S. R. Phillpot, "Shock compression of Cu x Zr100−x metallic glasses from molecular dynamics simulations," *Journal of Materials Science*, vol. 53, no. 8, pp. 5719–5732, 2018.

[11] Y. Li, X. Cheng, Z. Ma, X. Li, and M. Wang, "Dynamic response and damage evolution of Zr-based bulk metallic glass under shock loading," *Journal of Materials Science & Technology*, vol. 93, pp. 119–127, 2021.

[12] P. Wen, B. Demaske, D. E. Spearot, S. R. Phillpot, and G. Tao, "Effect of the initial temperature on the shock response of Cu50Zr50 bulk metallic glass by molecular dynamics simulation," *Journal of Applied Physics*, vol. 129, Article ID 165103, 2021.

[13] Y. Tan, Y. W. Wang, H. W. Cheng, and X. W. Cheng, "Dynamic fracture behavior of Zr63Cu12Ni12Al10Nb3 metallic glass under high strain-rate loading," *Journal of Alloys and Compounds*, vol. 853, Article ID 157110, 2021.

[14] J. P. Escobedo, D. J. Chapman, K. J. Laws et al., "Effects of chemical composition on the shock response of Zr-based metallic glasses," *AIP Conference Proceedings*, vol. 1793, Article ID 100032, 2017.

[15] B. P. Wang, L. Wang, S. Wang et al., "Mechanical response of Ti-based bulk metallic glass under plate-impact compression," *Intermetallics*, vol. 63, pp. 12–18, 2015.

[16] T. Mashimo, H. Togo, Y. Zhang et al., "Hugoniot-compression curve of Zr-based bulk metallic glass," *Applied Physics Letters*, vol. 89, no. 24, Article ID 241904, 2006.

[17] X. Q. Lu, L. Li, Y. H. Zhang et al., "Control of shear band formation in metallic glasses through introducing nanoscale pores," *Journal of Non-crystalline Solids*, vol. 569, Article ID 120994, 2021.

[18] N. V. Priezjev and M. A. Makeev, "Strain-induced deformation of the porous structure in binary glasses under tensile loading," *Computational Materials Science*, vol. 150, pp. 134–143, 2018.

[19] H. Liu, Z. Chen, J. Mo, M. Wang, Y. Zhang, and W. Yang, "Brittle-to-ductile transition in monatomic Tantalum nanoporous metallic glass," *Journal of Non-crystalline Solids*, vol. 506, pp. 6–13, 2019.

[20] Y. Luo, G. Yang, Y. Shao, and K. Yao, "The effect of void defects on the shear band nucleation of metallic glasses," *Intermetallics*, vol. 94, pp. 114–118, 2018.

[21] D.-Q. Doan, T.-H. Fang, T.-H. Chen, and T.-X. Bui, "Effects of void and inclusion sizes on mechanical response and failure mechanism of AlCrCuFeNi2 high-entropy alloy," *Engineering Fracture Mechanics*, vol. 252, Article ID 107848, 2021.

[22] B. Demaske, S. R. Phillpot, D. E. Spearot, and P. Wen, "Void collapse and subsequent spallation in Cu50Zr50 metallic glass under shock loading by molecular dynamics simulations," *Journal of Applied Physics*, vol. 125, no. 21, Article ID 215903, 2019.

[23] W. Song, Y. Yu, and Y. Guan, "Role of void shape on shock responses of nanoporous metallic glasses via molecular dynamics simulation," *International Journal of Mechanical Sciences*, vol. 218, Article ID 107076, 2022.

[24] M. Imran, F. Hussain, M. Rashid, Y. Cai, and S. A. Ahmad, "Mechanical behavior of Cu—Zr bulk metallic glasses (BMGs): a molecular dynamics approach," *Chinese Physics B*, vol. 22, Article ID 96101, 2013.

[25] X. X. Yue, C. T. Liu, S. Y. Pan, A. Inoue, P. K. Liaw, and C. Fan, "Effect of cooling rate on structures and mechanical behavior of Cu50Zr50 metallic glass: a molecular-dynamics study," *Physica B: Condensed Matter*, vol. 547, pp. 48–54, 2018.

[26] S. Plimpton, "Fast parallel algorithms for short-range molecular dynamics," *Journal of Computational Physics*, vol. 117, no. 1, pp. 1–19, 1995.

[27] M. I. Mendelev, D. J. Sordelet, and M. J. Kramer, "Using atomistic computer simulations to analyze x-ray diffraction data from metallic glasses," *Journal of Applied Physics*, vol. 102, Article ID 43501, 2007.

[28] P. Gupta, S. Pal, and N. Yedla, "Molecular dynamics based cohesive zone modeling of Al (metal)-Cu50Zr50 (metallic glass) interfacial mechanical behavior and investigation of dissipative mechanisms," *Materials & Design*, vol. 105, pp. 41–50, 2016.

[29] T. Bučko and F. Šimko, "On the structure of crystalline and molten cryolite: insights from the ab initio molecular dynamics in NpT ensemble," *The Journal of Chemical Physics*, vol. 144, Article ID 064502, 2016.

[30] A. Stukowski, "Visualization and analysis of atomistic simulation data with OVITO–the Open Visualization Tool," *Modelling and Simulation in Materials Science and Engineering*, vol. 18, Article ID 0, 2009.

[31] J.-L. Shao, C. Wang, P. Wang, A.-M. He, and F.-G. Zhang, "Atomistic simulations and modeling analysis on the spall damage in lead induced by decaying shock," *Mechanics of Materials*, vol. 131, pp. 78–83, 2019.

[32] F. Shimizu, S. Ogata, and J. Li, "Theory of shear banding in metallic glasses and molecular dynamics calculations," *Materials Transactions*, vol. 48, no. 11, pp. 2923–2927, 2007.

[33] B. J. Demaske, P. Wen, S. R. Phillpot, and D. E. Spearot, "Atomic-level deformation of Cu x Zr100-x metallic glasses under shock loading," *Journal of Applied Physics*, vol. 123, Article ID 215101, 2018.

[34] J. J. Lewandowski and A. L. Greer, "Temperature rise at shear bands in metallic glasses," *Nature Materials*, vol. 5, no. 1, pp. 15–18, 2006.

[35] L. P. Davila, P. Erhart, E. M. Bringa et al., "Atomistic modeling of shock-induced void collapse in copper," *Applied Physics Letters*, vol. 86, Article ID 161902, 2005.

[36] M. Q. Jiang, Z. Ling, J. X. Meng, and L. H. Dai, "Energy dissipation in fracture of bulk metallic glasses via inherent competition between local softening and quasi-cleavage," *Philosophical Magazine*, vol. 88, no. 3, pp. 407–426, 2008.

[37] C. Minnert, M. Kuhnt, S. Bruns et al., "Study on the embrittlement of flash annealed Fe85.2B9.5P4Cu0.8Si0.5 metallic glass ribbons," *Materials & Design*, vol. 156, pp. 252–261, 2018.

[38] X. Zhang, W. Li, Y. Deng, J. Shao, X. Zhang, and L. Chen, "Strength criterion and temperature dependent strength model of metallic glasses," *International Journal of Solids and Structures*, vol. 163, pp. 242–251, 2019.

[39] H. Jia, G. Wang, S. Chen, Y. Gao, W. Li, and P. K. Liaw, "Fatigue and fracture behavior of bulk metallic glasses and their composites," *Progress in Materials Science*, vol. 98, pp. 168–248, 2018.

[40] Y.-L. Guan, L.-S. Dai, J.-L. Shao, and W.-D. Song, "Molecular dynamics study on the nanovoid collapse and local deformation in shocked Cu50Zr50 metallic glasses," *Journal of Non-Crystalline Solids*, vol. 559, Article ID 120703, 2021.